UCGE Reports
Number 20180

Department of Geomatics Engineering

Investigations into the Estimation of Tropospheric Delay and Wet Refractivity Using GPS Measurements
(URL: http://www.geomatics.ucalgary.ca/links/GradTheses.html)

by

Sudhir Man Shrestha

July 2003

UNIVERSITY OF CALGARY

Calgary, Alberta, Canada

UNIVERSITY OF CALGARY

Investigations into the Estimation of Tropospheric Delay

And

Wet Refractivity Using GPS Measurements

by

Sudhir Man Shrestha

A THESIS

SUBMITTED TO THE FACULTY OF GRADUATE STUDIES

IN PARTIAL FULFILMENT OF THE REQUIREMENTS FOR THE

DEGREE OF MASTER OF SCIENCE

DEPARTMENT OF GEOMATICS ENGINEERING

CALGARY, ALBERTA

JULY, 2003

ABSTRACT

The principal error source in the GPS technology is a delay experienced by the GPS signal in propagating through the electrically neutral atmosphere, usually referred to as a tropospheric delay. This delay is normally calculated in the zenith direction, and is referred to as a zenith tropospheric delay. The delay consists of a zenith hydrostatic delay, which can be modeled accurately using surface barometric measurements, and a zenith wet delay, which cannot be modeled from surface barometric measurements and depends on atmospheric water vapor. In this research presented here, the approach for the production of zenith wet delays from GPS observations is demonstrated. Slant wet delays are recovered for each epoch to all satellites in view assuming that the atmosphere is inhomogeneous. The RMS errors in slant wet delay recovery are found to be about 2-3 cm, through validation of wet delays estimates compared with water vapor radiometer (WVR) "truth" data. Experiments are conducted to determine the optimal processing parameters for estimation of tropospheric delay parameters such as elevation cutoff angle, batch processing interval, and baseline length.

Observations of the slant wet delay can be used to model the vertical and horizontal structure of water vapor over a local area. These techniques are based on a tomographic approach using the slant wet delays as input observables, where a 4-D model of the wet refractivity may be derived. Extensive simulations are performed for various vertical resolutions, elevation cutoff angles, and reference station vertical geometries to determine the sensitivity and accuracy of the tomographic solution for a given network. The tomographic technique is tested with real GPS data from the Southern California Integrated GPS Network (SCIGN) to define the wet refractivity in a local network. Results indicate that slant wet delays may be derived from the estimated wet refractivity fields with accuracies of 2-3 cm.

ACKNOWLEDGEMENTS

TABLE OF CONTENTS

LIST OF TABLES

LIST OF FIGURES

LIST OF SYMBOLS

$L_1(t)$	modulated L1 signal
$L_2(t)$	modulated L2 signal
A_1	amplitude of L1
A_2	amplitude of L2
$P(t)$	P code
$N(t)$	navigation messages (ephemerides)
$\cos(f_1 t)$	unmodulated L1 or L2 signal
$\cos(f_2 t)$	unmodulated L2 signal
$C/A(t)$	C/A code
p	measured pseudorange
ρ	geometric range
$d\rho$	orbital error
r^s	position vector of a satellite
R_r	position verctor of a receiver
dt	satellite clock error
dT	receiver clock error
d_{ion}	ionospheric delay
d_{trop}	tropospheric delay
ε_ρ	receiver code noise and multipath
Φ	observed integrated carrier phase range
N	integer ambiguity (cycles)
λ	wavelength
ε_Φ	receiver carrier phase noise and multipath
$\dot{\Phi}$	measured Doppler
$\dot{\rho}$	geometric range rate
$\dot{d\rho}$	orbital error drift
$\dot{dt}$	satellite clock error drift
$\dot{dT}$	receiver clock error drift
$\dot{d}_{ion}$	ionospheric delay drift

$\dot{d}_{trop}$	tropospheric delay drift
$\dot{\varepsilon}_\Phi$	noise drift
af_0	zero order coefficient
af_1	first order coefficient
af_2	second order coefficient
t	time of measurement
t_{oc}	time of ephemeris
d_{rel}	relativity correction
t_{gd}	group delay
f	frequency of the signal
e	electron charge
ε_0	mass of an electron
υ	electron-neutral collision frequency
f_H	electron gyro frequency
Δt	ionospheric time delay
f	frequency of the signal
c	speed of light
N_e	ionospheric electron density
E	electron charge
$\Delta\phi$	phase shift
ε_P	measurement noise
σ^2	noise variance
Φ_D	phase of direct signal
β	attenuation due to multipath
Θ	phase shift due to multipath
P_d	partial pressure due to dry gases
K_i	refractivity constants,
e	partial pressure of water vapor,
T	absolute temperature.
$m_h(\varepsilon)$	hydrostatic mapping function,
$m_w(\varepsilon)$	wet mapping function
P_s	surface pressure
g_s	surface gravity at the station
r_s	mean geocentric radius of the station

LIST OF ABBREVIATIONS

GPS	Global Positioning System
C/A	Coarse acquisition
IGS	International GPS Service
NGS	National Geodetic Survey
WVR	Water vapor radiometer
MET3A	Meteorological package 3A
RMS	Root mean square
SCIGN	Southern California Integrated GPS Network

CHAPTER ONE

INTRODUCTION

1.1 BACKGROUND

The NAVSTAR GPS (NAVigation Satelllite Timing And Ranging Global Positioning System) is an all-weather, space-based navigation system developed by the U.S. Department of Defense to determine ones position, velocity, and time accurately in a common reference system on the Earth. The present constellation consists of nominally 24 satellites and provides global coverage with four to eight satellites simultaneously observed above $15°$ elevation.

When radio signals propagate through the atmosphere, they are delayed due to the different refractivity indices of the each layer of the atmosphere. The atmosphere has a significant effect on the propagation of a GPS signal. The signal travels through the ionosphere, which is a region of charged particles with a large number of free electrons. The delay caused by the ionosphere is dispersive in nature, meaning that the delay is dependent upon the frequency of the signal. Because GPS broadcasts on two separate frequencies, the error can be eliminated by taking advantage of combinations of the two separate frequency signals. Unlike the ionosphere, the delay caused by the neutral atmosphere is non-dispersive, or completely independent of the signal frequency (for GPS frequencies). The neutral atmosphere consists of the troposphere, tropopause, stratosphere, and part of the mesosphere. The delays caused by the neutral atmosphere in the radio signal propagation are mostly due to the troposphere. However, tropospheric delays can be detected or eliminated with accurate knowledge of the position of the GPS antenna and GPS satellite if the GPS applications require it. The tropospheric delay is measured in distance, and a typical zenith tropospheric delay would be 2.50 m, meaning that the troposphere causes a

GPS range observation to have an apparent additional 2.50 m distance between the ground-based receiver and a satellite at zenith.

The delay caused by the troposphere can be separated into two main components: the hydrostatic delay and the wet delay (Saastamoinen, 1972). The hydrostatic delay is caused by the dry part of gases in the atmosphere, while the wet delay is caused solely by highly varying water vapor in the atmosphere. The hydrostatic delay makes up approximately 90% of the total tropospheric delay. The hydrostatic delay is entirely dependent on the atmospheric weather characteristics found in the troposphere. The hydrostatic delay in the zenith direction is typically about 2.30 m (Businger et al., 1996; Dodson et al., 1996). The hydrostatic delay has a smooth, slowly time-varying characteristic due to its dependence on the variation of surface pressure; it can be modeled and range corrections applied for more accurate positioning results using measurements of surface temperature and pressure. However, the wet delay is dependent on water vapor pressure and is a few centimeters or less in arid regions and as large as 35 centimeters in humid regions. The wet delay parameter is highly variable with space and time, and cannot be modeled precisely with surface measurements (Bevis et al., 1992). By measuring the total delay, and calculating the hydrostatic delay from theoretical models using surface measurements, the remaining wet delay signal, caused by water vapor in the atmosphere, may be recovered.

The tropospheric delays are not measured directly to all satellites in view. Instead, there are several mapping functions that take zenith signal delays and map them to all individual GPS satellites in view at a given site. The Lanyi (1984), Herring (1992), Ifadis (1986), and Neill (1996) models are examples of mapping functions that can be used for high-precision positioning applications. The individual satellite-receiver line-of-sight signal delays are termed as slant delays.

The study of atmospheric water vapor is important for two reasons. Firstly, short-term weather forecasting is affected by the content of water vapor in the atmosphere. Water vapor is highly variable both in time and space and sudden changes in water vapor in the

atmosphere can result in changes in the local weather. Water vapor is fundamental to the transfer of energy in the atmosphere (Rocken et. al, 1997). This transfer of energy often results in thunderstorms or even more violent atmospheric phenomena. Secondly, long-term climate changes are reflected in water vapor content. Water vapor is a greenhouse gas, which traps emitted long wave radiation from the Earth's surface. Scientists may be able todirectly measure and model the spatio-temporal manifestations of climate change, such as changes to processes of atmospheric water vapor content.

Measurements of water vapor may be expressed in terms of the precipitable water vapor (PWV). Currently, water vapor is very poorly measured in real-time using conventional instruments and techniques. Radiosondes and water vapor radiometers are used to measure water vapor in the atmosphere directly, but they have severe limitations, such as high cost and poor spatial coverage. Better predictions of weather can be obtained by measuring water vapor accurately both in time and space using GPS. The use of GPS to measure water vapor in the atmosphere for the application of weather predictions and study of climate change is currently referred to as GPS meteorology.

The zenith tropospheric delays and azimuthal gradients can be estimated using GPS if positions of the satellites and the ground-based antenna are known. The zenith wet delays are extracted from the total zenith tropospheric delays by subtracting the zenith hydrostatic delays modeled precisely using surface meteorological measurements. Zenith wet delays are then mapped from vertical to slant by adding the azimuthal gradient contributions and using a theoretical mapping function for respective station-satellite pairs. The satellite-receiver slant wet delays may further be expressed as the product of the path length and the refractivity, integrated along the appropriate satellite-receiver line-of-sight. Tomographic techniques may then be successfully applied to obtain 4-D profiles of the tropospheric wet refractivity in a local dense network of GPS receivers (Flores et al., 2000b). Slant wet delays are the basic observables in the tomographic processing. By dividing the lower atmosphere into vertical layers up to a height of 8 km, and expressing the slant wet delays as discrete summations of wet refractivity multiplied by path length, the wet refractivity in

each layer may be estimated in successive time windows by discrete inversion methods (Skone and Shrestha, 2003). Knowledge of the 4-D wet refractivity fields for a given network allows estimation of water vapor content at any time and any location in the network area.

1.2 OBJECTIVES

There are two objectives in this thesis. The first objective is to validate techniques for producing the slant wet delays from GPS observations. The troposphere range delay is a limiting error source for GPS technology. As stated previously, this propagation delay is generally split into hydrostatic and wet delay components, and is estimated in the zenith direction above a station. In this thesis, the total tropospheric delays and the azimuthal gradients are derived above a given GPS site using the Bernese software version 4.2, which employs a carrier phase-based double difference approach. The hydrostatic delays are due to the dry gases in the troposphere and the non-dipole component of water vapor refractivity, and can be modeled accurately using surface measurements. By subtracting this contribution from the total zenith tropospheric delays, the wet delays are isolated and recovered. The zenith wet delays are then mapped into slant wet delay observations using a theoretical mapping function. The production of these slant wet delays is validated by comparisons with observations of integrated water vapor from an extensive set of water vapor radiometer (WVR) "truth" data.

The second objective is to define a tomographic model using slant wet delays from a regional GPS network. Tropospheric tomography is a promising technique for the determination of the spatio-temporal structure of the atmosphere and defines spatio-temporal representations of the wet refractivity field in the lower troposphere. Wet refractivity as a result of tropospheric tomography can be used for the estimation of water vapor in the atmosphere. Two sets of analyses are conducted for the tomographic approach.

Simulations are first conducted to determine optimal processing parameters and limitations in the tomographic model. Results are then derived using real GPS observations for a regional GPS network in Southern California.

Two data sets are used to realize these objectives. The validation of slant delays is done using GPS and WVR data collected on the roof of the Engineering building at the University of Calgary. A second set of data was available for six GPS stations in the Southern California Integrated GPS Network (SCIGN). This GPS network data is used to first produce slant wet delay observations, and these observations are then used to derive wet refractivity profiles using the tomographic approach. Validation of the tomographic approach is conducted using observations from the SCIGN network for a period of 12 days.

1.3 OUTLINE

Chapter 2 provides background material related to the GPS. GPS observables are described and different errors affecting GPS observations are discussed. These include orbital errors, multipath errors, receiver noise, and satellite clock errors. Errors due to atmospheric effects, the ionospheric and tropospheric range delays, are introduced.

Chapter 3 presents the physics of the troposphere, with a focus on the structure of the troposphere, and the refractivity of the lower layer of the atmosphere. The tropospheric path delay is defined mathematically for the GPS signals. Tropospherics models are described, in addition to different mapping functions, which are used to model the elevation dependence of the propagation delay.

Chapter 4 gives the general introduction of two data sets used in this thesis to validate slant wet delays. It includes a description of instruments used for collecting data on the roof of the Engineering Building at the University of Calgary. Principles of the water vapor radiometer (WVR) operation are given in this chapter. The algorithms employed in Bernese

software version 4.2 (Hugentobler et al., 2001) to define total tropospheric delay are discussed. The approach used to compute slant wet delays of GPS signals is also provided. Validation of slant wet delays from GPS measurements is presented.

Chapter 5 describes the tropospheric tomography approach and introduces the formulation of the tomographic model. Simulations of the tomographic approach are presented using various processing parameters for a regional GPS network. This simulation is based on MatLab routines from the GPSoft suite of programs. Finally, the tomography algorithm is tested using a data set from a regional network of GPS sites in the Southern California Integrated GPS Network (SCIGN).

Chapter 6 gives the conclusions and recommendations.

CHAPTER TWO

GPS OBSERVABLES AND ERRORS

2.1 THE GLOBAL POSITIONING SYSTEM (GPS)

Throughout time, people have been developing a variety of ways to figure out their position on the Earth and to navigate from one place to another. Early mariners relied on the use of angular measurements of the natural stars to define the position on the Earth. In the 1920s, the radionavigation technique was introduced to allow the navigators to locate the direction of shore-based transmitters. These techniques included radio beacons, very high frequency omnidirectional radios (VORS), long-range radio navigation (LORAN), and OMEGA. In the 1960s, the development of artificial satellites promised the possibility of use of precise, line-of-sight radionavigation signals to define the position on the Earth. Satellites were used to define the two-dimensional position in a U.S. navy system called Transit.

In 1973, the U.S. Department of Defense decided to develop and deploy the NAVSTAR GPS (NAVigation Satellite Timing And Ranging Global Positioning System). The Global Positioning System is a 24-satellite constellation in orbit around the Earth with ground–based monitoring stations. GPS navigation and position determination is based on measuring the distance from the user to known locations of the GPS satellites as they orbit. It is possible to determine three coordinates of user's positions (latitude, longitude, and altitude) as well as GPS receiver clock time offset using range measurements to four satellites. According to Wooden (1985),

" The Navstar Global Positioning System (GPS) is an all-weather, space-based navigation system under development by the U.S. Department of Defense to satisfy the requirements

for the military forces to accurately determine their positions, velocity and time in a common reference system, anywhere on or near the Earth on a continuous basis."

Originally, GPS was developed to meet military requirements; it was quickly adopted by the civilian world with some restrictions. The civilian usage of GPS has enormously increased and has included more applications with the elimination of SA (Selective Availability) on May 2, 2000.

2.1.1 The Space Segment

The present GPS constellation consists of 24 satellites in six orbital planes in almost circular orbits with an altitude of about 20,200 km above the surface of the Earth, with orbital periods of approximately 11 hours 58 minutes. The orbital planes are inclined 55° with respect to the equator. This constellation provides global coverage with four to eight satellites simultaneously observed above 15° elevation. The orbital configuration is illustrated in Figure 2.1
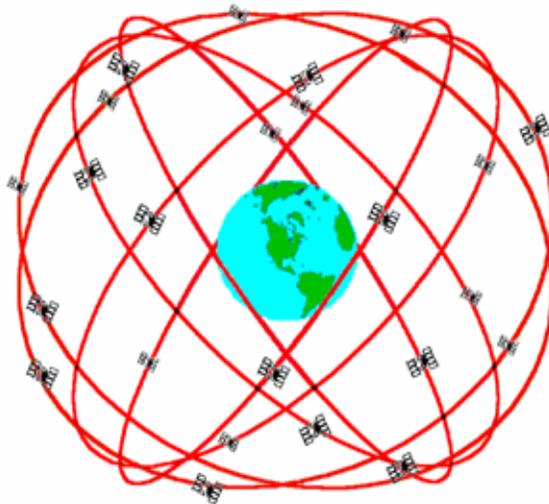
Figure 2.1 GPS orbital configuration.

The GPS satellites provide a platform for radio transmitters, computers, and various equipment used for positioning, timing, RF transmission and for a series of other military projects. The satellites are equipped with solar panels for power supply, reaction wheels for attitude control, and a propulsion system for orbit adjustments. Each satellite has highly accurate timing standards derived from rubidium and cesium clocks. The electronic equipment of the satellites allows the user to measure a pseudorange to the satellite, and each satellite to broadcast a message, which allows the user to recognize the satellite and to determine its position in space for arbitrary epochs. Each satellite transmits on two modulated signals. The detail signal structure is described in Section 2.1.4.

2.1.2 The Control Segment

The Operational Control System (OCS) consists of a master control station, monitor stations, and ground control stations. The master control station is located at Schriever Air Force Base in Colorado Springs. The master control station collects the tracking data from five monitor stations and calculates the satellite orbit and clock parameters. These results are then passed to one of the three ground stations for eventual upload to the satellites. The five monitor stations are equipped with precise cesium time standards and receivers that continuously measure range data to determine the broadcast ephemerides as well as model the satellite clocks. The ground stations mainly consist of ground antennas that receive the satellite ephemerides and clock information and upload them to each GPS satellite.

The control segment is also responsible for establishing GPS Time, which is defined as the number of seconds elapsed from Saturday midnight of the present week (cf. Kaplan, 1996). GPS time is realized by an atomic time scale, which is related to UTC (Universal Time Coordinated). GPS time is synchronized with UTC at the microsecond level, within an integer number of seconds. GPS satellites transmit clock corrections, which model the deviation of the clocks with respect to GPS time. The deviation is less than 1 ms and corrections are accurate to within a few nanoseconds (Lachapelle, 2001).

2.1.3 The User Segment

During early days of development of GPS, it was planned to incorporate GPS receivers into every major defense system. The receivers are used in land, sea and airborne vehicles to coordinate the military activities. However, GPS would not be a perfect military system since it is prone to jamming and relies on line-of-sight visibility from an antenna to a satellite.

The primary focus in the early years of GPS developers was on navigation for civilian use, but the surveying community quickly adopted the system for high-accuracy positioning. The use of GPS in the civilian community is expanding rapidly due to the decrease in receiver costs. The user segment consists of receiver technologies for computing local position/navigation solutions, in addition to the receiver clock offset. The GPS satellite positions are computed in the Earth-centred Earth-fixed WGS-84 reference system, such that a user's position is referenced to the WGS-84 ellipsoid.

2.1.4 The Satellite Signal

The GPS signal is broadcast at two frequencies referred to as L1 and L2. The L1 frequency is 1575.42 MHz, while the L2 frequency is 1227.60 MHz. All signals transmitted by the satellite are derived from the fundamental frequency f_0 of the satellite oscillator. Fundamental frequency is 10.23 MHz. The two sinusoidal carriers L1 and L2 are modulated with pseudo-random noise (PRN) codes and the navigation message. The coarse acquisition (C/A) code is transmitted on the L_1 signal. The encrypted P code is transmitted on both the L_1 and L_2 signals. Information such as the satellite clock corrections, the orbital parameters, and ionospheric modeling coefficients are transmitted on the signal.Elements of the two GPS signal are given in the following equations:

$$L_1(t) = A_1 P(t) N(t) \cos(2\pi f_1 t) + A_1 C/A(t) N(t) \sin(2\pi f_1 t)$$
$$L_2(t) = A_2 P(t) N(t) \cos(2\pi f_2 t)$$

$$(2.1)$$

where

$L_1(t), L_2(t)$ are the modulated L1 and L2 signals, respectively,

$A_{1,2}$ is the amplitude of L1 or L2,

$P(t)$ is the P code,

$N(t)$ is the navigation message (ephemerides),

$\cos(2\pi f_{1,2} t), \sin(2\pi f_1 t)$ are the unmodulated L1 or L2 signal, and

$C/A(t)$ is the C/A code.

The C/A-code (Coarse-Acquisition) is generated by the combination of two 10-bit tapped feedback shift registers, and a unique code is assigned to each satellite. The sequence has a length of 1023 bits. The time interval between two subsequent bits approximately corresponds to 300 meters. The C/A-code is intended for civilian users and is modulated only on L1.

The P-code is also generated by the combination of four 12-bit tapped feedback shift registers, but the length of the resulting sequence is approximately 2.3547×10^{14} bits, corresponding to a time span of about 266 days (Hungentobler et al., 2001). The time interval between two subsequent bits is 10 times smaller than that of the C/A-code. The precision of the P-code is therefore 10 times higher than that of the C/A-code. The P-code is modulated on both carriers L1 and L2. The access of the P-code is limited to U.S. military users and other authorized users through encryption.

The navigation message is 1500 bits long and the message is subdivided into five sub-frames. The navigation message contains information such as the transmission time, satellite clock correction, the satellite orbit parameters, the satellite health status, and various other data. The navigation message has a frequency of 50 Hz.

2.2 GPS OBSERVABLES

There are three GPS measurements: code, carrier phase, and Doppler measurements. The code pseudorange measurements are based on observations of the time taken for the GPS signal to travel from the satellite to the antenna. It is measured through comparison of the received signal with a reference carrier generated in the receiver and modulated with a copy of C/A-code, which is unique for each satellite and is known as pseudo-random noise (PRN) code. The code pseudorange measurements contain a number of errors. The code pseudorange measurement equation is given by Wells et al. (1987):

$$p = \rho + d\rho + c(dt\text{-}dT) + d_{ion} + d_{trop} + \varepsilon_p \qquad (2.2)$$

where

p is the measured pseudorange,

ρ is the geometric range (i.e. $\left\| r^s - R_r \right\|$),

$d\rho$ is the orbital error,

r^s, R_r are the position vector of satellite (known) and receiver (unknown), respectively,

dt, dT are the satellite and receiver clock errors, respectively,

d_{ion} is the ionospheric delay,

d_{trop} is the tropospheric delay, and

ε_p is the receiver code noise and multipath.

The phase measurements are based on processing the reconstructed signal carriers. The received signal is demodulated through correlation between the received signal and the PRN that is generated by the receiver. In order to recover the encrypted L2 signal, signal squaring or cross-correlation techniques are required. In the squaring technique, the received signal is multiplied by itself and will produce an unmodulated squared carrier with half the period. In the cross-correlation technique, the L1 signal is delayed to match with the L2 signal in the receiver to measure the travel time difference of the two signals (cf. Holmann-Wellenhof et al., 1994). Both squaring and cross-correlation techniques result in increased noise for the L2 pseudorange observations, as compared with direct correlation methods (Lachapelle, 2001).

The phase difference observables can be obtained from the beat frequency carrier. The receiver can measure only the fractional part of the carrier phase, and the exact number of integer wavelengths between the satellite and the receiver is not known. The unknown integer number of cycles to be added to the fractional phase measurement is called the initial phase ambiguity. The phase ambiguity will be constant as long as the receiver does not lose lock on the carrier transmitted by the satellite. If the initial integer ambiguity is resolved accurately, the precision of the phase range measurement is about 1-3 mm (Lachapelle, 2001). The phase measurement observation is given by Wells et al. (1987):

$$\Phi = \rho + d\rho + c\left(dt - dT\right) + \lambda N - d_{ion} + d_{trop} + \varepsilon_\Phi \qquad (2.3)$$

where

Φ is the observed integrated carrier phase range,

N is the integer ambiguity (cycles),

λ is the wavelength, and

ε_Φ is the receiver carrier phase noise and multipath.

The Doppler measurement is a measure of the instantaneous phase rate and the measurement is made in the phase lock loop. It is not affected by cycle clips and does not have any phase ambiguity. Basically, it is used for velocity estimation and cycle slip detection. The Doppler measurement (in m/s) equation is given below.

$$\dot{\Phi} = \dot{\rho} + d\dot{\rho} + c(\dot{dt} - \dot{dT}) - \dot{d}_{ion} + \dot{d}_{trop} + \dot{\varepsilon}_{\Phi} \tag{2.4}$$

where

$\dot{\Phi}$ is the measured Doppler,

$\dot{\rho}$ is the geometric range rate(i.e. $\left\| r^s - R_r \right\|$),

$d\dot{\rho}$ is the orbital error drift,

$\dot{dt}$ is the satellite clock error drift,

$\dot{dT}$ is the receiver clock error drift,

$\dot{d}_{ion}$ is the ionospheric delay drift,

$\dot{d}_{trop}$ is the tropospheric delay drift, and

$\dot{\varepsilon}_{\Phi}$ is the noise (1-5 mm/s).

2.3 GPS ERRORS

There are biases and errors influencing the GPS measurements, which limit the achievement of millimeter-level positioning accuracy. The major error sources of the GPS measurements are signal propagation errors due to the troposphere and ionosphere, orbital errors, satellite clock errors, multipath and receiver noise errors. These biases and errors are described in the following sections.

2.3.1 Orbital Errors

The orbit quality is considered to be one of the primary accuracy-limiting factors in the GPS measurements. Orbital errors occur when the GPS message does not transmit the correct orbital parameters. The rule of thumb, which gives the error Δx in a component of a baseline of length l as a function of an orbit error of size ΔX (Bauersima, 1983) is represented by the following expression:

$$\Delta x = \frac{1}{d} \Delta X \tag{2.5}$$

where d is the approximate distance between the satellite system and the survey area.

There are several ways to define the satellite orbits for determination of the position using GPS measurements. The broadcast ephemeris is transmitted in the navigation message. The broadcast ephemeris uses Keplerian elements to represent the satellite orbits and incorporates additional terms to account for the effects of the perturbing forces. The main Keplerian elements are square root of the semi-major axis, eccentricity, mean anomaly at reference time, inclination angle at reference time, right ascension at reference time, and argument of perigee. The navigation message is generated based on observations at five ground-based monitor stations of the GPS control segment. The master control station is responsible for the computation of the ephemeris and satellite clock corrections, and the ground stations upload them to the satellites. The broadcast ephemeris is normally produced every hour and typical errors in the broadcast ephemeris are found to be 3 metres (Hugentobler et al., 2001).

The post-mission orbits give more accurate satellite positions. There are different agencies which provide post-mission orbits. The post-mission orbits are calculated using observations in an extended tracking network of GPS stations worldwide. The Center for

Orbit Determination in Europe (CODE), the National Geodetic Survey (NGS), and the International GPS Service (IGS) provide post-mission orbit solutions. The ultra-rapid orbits are generated twice each day and contain 48 hours of orbits; the first 27 hours are based on observations and the second 21 hours are predicted. Accuracies of ultra-rapid, rapid, and final orbits have been determined by Hugentobler et al. (2001).The accuracy of ultra-rapid orbits is at a level of 20 cm. The rapid orbits are available after a delay of one or two days of data collection with an accuracy of approximately 10 cm. The final orbits are the most accurate orbits with accuracies at a level of less than 5 cm. The final orbits are available after two weeks once the data is collected and the necessary analyses are conducted. The final orbits used in this thesis are the products of IGS and National Geodetic Survey (NGS).

2.3.2 Satellite Clock Error

Satellite clock errors arise from instabilities in the oscillators of the GPS satellites, such that ranging errors are observed in user's measurements. The satellite clock error can be determined using the coefficients transmitted in the satellite navigation message. The satellite clock error can be determined using the following equation:

$$dt = a_{f_0} + a_{f_1}(t\text{-}t_{oc}) + a_{f_2}(t\text{-}t_{oc})^2 + d_{rel} - t_{gd} \qquad (2.6)$$

where

dt   is the satellite clock error,

a_{f_0} is the zero order coefficient,

a_{f_1} is the first order coefficient,

a_{f_2} is the second order coefficient,

t   is the time of measurement,

t_{oc} is the time of ephemeris,

d_{rel} is the relativity correction, and

t_{gd} is the group delay.

The clock errors computed using the broadcast navigation message are not accurate because the coefficients are predicted in time. If the broadcast coefficients were adequately modeled, the typical satellite clock error would be 10 ns (Hugentobler et al., 2001). The observed satellite clock error will be same for all receivers tracking the same satellite at the same instant.

Relativity and group delay contribute to the satellite clock error. The relativity effect occurs due to an apparent frequency shift in the satellite oscillator. The group delay correction is necessary to compensate for inter-frequency biases in the satellite transmitter.

The satellite clock error can be removed by computing single differences of GPS observations between receivers. Also, the satellite clock error may be estimated post-mission using the precise clocks. Precise clocks are computed with the precise/final orbits. In this thesis, the precise clocks of 15 minutes interval from the National Geodetic Survey (NGS) and the International GPS Service (IGS) were computed and used for data pre-processing.

2.3.3 Tropospheric Error

The troposphere is the neutral region of the Earth's atmosphere extending from the Earth's surface up to 50 kilometres. When GPS signals propagate through the troposphere, they experience range delays dependent on the pressure, temperature and moisture content along the signal path. The tropospheric delay is generally split into hydrostatic and wet components. The hydrostatic delay is due to the dry gases in the troposphere and the non-dipole component of water vapor refractivity and can be modeled accurately using surface temperature, pressure, and humidity measurements. However, the wet delay is caused by

the presence of water vapor and it exists up to 10 km from the surface of the Earth. Water vapor is highly variable in space and time such that the wet delay cannot be modeled using surface measurements very accurately (Bevis et.al., 1994).

Tropospheric delay has a great impact on GPS precise positioning because the troposphere is a non-dispersive medium at GPS frequencies and the delay cannot be eliminated using a combination of observations on two frequencies. Different models such as the Hopfield model (1969), Saastamoinen model (1973), and modified Hopfield model (Goad and Goodman, 1974) are used to estimate the tropospheric error (Hoffmann-Wellenhof et al., 2000). The dry part of the delay component can be determined with the accuracy of few millimetres; however the wet part of the delay component can only be estimated with an accuracy of 10-20%. Detailed discussion of the physics of the troposphere and the different troposphere models are given in Chapter 3. Accurate estimation of the tropospheric wet delay using GPS observations is the focus of this thesis.

2.3.4 Ionospheric Error

The ionosphere is the layer of the Earth's atmosphere extending from 50 km to 1000 km altitude. The ionosphere contains weakly ionized plasma of electrons and ions created primarily by the presence of ionizing solar radiation. GPS signals are affected as they pass through the ionosphere resulting in range errors. The magnitude of error depends on the signal frequency and the density of free electrons along the signal path. The electron density integrated in a vertical column with a cross-sectional area of one square metre is known as the total electron content (TEC). The major effects of the ionosphere are the carrier phase advance and group delay of pseudorange. The phase advance and group delay are equal in magnitude and opposite in sign. The pseudorange ionospheric group delay ranges from 1 to 100 m (Lachapelle, 2001). GPS ionospheric range errors are a function of the TEC along the signal path and the signal frequency.

Different layers or regions of the ionosphere exist. These regions are known as the D, E, and F regions and the locations of these regions vary for daytime versus nighttime. Figure 2.2 shows different layers or regions in the ionosphere. The D region is the lowest region of the ionosphere extending from 50 to 90 km. The D region has no significant effect on GPS frequencies; however, it absorbs radio signals at frequencies up to the low VHF band. The E region extends from 90 to 140 km, and is produced at high latitudes by solar particle precipitation in the auroral region; the aurora is associated with scintillation effects on GPS frequencies. Radio operators may use the E region as a surface to reflect signals to distant stations. The F region is divided into two regions: the F1 and F2 region. The F1 region extends from 140 km to 210 km, and contributes 10% of the total ionospheric delay experienced by GPS signals. The F2 region extends from 210 km to 1000 km and is mainly produced from the ionization of atomic oxygen. The highest electron densities are generally observed at heights from 250 km to 400 km. This region is highly variable and contributes the majority of the delay on GPS frequencies.
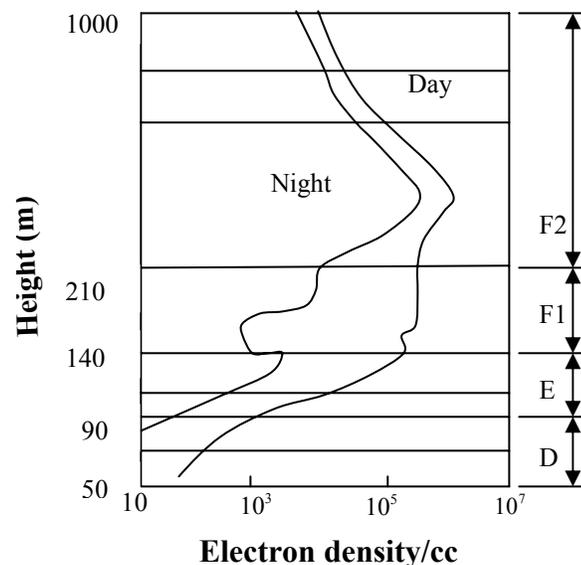
Figure 2.2 Ionosphere layers.

The variation of TEC and ionospheric effects on GPS signals depends on different ionospheric characteristics. The electron density is directly proportional to the rate of ionization, which depends on the level of solar radiation, and solar wind characteristics (in auroral and polar regions). In the daytime, solar radiation is high and creates free electrons; the electrons recombine with ionospheric ions in the nighttime local time sector. The highest number of free electrons occurs at approximately 14:00 local time, and a secondary maximum may occur at 22:00 local time in the equatorial region. The TEC also depends on the season and geographic location. Electron densities are highest at spring equinox and two maxima in TEC are located at ±20 degrees magnetic latitude. Electron densities also increase by a factor of 3 in the period of solar maximum. A larger number of sunspots appear in the period of solar maximum than in the period of solar minimum. TEC at mid-latitudes varies about 25% from monthly mean values due to variations in temperature and recombination processes. The measured TEC can be in the range 10^{16} to 10^{19} el/m^2; these values represent the extremes of observed values in the Earth's ionosphere (Klobuchar, 1996). Figure 2.3 shows the worldwide distribution of TEC at 13:00 UT on September 27, 2001.
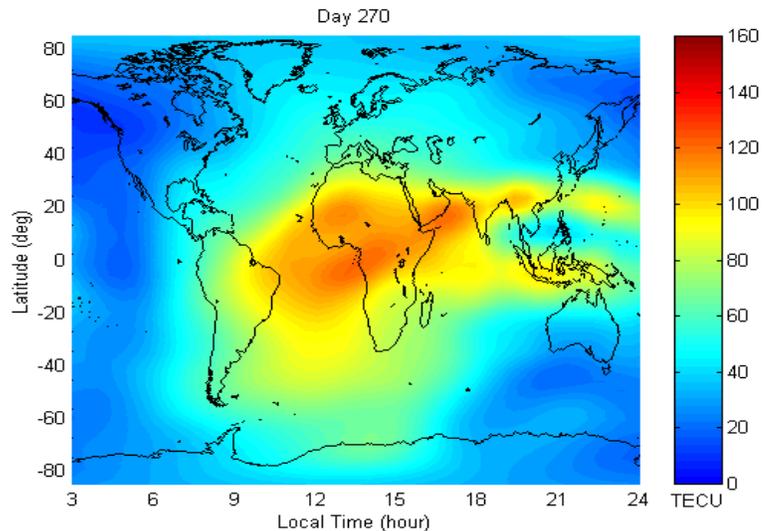
Figure 2.3 Worldwide distribution of TEC, 1300 UT on Sept. 27, 2001.

The ionosphere is a dispersive medium: the delay depends on the frequency of the radio signal. In order to specify the propagation effects on a radio wave travelling through the ionosphere, the following equation for the refractive index of the medium given by Appleton and Hartree (Klobuchar, 1996) can be used.

$$n^2 = 1 - \frac{X}{1 - iZ - \frac{Y_T^2}{2(1-X-iZ)} \pm \left[\frac{Y_T^4}{4(1-X-iZ)^2} + Y_L^2 \right]^{1/2}}$$

(2.7)

where $X = N_e E^2 / \varepsilon_0 m \omega^2$, $Y_L = f_H \cos\theta / f$, $Y_T = f_H \sin\theta / f$, $Z = \upsilon / \omega$, $\omega = 2\pi f$, and

f   is the frequency of the signal,

E   is the electron charge,

ε_0 is the permittivity of free space,

m   is the mass of an electron,

θ is the angle of the ray with respect to the Earth's magnetic field,

N_e is the ionospheric electron density,

υ is the electron-neutral collision frequency, and

f_H is the electron gyro frequency.

The ionospheric refractive index can be determined with an accuracy of better than 1% using the following approximation:

$$n = 1 - (X/2)$$

(2.8)

The ionospheric group delay can then be determined using the following equation (Lachapelle, 2002):

$$\Delta t = \frac{40.3}{f^2} TEC$$

(2.9)

where

Δt is the ionospheric time delay,

f   is the frequency of the signal,

c   is the speed of light,

TEC   is the total electron content,

The temporal and spatial variations of TEC in the ionosphere cause variations in the ionospheric time delay for the GPS measurements. The phase of the carrier signal is advanced when it passes through the ionosphere. The carrier phase advance can be expressed using the following equation (Lachapelle, 2000):

$$\Delta\phi = \frac{1.34 \times 10^{-7}}{f} \text{TEC} \tag{2.10}$$

where $\Delta\phi$ is phase shift due to the ionospheric refractive index.

In addition to group delay and phase advance of the radio signal, the other effects of the ionosphere are absorption, Faraday rotation or change in plane of polarization, Doppler shift, refraction or bending of the radio waves, and scintillation. Ionospheric scintillations are rapid fluctuations in the phase and amplitude of signals and are caused by electron density irregularities in the ionosphere. The effects of ionospheric scintillations might be observed as the loss of phase lock due to lower signal strength, or due to Doppler shift outside the bandwidth of the phase lock loop.

The ionospheric effects can be virtually eliminated using dual frequency data to correct the pseudorange measurements. The ionospheric correction removes the first order ionospheric effect, but it increases the noise on the ionospherically corrected pseudorange. The

ionospheric correction can be applied on the L1 carrier phase at a given epoch using dual frequency carrier phase observations and known carrier phase ambiguities for L1 and L2. However, the differential ionospheric delay correction can be applied using both L1 and L2 carriers without knowing the ambiguities in a float ambiguity positioning approach. The broadcast ionospheric model removes over 50% of the ionospheric delay at mid-latitude regions. The wide area DGPS ionospheric grid model may also be used to estimate ionospheric delays for individual satellites at a user's location (Skone, 1998).

2.3.5 Receiver Noise

Receiver noise is a random error generated by the receiver as it processes the received signal to derive pseudorange and carrier phase measurements. It is considered as white noise because the errors are not correlated over time. There is also no correlation between the code measurements and phase measurements taken at the same time in a given receiver because these measurements are derived using separate tracking loops. The noise in the code measurements can be isolated from all other errors using a "zero-baseline" concept where two receivers are connected to the same antenna. The noise for the code measurements can be calculated from the double difference pseudorange using the following equation:

$$\sigma_{\varepsilon_P} = 0.5\sigma_{\Delta\nabla P_{rx}} \tag{2.11}$$

where

σ_{ε_P} is the measurement noise to account for double difference pseudorange, and

$\sigma_{\Delta\nabla P_{rx}}$ is the noise variance.

The receiver noise for C/A-code measurements is in the range 30-300 cm and for P-code, the values are 3-30 cm. For carrier phase L1, the phase noise would be 0.5-3 mm in a

survey-grade receiver. The noise level of the code and phase measurements decreases as the elevation angle increases up to about $45°$ and the noise level becomes constant above $45°$ elevation (Lachapelle, 2001).

2.3.6 Multipath Error

Multipath is the result of GPS signals arriving at an antenna from more than one direction due to signal reflection or diffraction at various objects. In secular multipath, the incident ray remains parallel after reflection from smooth sources. In the case of diffuse multipath, the energy of the signal is scattered in many directions due to roughness of the reflecting surface, resulting in the reduction of field strength in the direction of the antenna.
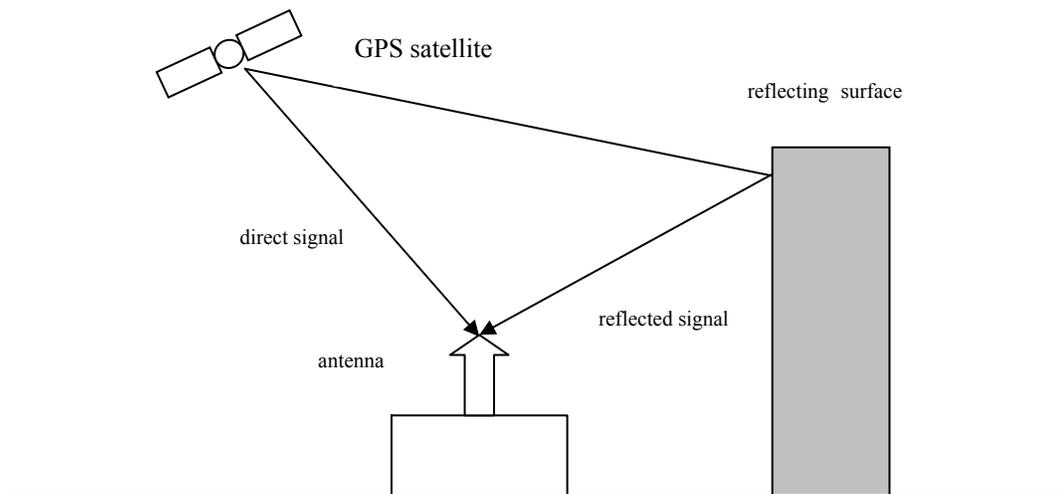
Figure 2.4 Multipath.

Multipath has been a major source of error in precise GPS applications and a limiting factor for many DGPS applications. Multipath distorts the signal modulation and degrades the accuracy in pseudorange code measurements and carrier phase measurements, and it cannot be reduced through differential processing. Pseudorange multipath shows up as a systematic error in the GPS measurements and is correlated from day to day if the

measurements are taken in the same environment. It can reach the magnitude of about 15 m for code measurements and ¼ wavelength for phase measurements (Ray, 2000). This error can affect the ability to resolve integer ambiguities and, ultimately, degrade the accuracy of precise positioning and attitude determination. The superposition of direct and reflected signals can be used to determine the multipath error as expressed by the following equation:

$$A_\Sigma = \beta A \cos\left(\Phi_D + \Theta\right) \qquad\qquad (2.12)$$

where

A_Σ is the received signal,

A is the direct signal amplitude,

Φ_D is the phase of direct signal,

β is the attenuation due to multipath, and

Θ is the phase shift due to multipath.

The phase shift due to multipath Θ is given by:

$$\Theta = \arctan\left(\frac{\sin\Phi}{\alpha^{-1} + \cos\Phi}\right) \qquad\qquad (2.13)$$

The maximum multipath error occurs when α is equal to unity; hence maximum theoretical multipath error is $90°$ or 5 cm for L1 measurements. However, typical phase multipath is in the order of 1 cm and less in real applications (Lachapelle, 1994).

The multipath effects can be minimized by choosing the site of observation with minimum obstructions and reflecting surfaces nearby. Using a ground plane antenna or choke ring can minimize the multipath effects. Narrow correlator spacing technology may be applied in the GPS receiver to reduce the multipath effects (van Dierendonck et al., 1992). Different

multipath techniques have been developed to mitigate the multipath effects. Ray et al. (1998) have developed a system to estimate multipath parameters based on an array of closely spaced antennas in static mode.

2.4 FORMING DIFFERENCES OF GPS OBSERVATIONS

Two or more receivers are used to form differences of GPS observations. One receiver, usually at rest, is located at the reference station and the remote receiver is usually roving. Differences of the original GPS observations are formed to eliminate or reduce some errors. When differences of GPS observations are formed, orbital errors, ionospheric errors and satellite clock errors are either reduced or eliminated but receiver noise and multipath are not reduced or eliminated in the observations.

2.4.1 Single Differences

Single differences between receivers are formed from subtracting pseudorange or phase observations between the reference station and a remote station. Forming single differences reduces orbital errors, ionospheric errors and tropospheric errors, and eliminates satellite clock errors. However, it does not reduce receiver noise. The pseudorange and phase single difference observations can be expressed using following equations (Lachapelle, 2001):

$$\Delta = (\bullet)_{rx1} - (\bullet)_{rx2}$$
$$\Delta\rho = \Delta\rho + \Delta d\rho - c\Delta dT + \Delta d_{ion} + \Delta d_{trop} + \varepsilon_{\Delta\rho} \qquad (2.14)$$
$$\Delta\Phi = \Delta\rho + \Delta d\rho - c\Delta dT + \lambda\Delta N - \Delta d_{ion} + \Delta d_{trop} + \varepsilon_{\Delta\Phi}$$

where $\Delta\rho$ and $\Delta\Phi$ are single differences for pseudorange and phase observations, respectively.

Figure 2.5 shows single differences of GPS observations between receivers.
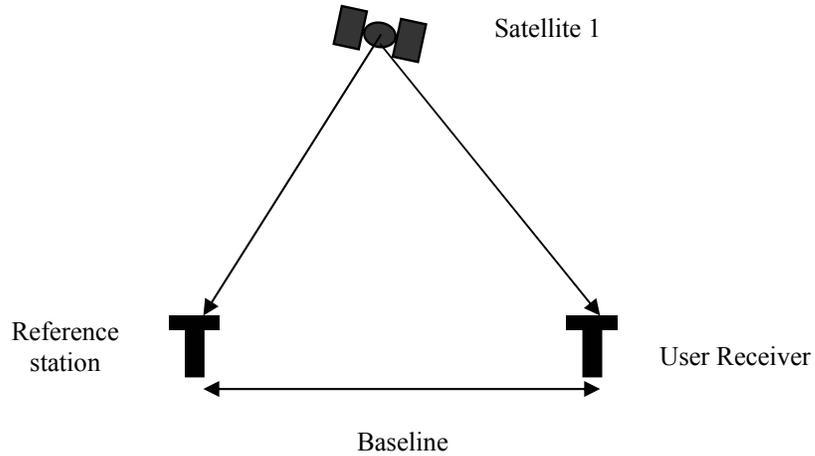
Figure 2.5 Single difference.

2.4.2 Double Differences

Satellite-receiver double differences are mainly used for precise static and kinematic differential GPS. By forming the double-difference observations, the receiver clock errors and the satellite clock errors are eliminated, and the orbital errors, ionospheric errors and tropospheric error are reduced (Hugentobler et al., 2001). The pseudorange and phase double difference observations can be expressed using following equations (Lachapelle, 2001):

$$\Delta\nabla = \left\{ (\bullet)_{sat2} - (\bullet)_{sat1} \right\}_{rx2} - \left\{ (\bullet)_{sat2} - (\bullet)_{sat1} \right\}_{rx1}$$

$$\Delta\nabla\rho = \Delta\nabla\rho + \Delta\nabla d\rho + \Delta\nabla d_{ion} + \Delta\nabla d_{trop} + \varepsilon_{\Delta\nabla\rho}$$

$$\Delta\nabla\Phi = \Delta\nabla\rho + \Delta\nabla d\rho + \lambda\Delta\nabla N - \Delta\nabla d_{ion} + \Delta\nabla d_{trop} + \varepsilon_{\Delta\nabla\Phi}$$

(2.15)

where $\Delta\nabla\rho$ and $\Delta\nabla\Phi$ are double differences for pseudorange and phase observations, respectively.

Figure 2.6 shows double differences of GPS observations between satellites and receivers.
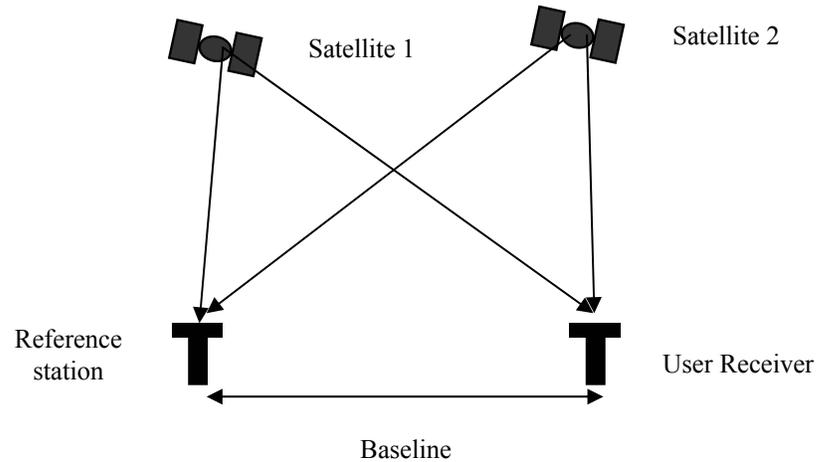
Figure 2.6 Double difference.

2.4.3 Triple Differences

The triple difference of the phase measurements are formed using double difference observations from two different epochs t_1 and t_2. In the triple difference, the satellite and receiver clock errors are eliminated. Phase ambiguities are also eliminated if the receivers did not lose lock during this time interval and if no cycle clip occurred (Hungentobler et al., 2001). The ionospheric and tropospheric errors are reduced forming triple difference observations. The phase triple difference observations can be expressed using the following equations (Lachapelle, 2001):

$$\delta\Delta\nabla = \left[\left\{(\bullet)_{sat2} - (\bullet)_{sat1}\right\}_{rx2} - \left\{(\bullet)_{sat2} - (\bullet)_{sat1}\right\}_{rx1}\right]_{t_1} -$$
$$\left[\left\{(\bullet)_{sat2} - (\bullet)_{sat1}\right\}_{rx2} - \left\{(\bullet)_{sat2} - (\bullet)_{sat1}\right\}_{rx1}\right]_{t_2}$$
$$\delta\Delta\nabla\Phi = \delta\Delta\nabla\rho + \delta\Delta\nabla d\rho - \delta\Delta\nabla d_{ion} + \delta\Delta\nabla d_{trop} + \varepsilon_{\delta\Delta\nabla\Phi}$$

(2.16)

where $\delta\Delta\nabla\Phi$ is triple difference phase observation.

Figure 2.7 shows triple differences of GPS observations between satellites and receivers for two different epochs t_1 and t_2.
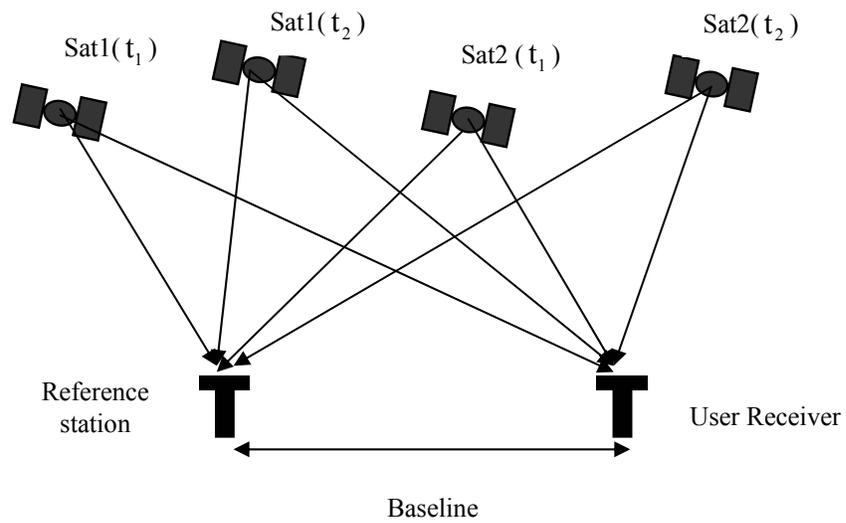
Figure 2.7 Triple difference.

CHAPTER 3

TROPOSPHERIC MODELING

The GPS signal is refracted as it propagates through the Earth's atmosphere. The signal bends from its original path and experiences velocity variations as it passes through regions of different refractive indices in the troposphere and the ionosphere. An ionospheric delay is caused by the presence of ionized gas molecules in the ionosphere, and it is dispersive at radio frequencies, meaning that the refractive index depends on the signal frequency. The ionospheric delay is dependent on the density of free electrons. The ionospheric delay can be removed using a linear combination of observations on two GPS frequencies.

The troposphere is a non-dispersive medium and the delay caused by the troposphere (due to combined variability of the refractive indices in the troposphere, the tropopause and the stratosphere) cannot be removed using a combination of two GPS frequencies. The tropospheric delay is generally classified as hydrostatic and wet components. The hydrostatic delay is due to the dry gases in the troposphere and the non-dipole component of water vapor refractivity, and can be modeled accurately using surface pressure measurements. However, the wet delay, which is mostly due to water vapor, is highly variable and cannot be modeled from surface measurements. A simple model can estimate the approximate tropospheric delay, which is sufficient for low-accuracy positioning. The distribution of water vapor should be known precisely to model the wet delay for high-accuracy positioning.

In this chapter, a general overview of the structure of the troposphere is presented with an introduction of the tropospheric refractive index. The effect of the tropospheric components on the path of a GPS signal is derived with mathematical expressions. The estimation of the delay components is explained for different models and mapping functions.

3.1 TROPOSPHERE AND ITS STRUCTURE

The neutral atmosphere consists of several vertical layers, and these layers are defined by their characteristics such as temperature, pressure, and chemical composition. The closest layer to the Earth is the "troposphere", which begins at the Earth's surface and extends up to approximately 9 kilometers. The region at 7 kilometers altitude (or higher), at the top of troposphere, is called the tropopause. The tropopause has some characteristics of the both the "troposphere" and stratosphere. The stratosphere extends from 16 km up to 50 km above the Earth's surface. The "troposphere", tropopause, and stratosphere are considered as the neutral atmosphere because they are electrically neutral. In GPS terminology, the term troposphere generally refers to the neutral atmosphere extending from the Earth's surface to 50 km altitude. This more inclusive definition of the troposphere is used in this thesis. Figure 3.1 shows the different layers in the troposphere. The atmosphere is dominated by charged particles above the stratosphere, and is called the ionosphere. The mesosphere is located in the lower ionosphere, and extends from 50 km up to 80 km above the Earth's surface. Above the mesosphere is the remainder of the ionosphere, which extends up to 1000 kilometres.
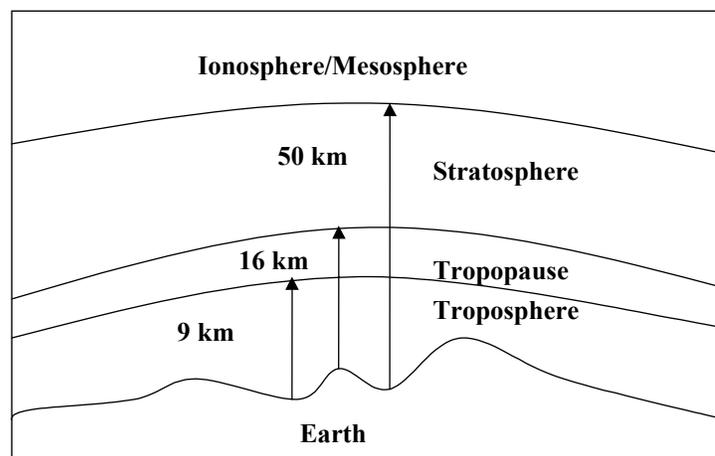
Figure 3.1 Vertical structure of the atmosphere.

The troposphere (altitudes below 10 km) contains 75 percent of the atmosphere's mass and most of the atmosphere's water vapor. Water vapor concentration varies from trace amounts in polar regions to nearly 4 percent in the tropics. The most prevalent gases are nitrogen (78 percent) and oxygen (21 percent), with the remaining 1 percent consisting of argon (0.9 percent), and traces of hydrogen ozone, a small amount of carbon dioxide, and other constituents. Figure 3.2 shows the atmospheric constituents in the atmosphere up to 1000 km altitude.
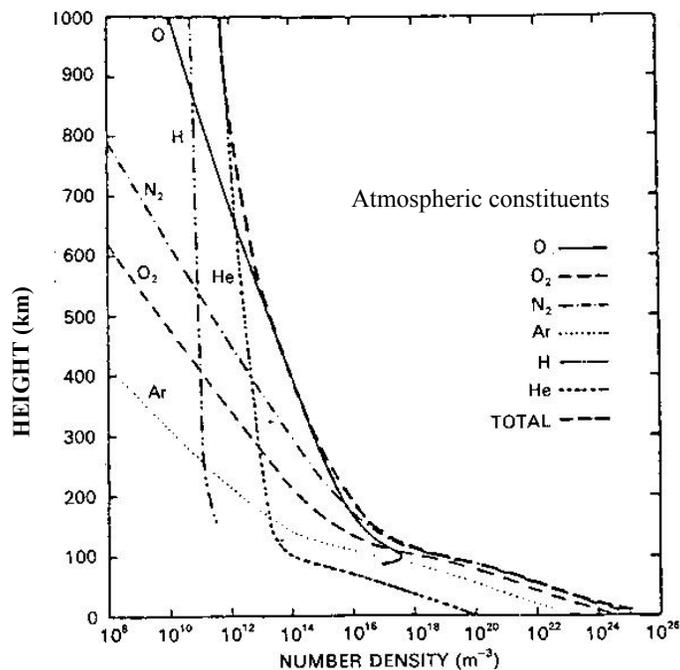
Figure 3.2 Atmospheric constituents (Richmond, 1983).

Water vapor plays a major role in regulating air temperature because it absorbs solar energy and thermal radiation from the Earth's surface. The temperature in the troposphere decreases rapidly with altitude at a constant lapse rate of $-5°$ to $-7°C$ per km of altitude from sea level up to the tropopause. The tropopause is a region of constant temperature rate. In the stratosphere, the temperature rate rises from $+1°$ to $+2°C$ per km, due to heating through ozone absorption, and the temperature is roughly $0°C$ at the height of 50 km from

the Earth's surface. Figure 3.3 shows thermal profiles of the troposphere with appropriate altitude of temperature regions.
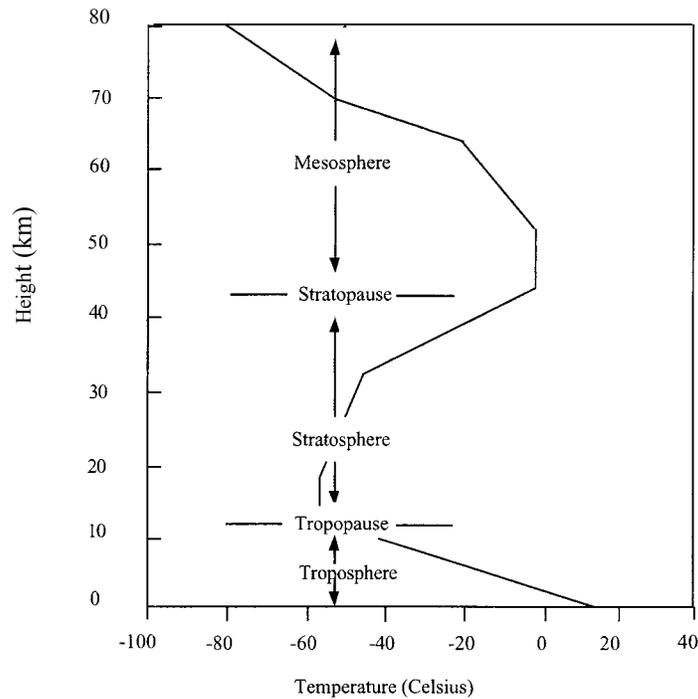
Figure 3.3 Vertical temperature profiles.

3.2 TROPOSPHERIC EFFECTS ON GPS SIGNALS AND REFRACTIVITY

3.2.1 Refractive Index and Refractivity

The refractive index of a medium, n, is defined as the ratio of the speed of propagation of an electromagnetic wave in a vacuum, c, to the speed of propagation in this medium, v:

$$n = \frac{c}{v} \qquad (3.1)$$

As the electromagnetic waves in the atmosphere propagate just slightly slower than in a vacuum, the refractive index is more conveniently expressed by the term refractivity, N:

$$N = 10^6 (n\text{-}1) \qquad (3.2)$$

The refractivity can be derived using following expression (Smith and Weintraub, 1953):

$$N = K_1 \frac{P_d}{T} + K_2 \frac{e}{T} + K_3 \frac{e}{T^2} \qquad (3.3)$$

where

P_d is the partial pressure due to dry gases, including CO_2,

K_i are the refractivity constants,

e is the partial pressure of water vapor, and

T is the absolute temperature.

The total refractivity is the sum of the hydrostatic components and wet components of the refractivity. If we take into account the compressibility factors, Z_d and Z_w, for the non-ideal gases, then we can express the equation of refractivity as follows:

$$N = K_1 \left(\frac{P_d}{T} \right) Z_d^{-1} + \left[K_2 \left(\frac{e}{T} \right) + K_3 \left(\frac{e}{T^2} \right) \right] Z_w^{-1} \qquad (3.4)$$

where Z_d and Z_w are empirical factors and are usually modeled as a function of pressure and temperature:

$$Z_d^{-1}=1+P_d\left[57.97\times10^{-8}\left(1+\frac{0.52}{T}\right)-9.4611\times10^{-4}\frac{T_c}{T}\right] \tag{3.5}$$

$$Z_w^{-1}=1+1650\frac{e}{T^3}\left[1-0.0137T_c+1.75\times10^{-4}T_c^2+1.44\times10^{-6}T_c^3\right] \tag{3.6}$$

where T_c is the temperature in degrees Celsius.

The refractivity constants K_i are determined empirically in a laboratory. Table 3.1 summarizes the most significant recent evaluations of the refractivity constants (Mendes, 1999):

Table 3.1 Determination of the Refractivity Constants

Reference	$K_1\,(K\,h\,Pa^{-1})$	$K_2\,(K\,h\,Pa^{-1})$	$K_3\,(K\,h\,Pa^{-1})$
Boudouris (1963)	77.59 ± 0.08	72 ± 11	3.75 ± 0.03
Smith and Weintraub (1953)	77.61 ± 0.01	72 ± 9	3.75 ± 0.03
Thayer (1974)	77.60 ± 0.01	64.79 ± 0.08	3.776 ± 0.004
Hill et al. (1982)	-	98 ± 1	3.583 ± 0.03
Hill (1988)	-	102 ± 1	3.578 ± 0.003

3.2.2 Tropospheric Delay

When the GPS signal propagates through the Earth's troposphere, it is affected significantly by the variability of the refractive index of the troposphere. The tropospheric delay is due to the excess path delay and the bending effects on the radio signal (Mendes, 1999). The refractive index of the troposphere is greater than unity causing an excess delay of the signal, and the change in the refractive index with height causes the bending of the signal. The tropospheric delay is directly proportional to the refractive index or refractivity and can

be expressed as a function of atmospheric temperature and pressure. The tropospheric delay can be computed through the integration along the signal path through the troposphere using following expression:

$$d_{trop} = \int_{Path} (n-1)\, ds \qquad (3.7)$$

where n is the refractive index. The equation can be expressed in terms of the refractivity, N:

$$d_{trop} = 10^{-6} \int_{Path} N\, ds \qquad (3.8)$$

The tropospheric delay can be separated into two main components: the hydrostatic delay and the wet delay. The hydrostatic delay is caused by the dry part of the atmospheric constituents and can be estimated precisely using surface temperature and pressure measurements. By removing the hydrostatic delay from the total tropospheric delay, the remaining signal delay is called the wet delay, mostly due to water vapor in the troposphere.

The tropospheric delay is therefore often represented as a linear combination of the hydrostatic and wet components:

$$d_{trop} = 10^{-6} \int_{Path} N_h\, ds + 10^{-6} \int_{Path} N_w\, ds \qquad (3.9)$$

The tropospheric delay is represented in terms of the delay calculated in the zenith direction over the antenna on the ground; hence the zenith tropospheric delay is a combination of the zenith hydrostatic delay d_h^z and the zenith wet delay d_w^z.

$$d_{trop}^{z} = d_{h}^{z} + d_{w}^{z} \qquad\qquad (3.10)$$

The slant tropospheric delays at arbitrary elevation angles can be expressed in terms of the zenith delays and mapping functions. This representation allows the use of separate mapping functions for the hydrostatic and wet delay components:

$$d_{trop}^{s} = m_{h}\left(\varepsilon\right) \times d_{h}^{z} + m_{w}\left(\varepsilon\right) \times d_{w}^{z} \qquad\qquad (3.11)$$

where

$m_{h}\left(\varepsilon\right)$ is the hydrostatic mapping function, and

$m_{w}\left(\varepsilon\right)$ the wet mapping function.

Normally, the total zenith tropospheric delay is about 2.50 m, where about 90% of this value is caused by the zenith hydrostatic delay, and approximately 10% of this value is caused by the zenith wet delay (Skone, 2001). As satellites decrease in elevation toward the horizon, the slant hydrostatic delay or the slant wet delay increases significantly. Figure 3.4 shows how the slant wet delay changes with an elevation angle for the Satellite PRN 1 on May 25, 2002 (Day 145). The slight jump in slant wet delay below $40°$ is because of discontinuities in the hourly batch estimates of wet delay. The zenith wet delay is found about 5 cm because the atmosphere is relatively dry in Calgary.
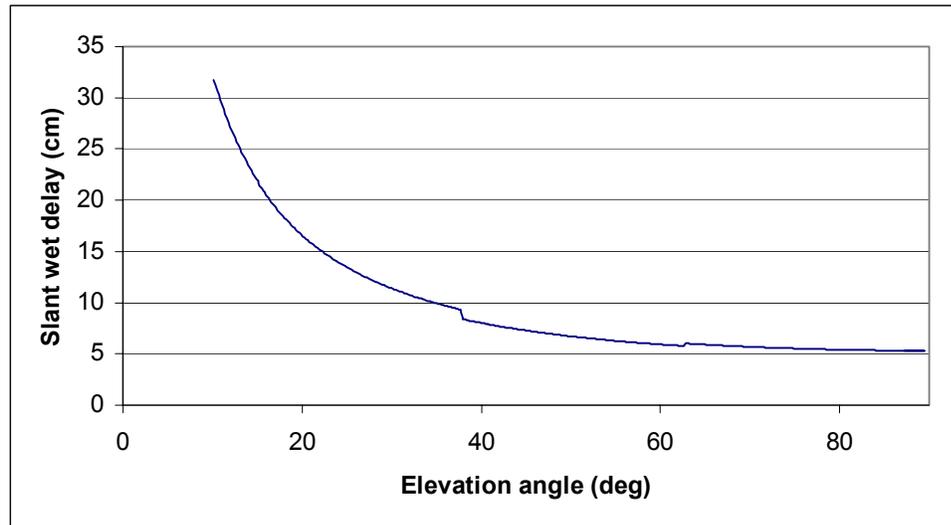
Figure 3.4 Slant wet delay as a function of elevation angle.

3.3 TROPOSPHERIC MODEL

It is difficult to measure the refractivity directly along the signal path. Various tropospheric models have been developed to represent the integrated tropospheric delay. Generally, surface meteorological parameters, such as pressure, temperature, and humidity are required input for these models. The zenith hydrostatic delay contributes about 90% of the total delay to the tropospheric delay (Skone, 2001). Zenith hydrostatic delay models can be estimated with accuracies better than 1% where the zenith hydrostatic delay is considered to be a function of the surface pressure, and in some cases temperature, and hydrostatic equilibrium is assumed. The zenith wet delay contributes about 10% of the total delay, and the zenith wet delay models have accuracies of 10-20%. The wet component depends on water vapor, which is highly variable with the space and time and is difficult to model. Some troposphere models are briefly explained below:

3.3.1 Hydrostatic Models

3.3.1.1 Saastamoinen Model

If hydrostatic equilibrium is assumed, the hydrostatic delay model may be expressed simply as a function of measured surface pressure. Saastamoinen (1973) employed this approach and used the following representation of gravity g_m in the zenith hydrostatic model.

$$g_m = 9.784\left(1 - 0.0026\cos 2\varphi - 0.00000028 H_s\right) \tag{3.12}$$

where φ is the latitude of the station and H_s is the station height above sea level, in metres. She used the refractivity constant given by Essen and Froome (1951) to determine the following expression for the zenith hydrostatic delay:

$$d_h^z = \frac{0.002277 P_s}{\left(1 - 0.0026\cos 2\varphi - 0.00000028 H_s\right)} \tag{3.13}$$

where P_s is the surface pressure.

3.3.1.2 Davis et al. Model

The Davis et al. (1985) model differs from the Saastamoinen model only in the choice of refractivity constant. Davis el al. used the K_1 refractivity constant given by Thayer (1974) and the zenith hydrostatic model is given by the following expression:

$$d_h^z = \frac{0.0022768 P_s}{\left(1 - 0.0026\cos 2\varphi - 0.00000028 H_s\right)} \tag{3.14}$$

3.3.1.3 Baby et al. Model

The acceleration of gravity used in the Baby et al. (1988) model can be expressed as:

$$g_m = \frac{g_s}{1 + \frac{2}{r_s \sigma (\mu + 1)}} \qquad (3.15)$$

where

g_s is the surface gravity at the station, and

r_s is the mean geocentric radius of the station in metres.

μ and σ are given by the following expressions:

$$\mu = \frac{g_s}{R_d \alpha} \left[1 - \frac{2}{r_s \sigma} \right] \qquad (3.16)$$

$$\sigma = \frac{\alpha}{T_s} \qquad (3.17)$$

where

α is the lapse rate,

T_s is temperature at the station in Kelvin,

r_s is the mean geocentric radius of the station in metres and

R_d is specific gas constant of dry air

Using the K_1 refractivity constant developed by Bean and Dutton (1966), the zenith hydrostatic delay model is given by the following expression:

$$d_h^z = \frac{0.022277P_s}{g_s}\left[1+\frac{2}{r_s\sigma(\mu+1)}\right] \tag{3.18}$$

Baby et al. (1988) also gave the semi-empirical model for the zenith hydrostatic delay model, which provides improved precision compared to the theoretical model. The semi-empirical model can be represented by the following expression:

$$d_h^z = 10^{-3}U_s 10^{\gamma v} \tag{3.19}$$

where γ and v are empirical coefficients, and are associated with seasonal and climatic variations.

3.3.1.4 Hopfield Model

Hopfield (1969) assumed that the theoretical dry refractivity profile could be expressed using a quartic model:

$$N_d = N_{ds}\frac{\left(H_d^e - H\right)^4}{\left(H_d^e\right)^4} \tag{3.20}$$

where $H_d^e = 40136 + 148.72(T-273.16)$, N_{ds} is the dry refractivity on the surface and H is the height above sea level, in kilometres.

Using the refractivity constant determined by Smith and Weintraub (1953), the final expression for the zenith dry delay model can be represented by the following expression:

$$d_d^z = 77.6 \times 10^{-6} \frac{P_s}{T_s} \frac{H_d^e}{5}$$ (3.21)

where P_s is the surface pressure, and T_s is the surface temperature.

3.3.1.5 Modified Hopfield Model

The Modified Hopfield model (Goad et al., 1974) introduced lengths of position vectors instead of heights. If R_E is the radius of the Earth, h is the height corresponding to the wet part of the atmosphere, H_d is the height corresponding to the dry part of the atmosphere, then the corresponding lengths are $r_d = R_E + h_d$ and $r = R_E + h$. The refractivities for dry and wet components are given by the following expressions:

$$N_h^{Trop}(r) = N_{ds}^{Trop} \left[\frac{r_d - r}{r_d - R_E} \right]^4$$ (3.22)

and

$$N_w^{Trop}(r) = N_{ws}^{Trop} \left[\frac{r_w - r}{r_w - R_E} \right]^4$$ (3.23)

where N_{ds}^{Trop} and N_{ws}^{Trop} are models for the dry and wet refractivity at the surface of the Earth and are given by the following expressions:

$$N_{ds}^{Trop} = c_1 \frac{e}{T}$$ (3.24)

$$N_{ws}^{Trop} = c_2 \frac{e}{T} + c_3 \frac{e}{T^2}$$ (3.25)

where e is the partial pressure of water vapor (mb) and T is the temperature in degrees Kelvin. The terms c_1, c_2 and c_3 are the coefficients and are determined empirically.

The resulting Modified Hopfield model can be found in Remondi (1984) and can be expressed in the following form:

$$d_i^{Trop}(\varepsilon)=10^{-6}N_{i,0}^{Trop}\left[\sum_{k=1}^{9}\frac{\alpha_{k,i}}{k}r_i^k\right] \tag{3.26}$$

where

i   is introduced to represent the hydrostatic component and the wet component,

ε is elevation angle,

k   is the tropospheric layer, and

$N_{i,0}^{Trop}$ is the refractivity at the surface of the Earth.

The other parameters are defined as:

$$r_i = \sqrt{(R_E + h_i)^2 - (R_E \cos\varepsilon)^2} - R_E \sin\varepsilon$$

$$\alpha_{1,i}=1 \qquad\qquad\qquad \alpha_{2,i}=4a_i$$

$$\alpha_{3,i}=6a_i^2+4b_i \qquad\qquad \alpha_{4,i}=4a_i\left(a_i^2+3b_i\right)$$

$$\alpha_{5,i}=a_i^4+12a_i^2b_i+6b_i^2 \qquad \alpha_{6,i}=4a_ib_i\left(a_i^2+3b_i\right)$$

$$\alpha_{7,i}=b_i^2\left(6a_i^2+4b_i\right) \qquad\quad \alpha_{8,i}=4a_ib_i^3$$

$$\alpha_{9,i}=b_i^4$$

where $a_i=-\dfrac{\sin\varepsilon}{h_i}$; $b_i=-\dfrac{\cos^2\varepsilon}{2h_iR_E}$;

Kaniuth (1986) investigated that $h_d = 41.6$ km and $h_w = 11.5$ km for the region of observation site.

3.3.2 Wet Delay Models

3.3.2.1 Saastamoinen Model

In the zenith wet delay model, Saastamoinen (1973) assumed that there is a linear decrease of temperature with height, and that the water vapor pressure decreases with height. The variation of the water vapor pressure e is expressed by the following expression:

$$e = e_s \left[\frac{T}{T_s} \right]^{\frac{vg}{R_d \alpha}} \tag{3.27}$$

where

e_s is the water vapor pressure at the surface of the Earth,

v   is the numerical coefficient to be determined from local observations,

R_d is the specific dry gas constant,

T_s is the temperature at the surface of the Earth,

T   is the temperature in degrees Kelvin,

α   is the lapse rate, and

g   is the acceleration due to gravity.

Saastamoinen (1973) gave the expression for the zenith wet delay model using the refractivity constant of Essen and Froome (1951) and for mid-latitudes and average conditions:

$$d_w^z = 0.002277 \left(\frac{1255}{T_s} + 0.05 \right) e_s \tag{3.28}$$

3.3.2.2 Hopfield Model

Hopfield (1969) gave the expression for the zenith wet delay model using a quartic atmospheric profile:

$$d_w^z = 10^{-6} N_{ws} \frac{H_w^e}{5} \tag{3.29}$$

where N_{ws} is the wet refractivity at the surface, developed by Smith and Weintraub (1953):

$$N_{ws} = 3.73 + 10^5 \frac{e_s}{T_s^2} \tag{3.30}$$

3.3.2.3 Ifadis model

Ifadis (1986) developed the empirical model for the zenith wet delay based on the fact that there is a linear correlation between the zenith wet delay and the surface meteorological parameters. The zenith wet delay model is given by the following expression:

$$d_w^z = 0.00554 - 0.880 \times 10^{-4} \left(P_s - 1000.0 \right) + 0.272 \times 10^{-4} e_s + 2.771 \left[\frac{e_s}{T_s} \right] \tag{3.31}$$

3.3.2.4 Berman Model

The Berman model (1976) is based on the existence of a strong correlation between the ratios of the wet and zenith hydrostatic delays and the corresponding refractivities:

$$\frac{d_w^z}{d_d^z} = K \times \left[\frac{N_w}{N_d} \right]$$ (3.32)

where K is a constant and is determined with empirical values. The zenith wet delay model can be expressed by the following expression:

$$d_w^z = 10.946 \left[\frac{e_s}{T_s} \right]$$ (3.33)

3.4 MAPPING FUNCTIONS

The mapping function, $m(\varepsilon)$, is defined as the ratio of the electrical path length (also referred to as the delay) through the atmosphere at geometric elevation ε, to the electrical path length in the zenith direction. A mapping function is used to map the zenith delay to estimate the slant tropospheric delay. Several mapping functions have been developed in the past 20 years. The simplest mapping function is given by $1/\sin(\varepsilon)$ (Niell, 2000), the cosecant of the elevation angle. In this derivation, it is assumed that spherical constant-height surfaces could be approximated as planar surfaces. This is an accurate approximation only for high elevation angles and with a small degree of bending. More complex mapping functions have been developed, and different mapping functions may be used for the hydrostatic versus wet delays. Brief descriptions of the main features of various mapping functions are given in the following sub-sections.

3.4.1 Hopfield

The Hopfield mapping function (1969) is based on quartic refractivity profiles. The mapping function assumes that the neutral atmosphere has a constant lapse rate of 6.8 K km^{-1}; the neutral atmosphere is considered to be in hydrostatic equilibrium and to have an azimuthal symmetry; the ray bending is ignored. The expression for the hydrostatic or wet mapping function can be written as follows:

$$m_i(\varepsilon) = \left[\frac{5}{H_i^e} \int_{-h_{tro_i}}^{0} \frac{\left(r_{tro_i} + x\right) x^4}{\left(r_{tro_i} + x\right)^2 - \left(r_s \cos\varepsilon\right)^2} dx \right] \qquad (3.34)$$

where $h_{trop_i} = H_i^e - H_s$; $x = H - H_i^e$,

i   is the subscript for hydrostatic or wet components,

r_{tro_i} is the geocentric radius of the point at which N_i becomes negligible,

r_s is the geocentric radius of the station,

H   is the height above sea level, and

H_i^e are the equivalent heights.

3.4.2 Black

Black (1978) mapping functions are based on the quartic profiles developed by Hopfield (1969) and use the equivalent heights proposed by Hopfield (1971). The mapping functions were recommended for elevation angles above 5°. The mapping functions are as follows:

$$m_i(\varepsilon) = \left[1 - \left[\frac{\cos\varepsilon}{1+(1-l_c)\left[\frac{H_i^e}{r_s}\right]} \right]^2 \right]^{-\frac{1}{2}} \tag{3.35}$$

where $l_c = 0.85$ and is a weak function of surface temperature and elevation angle, and i is the subscript for hydrostatic or wet components.

3.4.3 Chao

Marini (1972) gave the elevation angle dependence of the atmospheric delay in the form a continued fraction, in terms of the sine of elevation angle ε:

$$m(\varepsilon) = \cfrac{1}{\sin\varepsilon + \cfrac{a}{\sin\varepsilon + \cfrac{b}{\sin\varepsilon + \cfrac{c}{\sin\varepsilon + \cdots}}}} \tag{3.36}$$

where the coefficients a, b, c... are constants or linear functions which depend on surface pressure, temperature, lapse rates, and height.

In the Chao (1972) mapping functions, the continued fraction is truncated to second order terms and the second order $\sin\varepsilon$ is replaced by $\tan\varepsilon$, and the coefficients a and b are determined from empirical data. The hydrostatic and wet mapping functions are expressed as follows:

$$m_h\left(\varepsilon\right)=\frac{1}{\sin\varepsilon+\dfrac{0.00143}{\tan\varepsilon+0.0445}} \qquad (3.37)$$

$$m_w=\frac{1}{\sin\varepsilon+\dfrac{0.00035}{\tan\varepsilon+0.017}} \qquad (3.38)$$

3.4.4 Baby et al.

Baby et al. (1988) used Snell's law of refraction to expand the term $1/\sin\theta$ and gave the following expression for the mapping function for hydrostatic and wet components:

$$m_t\left(\theta\right)=\frac{1}{\sin\theta\sqrt{\left(1+\varepsilon_H\cot^2\theta\right)}} \qquad (3.39)$$

where θ is the refracted elevation angle from zenith, and ε_H is a term depending on the refractive index and geocentric distance of the station.

3.4.5 Herring

Herring (1992) has developed both hydrostatic and wet mapping functions by fitting to radiosonde data from several North American stations ranging in geographic latitude from $27°\,\mathrm{N}$ to $65°\,\mathrm{N}$ for elevation angles down to $3°$. The mapping function's coefficients depend linearly on surface temperature, the cosine of the station latitude, and the height of the station above the geoid. The expression for the mapping function is given below:

$$m(\varepsilon)=\cfrac{\left[\cfrac{1}{1+\cfrac{a}{1+\cfrac{b}{1+c}}}\right]}{\sin(\varepsilon)+\cfrac{a}{\sin(\varepsilon)+\cfrac{b}{\sin(\varepsilon)+c}}} \qquad (3.40)$$

where a, b, and c are constants or linear functions.

3.4.6 Neill

The Neill (1996) mapping functions have no parameterization in terms of meteorological conditions, and they provide a better fit and give better accuracy over the latitude range $43°\,N$ to $75°\,N$ for elevation angles down to $3°$. The form adopted for the mapping functions is the continued fraction with three coefficients (a, b, c) as given in equation (3.36). The coefficients of the continued fraction representation of the hydrostatic mapping function depend on the latitude and height above sea level of the observing site (H) and on the day of the year. The wet mapping function depends only on the site latitude. The expressions for the hydrostatic and wet mapping functions are given below:

$$m_{hydro}(\varepsilon)=\cfrac{1}{\sinε+\cfrac{a_{hydro}}{\sinε+\cfrac{b_{hydro}}{\sinε+c_{hydro}}}}{\sinε+\cfrac{a_{hydro}}{\sinε+\cfrac{b_{hydro}}{\sinε+c_{hydro}}}}+\left[\cfrac{1}{\sinε}-\cfrac{1+\cfrac{a_{ht}}{1+\cfrac{b_{ht}}{1+c_{ht}}}}{\sinε+\cfrac{a_{ht}}{\sinε+\cfrac{b_{ht}}{\sinε+c_{ht}}}}\right]\times\cfrac{H}{1000} \qquad (3.41)$$

$$m_{wet}(\varepsilon)=\cfrac{\cfrac{1}{1+\cfrac{a_{wet}}{1+\cfrac{b_{wet}}{1+c_{wet}}}}}{\sinε+\cfrac{a_{wet}}{\sinε+\cfrac{b_{wet}}{\sinε+c_{wet}}}} \qquad (3.42)$$

where

ε is the elevation angle, and $a_{ht}=2.53\times10^{-5}$ km, $b_{ht}=5.49\times10^{-3}$ km, $c_{ht}=1.14\times10^{-3}$ km .

For the hydrostatic mapping function the parameter 'a' at tabular latitude φ_i at time t from January 0.0 (in UT days) is interpolated using the Table 3.2 and the following expression:

$$a(\varphi_i,t)=a_{avg}(\varphi_i)+a_{amp}(\varphi_i)\cos\left[2\pi\frac{t-T_0}{365.25}\right] \qquad (3.43)$$

where T_0 is the adopted phase, Day-of-year (DOY) 28 (detail in Niell, 1996), and t is day of the year; the value $a(\varphi,t)$ for a given value of φ is obtained by interpolating linearly between values of $a(\varphi_i,t)$ for the appropriate values of φ_i in Table 3.2. A similar procedure is followed for the parameters b and c. The average values of $a_{hydro,}$ b_{hydro}, c_{hydro}

and their amplitudes are given in Table 3.2. For the wet mapping function, only an interpolation in latitude for each parameter is needed (Neill, 1996). The average values of $a_{wet,}$ b_{wet}, c_{wet} and their amplitudes are given in Table 3.3.

Table 3.2 Coefficients of the Hydrostatic Mapping Function

Coefficient	Latitude (degree)				
(hydro)	15	30	45	60	75
	Average				
a_{avg}	1.2769934e-3	1.2683230e-3	1.2465397e-3	1.2196049e-3	1.2045996e-3
b_{avg}	2.9153695e-3	2.9152299e-3	2.9288445e-3	2.9022565e-3	2.9024912e-3
c_{avg}	62.610505e-3	62.837393e-3	63.721774e-3	63.824265e-3	64.258455e-3
	Amplitude				
a_{amp}	0.0	1.27079626e-5	2.6523662e-5	3.4000452e-5	4.1202191e-5
b_{amp}	0.0	2.1414979e-5	3.0160779e-5	7.2562722e-5	11.723375e-5
c_{amp}	0.0	9.0128400e-5	4.3497037e-5	84.795348e-5	170.37206e-5

Table 3.3 Coefficients of the Wet Mapping Function

Coefficient	Latitude (degree)				
(wet)	15	30	45	60	75
	Average				
a_{avg}	5.8021897e-4	5.6794847e-4	5.8118019e-4	5.9727542e-4	6.1641693e-4
b_{avg}	1.4275268e-3	1.5138625e-3	1.457252e-3	1.5007428e-3	1.7599082e-3
c_{avg}	4.3472961e-2	4.6729510e-2	4.3908931e-2	4.4526982e-2	5.4736038e-2

CHAPTER 4

TROPOSPHERIC DELAY ESTIMATION

The first two objectives of this thesis research are to determine zenith wet delays and slant wet delays from the GPS observations and to validate them with the truth values. These objectives are fulfilled using GPS data, water vapor radiometer (WVR) data, and meteorological (Met) data. The GPS data were collected with a NovAtel OEM4 receiver, the WVR data were collected with a WVR1100 water vapor radiometer, and Met data were collected with a MET3A meteorological package. The three instruments were run simultaneously very near to each other on the roof of the Engineering Building at the University of Calgary. The GPS data from the reference stations PRDS, NANO, and DRAO were downloaded from the Scripps Orbit and Permanent Array Center (SOPAC) web site. The WVR data are taken as "truth" to validate the zenith wet delays and slant wet delays derived from the GPS data.

In this chapter, the methodology will be given to determine the zenith wet delays and slant wet delays from the GPS data. A brief description of data sets will also be presented. The validation of wet delays obtained from GPS data will be demonstrated using the truth data from the WVR. Finally, an accuracy analysis of the observed differences between GPS and WVR wet delays will be shown.

4.1 METHODOLOGY

The methodologies given here describe a processing technique to derive slant wet delays from GPS data. The slant wet delays are the fundamental observables in the tomographic 4-D modeling (Chapter 5). Figure 4.1 gives the general overview of the methodologies. Data collection and data sets are described in Section 4.2. Once the data from the GPS receiver, WVR, and Met Pack have been collected, the GPS data are post-processed to estimate the

zenith tropospheric delays and gradient parameters. The gradients are then applied and the zenith tropospheric delays are converted into slant wet delays dependent on satellite azimuth and elevation angle. Accuracies are tested using truth data from the WVR. The wet refractivity within a small network in the Southern California Integrated GPS Network (SCIGN) is estimated using tomography techniques in Chapter 5. The methodology given in Figure 4.1 is described in detail in the following sub-sections.
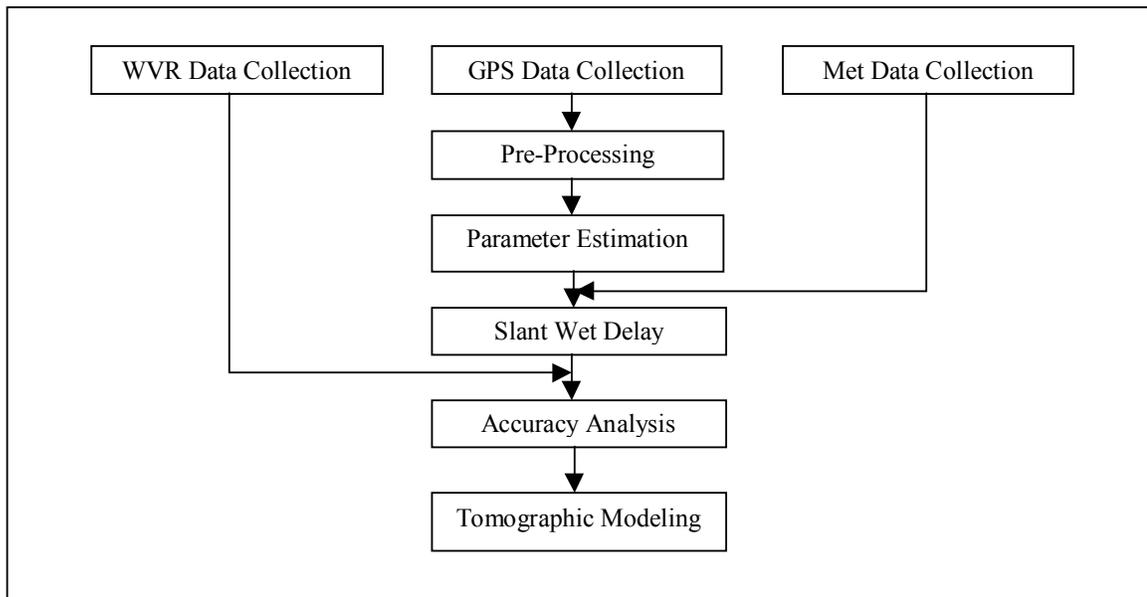
Figure 4.1 Methodology.

4.1.1 Pre-Processing

Initially, the GPS data needs to be pre-processed prior to estimating the total zenith tropospheric delays. The positions of satellites and the ground positions must be known precisely in order to determine the total zenith delays. The total zenith delays consist of both the hydrostatic and wet components of the tropospheric delays. Because of high correlation between the wet and hydrostatic elevation dependence in the model used for processing, only the total zenith delays (sum of the wet and the hydrostatic zenith delays) and total gradient delays (sum of hydrostatic and the wet zenith delay gradients) can be

estimated with the present GPS data processing (Gradinarsky and Jarlemark, 2002). The data pre-processing is done using Bernese software version 4.2 (Hugentobler et al., 2001). The pre-processing programs used in this thesis are TRANSFER, CODSPP, SNGDIF, MAUPRP, and GPSEST. The pre-processing steps are shown in Figure 4.2 and are described below briefly.
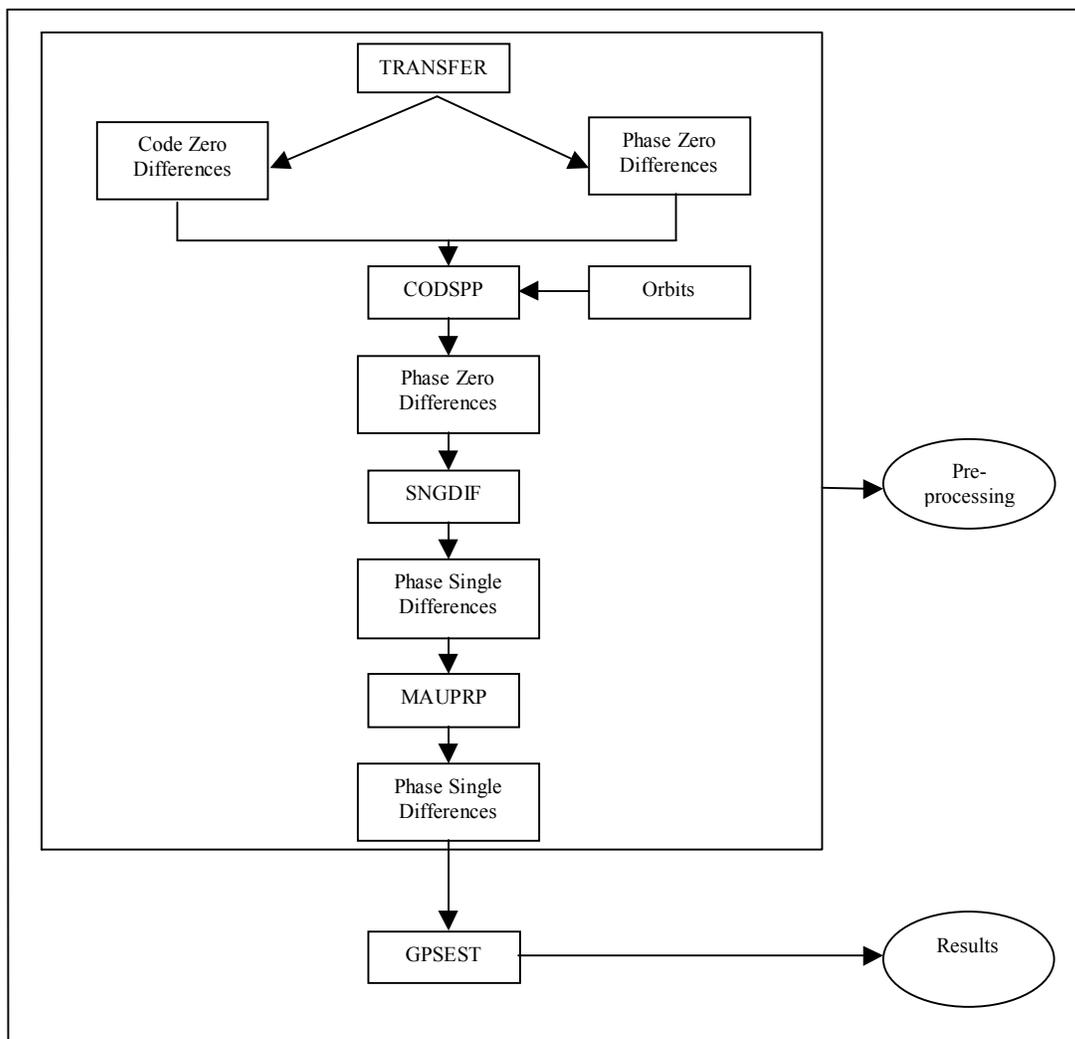
Figure 4.2 Data processing.

4.1.1.1 TRANSFER

All the GPS processing programs need the explicit format of the GPS observables in order to process them. If the data are collected in different receivers, the raw receiver information must first be converted to standard definitions and formats. The GPS data being used in this thesis are obtained from different types of GPS receivers. A NovAtel OEM4 receiver is used to collect GPS data on the roof of the Engineering Building at the University of Calgary. AOA BENCHMARK ACT receivers are used in the stations DRAO and NANO, and an AOAD/M_T receiver is used in the station PRDS. The TRANSFER program facilitates the conversion of any raw receiver data into a RINEX format (Gurtner et al., 1989) and gives an explicit definition of the observables.

The basic information to be used in the RINEX format are the epochs of observations, carrier phase observations, and pseudorange observations. These three quantities are based on the same oscillator, such that any offsets and drifts of the oscillator are included in the basic observables. There are three types of RINEX files: RINEX observation files, RINEX navigation message files, and RINEX meteorological data files. Only the RINEX observation files are used in this thesis.

A RINEX observation file contains data collected by one receiver only. A file contains data from one station and one session only. The file consists of a header, containing all auxiliary information on the station and the receiver necessary for post-processing of the data, and a data section containing the basic observables. The basic observables are code zero differences and phase zero differences. The RINEX observation files are transferred into Bernese format for all the GPS observables that are to be used with all programs in the Bernese software version 4.2 (Hugentobler et al., 2001).

4.1.1.2 CODSPP

The receiver clock has to be synchronized with GPS time. The receiver clock error δ_k has to be known with an accuracy better than 1 μs. The CODSPP program computes the receiver clock error δ_k using the zero-difference code measurements, and also gives *a posterori* RMS error on the position estimation. These outputs help to check if measurements are good enough for further processing. This program stores the clock offsets in the phase observation files for further processing.

This program uses an ionospheric-free linear combination in a standard least-squares adjustment to compute unknown parameters, such as the receiver clock corrections, and coordinates of receivers. The equation for the ionospheric-free linear combination L_3 can be written as follows:

$$L_3 = \frac{1}{f_1^2 - f_2^2}\left(f_1^2 L_1 - f_2^2 L_2\right) \tag{4.1}$$

where
f_1, f_2 are the frequencies of GPS signals, and
L_1, L_2 are the carrier phase measurements of GPS signals.

4.1.1.3 SNGDIF

The SNGDIF program creates the code single-differences and phase single-differences and stores these observations in files. Only the phase single-differences between receivers are used for the computation of the double differences of GPS measurements, which are the basic observables for determination of tropospheric parameters and gradient parameters.

If there are N receivers being used for the measurements simultaneously, there will be N zero-difference measurements to each satellite at each epoch for each carrier. There will be N-1 independent single differences. This program creates one set of N-1 baselines for the entire session and stores the observations into the single-difference files. However, there are two criteria for the selection of independent baselines: maximum or minimum baseline length; and the number of available baselines.

4.1.1.4 MAUPRP

The receivers measure the difference between the phase of the satellite-transmitted carrier and the phase of the receiver generated replica of the signal. This measurement yields a value between 0 and 1 cycle (0 and 2π). The initial integer is initialized once the receiver begins tracking the signal for a given satellite. The accumulated phase is the sum of the directly measured fractional phase and the integer count. The unknown phase count is called a phase ambiguity. The initial phase ambiguity remains constant provided that no loss of signal lock occurs. A loss of lock causes a jump in the instantaneous accumulated phase by an integer number of cycles and is called a cycle slip. Cycle slips might occur due to the obstruction of the satellite signals from trees, buildings, etc. and due to low signal-to-noise ratio.

The MAUPRP program checks the observations and finds the time intervals during which observations are corrupted by cycle slips. Also, it repairs the cycle slips if it is possible. The MAUPRP program performs the following steps:

- Automatic cycle slip detection: The programs correct large discontinuities on the single difference level. Such jumps arise from the receiver clock and are common to all satellites.

- Checking by smoothing: The CODCHK algorithm finds time intervals in which no cycle slips occur with certainty.

- Triple-difference solution: The triple-difference solution is performed using the standard least-squares adjustment for each baseline. The advantage of triple-difference solution over double-difference solution is that an undetected cycle slip corrupts one triple-difference only, as opposed to all double-differences after the cycle slip.

4.1.1.5 GPSEST

The program GPSEST is used for the estimation of tropospheric parameters and gradient parameters. It generates these parameters using the double difference solution and standard least-squares adjustment for each station. The program performs the following tasks:

- Firstly, the program estimates the accurate coordinates of stations from the ionospheric-free linear combination without resolving the ambiguities. The basic observables are double difference carrier phase observations. This process does not generate final results, but it checks the quality of data and estimates coordinates of stations.

- The ambiguities are resolved for all baselines separately using tropospheric corrections and ionospheric corrections. Different strategies can be selected for the ambiguity resolution, such as round, sigma, search, quasi-ionospheric free and lamda methods (details in Hugentobler et al., 2001).

- Lastly, the program generates the final coordinates of the stations and tropospheric parameters for each station. It also generates the tropospheric gradient parameters for each station. The program uses double difference carrier phase observations and the ionospheric-free linear combination. The ambiguities on L1 and L2 resolved together in previous processing steps are used in the least squares adjustment.

4.1.2 Tropospheric Parameter Estimation

The tropospheric delays are one of the accuracy-limiting factors for applications of the GPS. There are two kinds of tropospheric biases: relative troposphere biases, and absolute troposphere biases (Beutler et al., 1988).

4.1.2.1 Relative Troposphere Biases

Relative troposphere biases are caused by errors of (mismodeled) troposphere refraction at one of the endpoints of a baseline relative to the other endpoint. Relative troposphere biases are important for local and smaller regional campaigns. Biased station heights are caused due to the effect of relative troposphere error and can be computed as:

$$\Delta h = \frac{\Delta\rho_r^0}{\cos z_{max}}$$

(4.2)

where

Δh is the induced station height bias,

$\Delta\rho_r^0$ is the relative tropospheric zenith delay error, and

$\cos z_{max}$ is the maximum zenith angle of the observation scenario.

4.1.2.2 Absolute Tropospheric Biases

Absolute troposphere biases are caused by errors of (mismodeled) tropospheric refraction common to both endpoints of a baseline. Absolute troposphere biases are important for global and regional campaigns. Scale biases of the estimated baseline lengths are caused due to absolute troposphere errors and are computed as:

$$\frac{\Delta l}{l} = \frac{\Delta \rho_a^0}{R_E \cos z_{max}}$$
(4.3)

where

$l, \Delta l$ are the baseline length and the associated bias,

$\Delta \rho_a^0$ are the absolute troposphere bias in zenith direction, and

R_E is the Earth's radius.

4.1.2.3 Troposphere Parameters for Individual Stations

The estimation of troposphere parameters for individual stations is much more common than the estimation of local troposphere models (Hungentobler et al., 2001). The total tropospheric delay corrections $d_{trop, k}$ for the individual station is given by:

$$d_{trop, k} = m_{apr}\left(z_k^i\right) d_{trop(apr), k}^z + m\left(z_k^i\right) d_{trop, k}^z(t)$$
(4.4)

where

$d_{trop(apr), k}^z$ is the tropospheric zenith delay according to the *a priori* model specified,

z_k^i is the zenith distance for a satellite i, and station k,

m_{apr} is the mapping function of the *a priori* model,

$d_{trop, k}^z(t)$ is the time-dependant zenith troposphere parameter for station k, and

$m\left(z_k^i\right)$ is the mapping function used for the parameter estimation.

In the Bernese software version 4.2, a set of parameters $d_{trop, k}^z$ is estimated for each site, and each parameter is valid within a time interval (t_i, t_{i+1}).

4.1.2.4 Troposphere Gradient Parameters Estimation

Troposphere gradient parameters are estimated to take into account azimuthal asymmetries in the tropospheric delay (Hugentobler et al., 2001). Having introduced the troposphere gradient parameter, the tropospheric delay would be given by:

$$
\begin{aligned}
d_{\text{trop, k}}(t) = {}& m_{\text{apr}}\left(z_k^i\right) d_{\text{trop(apr), k}}^z + m\left(z_k^i\right) d_{\text{trop, k}}^z(t) \\
& + G_N(t)\frac{\partial m}{\partial z}\cos\left(A_k^i\right) + G_E(t)\frac{\partial m}{\partial z}\sin\left(A_k^i\right)
\end{aligned}
\tag{4.5}
$$

where

$d_{\text{trop(apr), k}}^z$ is the tropospheric zenith delay according to the *a priori* model specified,

$d_{\text{trop, k}}^z(t)$ is the zenith delay parameter,

$G_N(t)$ is the gradient parameter in north-south direction,

$G_E(t)$ is the gradient parameter in east-west direction, and

A_k^i is the azimuth of the station-satellite direction.

4.1.3 Slant Wet Delay computation

The tropospheric delays are also called total zenith delays since delays are calculated in the zenith direction.. The slant delay d_{trop}^s is the delay mapped into line-of-sight between the individual satellite and receiver, and is associated with zenith hydrostatic delay $\left(d_h^z\right)$ and zenith wet delay $\left(d_w^z\right)$ through the hydrostatic and wet mapping functions $m_h(\varepsilon)$ and $m_w(\varepsilon)$, respectively. The slant delay can be calculated using the equation 3.11.

The zenith hydrostatic delay can be estimated with accuracies better than 1% using any of hydrostatic models explained in Section 3.3.1. In this thesis, the zenith hydrostatic delay is estimated using the Saastamoinen model where the delay is derived from precise measurements of surface atmospheric pressure using the equation 3.13.

Equation 3.11 assumes that the atmosphere is azimuthally homogenous, meaning that water vapor is equally distributed in all directions in the atmosphere. In precise GPS applications, the azimuthal asymmetry should be considered to derive the slant delays. The slant delays can be modeled as the contribution of a zenith component plus horizontal gradients (Davis et al., 1993):

$$
\begin{aligned}
d_{trop}^{s} = & \, m_h \left(\varepsilon \right) \left[d_h^z + \cot\varepsilon \left(G_N^h \cos A + G_E^h \sin A \right) \right] \\
& + m_w \left(\varepsilon \right) \left[d_w^z + \cot\varepsilon \left(G_N^w \cos A + G_E^w \sin A \right) \right]
\end{aligned}
\tag{4.6}
$$

where

ε $\quad\quad\quad$ is the elevation angle between the satellite and station,

A $\quad\quad\quad$ is the azimuth of the satellite,

G_N^h, G_E^h $\quad\quad$ are the north and east components of the hydrostatic delay gradients, and

G_N^w, G_E^w $\quad\quad$ are the north and east components of the wet delay gradients.

Once all hydrostatic parameters are removed from the equation 4.6, the slant wet delays of GPS signal d_w^s can be calculated using the following expressions:

$$
d_w^s = m_w \left(\varepsilon \right) \left[d_w^z + \cot\varepsilon \left(G_N^w \cos A + G_E^w \sin A \right) \right]
\tag{4.7}
$$

Equation 4.7 is used to derive basic slant wet delay observables for the tomographic model. The wet mapping function used in this thesis is the wet Niell mapping function (Niell, 1996). In this thesis, the assumption is made that hydrostatic gradients are not removed from the total gradients in order to recover the wet gradients. Experiments have shown that

surface horizontal gradients of the wet and hydrostatic refractivity fields are on the order of $0.5 \, \text{Nkm}^{-1}$ and $0.005 \, \text{Nkm}^{-1}$, respectively (Flores et al., 2000b). There are two orders of magnitude difference between both kinds of gradients and, therefore, the hydrostatic gradient is considered to be negligible with respect to the wet gradient, such that the total gradient estimated using Bernese software version 4.2 is approximately equal to the wet gradient.

4.1.4 Accuracy Analysis

The accuracy of zenith wet delays and slant wet delays are evaluated in terms of root mean square (RMS) error, which can be calculated using the following expression:

$$RMS = \sqrt{\sum_{i=1}^{n} \frac{\left(X_i - X_{true}\right)^2}{n}} \tag{4.8}$$

where

X_i the observed value,

X_{true} the truth value, and

n   the number of observations.

In the results presented in this chapter, observations derived from a water vapour radiometer are used as truth values.

4.2 DATA SETS

Three sets of data have been used to estimate the tropospheric parameters and determine the slant wet delays from GPS measurements. The data sets are described briefly below.

4.2.1 GPS Data

GPS data was collected continuously from the beginning of May-June 2002 using a NovAtel OEM 4 receiver and a NovAtel GPS-600 antenna. The antenna was fixed on a pillar on the roof of the Engineering Building at the University of Calgary. The cutoff elevation angle was set to $15°$. The raw code and phase data were collected on both the L1 and L2 frequencies, and measurements were taken every 30 seconds. The raw data has been compiled in files consisting of 24 hours of observations, and each file was transferred into RINEX format for further processing to estimate tropospheric parameters using NovAtel Convert™ software. AOA BENCHMARK ACT receivers are used at the stations DRAO and NANO, and an AOAD/M_T receiver is used at the station PRDS. The GPS data are available at 30 seconds intervals and are in RINEX format. Figure 4.3 shows the geographical locations of the stations.
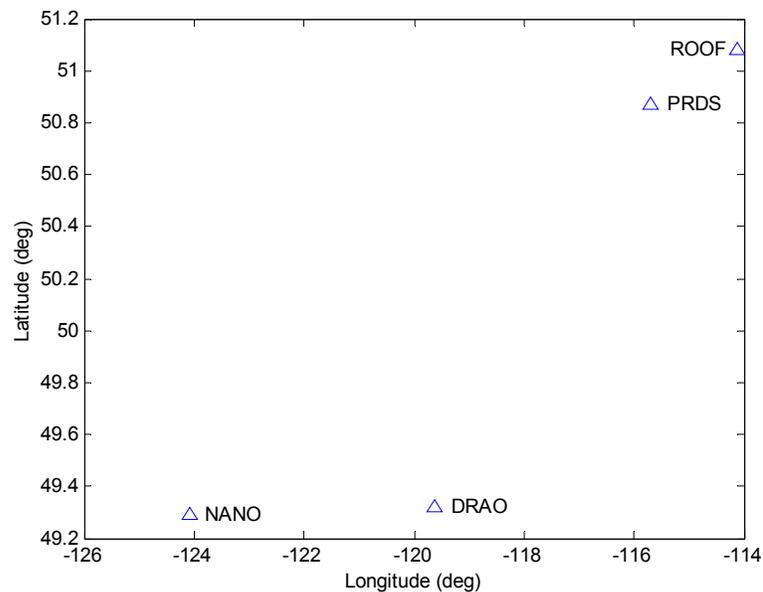
Figure 4.3 Geographical locations of stations.

Table 4.1 gives coordinates and heights of stations that are used for the processing to estimate tropospheric parameters and Table 4.2 shows the corresponding baseline lengths.

Table 4.1 Coordinates and Heights of Stations

STATION NAME	LATITUDE (deg min sec)	LONGITUDE (deg min sec)	HEIGHT (m)
ROOF	51 04 45.94	-114 07 58.13	1116.61
PRDS	50 52 16.68	-115 42 19.80	1249.11
DRAO	49 19 21.431	-119 37 29.931	542.38
NANO	49 17 41.320	-124 05 11.33	7.32

Table 4.2 Baseline Lengths

BASELINE	BASELINE LENGTH (km)
PRDS-ROOF	25
DRAO-ROOF	437
NANO-ROOF	737

The quality of data was tested during the processing of the data with the algorithms MAUPRP and GPSEST in terms of the presence of cycle slips. If the number of cycle slips were found to be relatively low, then the data were further processed for the estimation of trophospheric parameters. Table 4.3 gives examples of the data quality assessment, which presents the number of cycle slips for the processing of double difference observations between NANO, DRAO and PRDS with respect to the receiver on the roof of the Engineering Building at University of Calgary for May 25, 2002 (Day 145).

Table 4.3 Data Quality Assessment

BASELINE	DOUBLE DIFFERENCE OBSERVATIONS	NUMBER OF CYCLE SLIPS
PRDS-ROOF	17033	23
DRAO-ROOF	16643	38
NANO-ROOF	16080	6

4.2.2 Ground Meteorological Data

The meteorological package MET3A (manufactured by ParoScientific, Inc.) has been used to collect surface pressure, temperature and humidity measurements. This instrument was fixed very near to the GPS station on the roof of the Engineering Building at the University of Calgary. The surface pressure, temperature and humidity data were collected at 15-minute intervals. Figure 4.4 shows the meteorological package, MET3A.

Figure 4.4 MET3A.

The surface pressure measurements were used to model the zenith hydrostatic delays and remove them from zenith troposphere estimates derived from GPS measurements. An error of only 1 mb in the surface pressure measurement will induce a bias of 2 mm in the total zenith delay (Hugentobler et al., 2001). Therefore, the sensitivity of the meteorological

package should be a tenth of a millibar for the measurement of surface pressure. In this thesis, the sensitivity of the MET3A was limited to millibar precision in significant digits due to limitations in the manufacturer's software.

4.2.3 Water Vapor Radiometer Data

A WVR manufactured by Radiometrics, Inc. was installed very near to the GPS station on the roof of the Engineering Building. The water vapor radiometer scans every satellite in view, and records the precipitable water vapor and integrated liquid water above the instrument. The WVR also generates the radio propagation delay along a specified path due to the troposphere, such as zenith wet days and slant wet delays. In fact, the water vapor radiometer measures radiative brightness temperatures, which are converted into the precipitable water vapor and radio path delay using retrieval coefficients. Figure 4.5 shows the water vapor radiometer.

Figure 4.5 Water Vapor Radiometer (WVR).

The WVR is used as a tool to validate the GPS derived parameter to be used in GPS meteorology, namely zenith wet delays and slant wet delays. The WVR estimates those parameters with a high level of precision. The azimuth drive of the WVR allows it to point to all GPS satellites in view. The WVR measures slant wet delays directly along the satellite-receiver path for each satellite in view. It takes 50 seconds to measure each slant wet delay, such that a full cycle for all satellites in view is completed every 6-7 minutes. It also gives zenith wet delays using a mapping function. The other outputs of the WVR are the zenith liquid delays, integrated liquid content and brightness temperatures. For processing purposes, the zenith wet delays and slant wet delays were produced every 30 seconds with a linear interpolation technique, and these 30-second values were used to validate the zenith wet delays and slant wet delays derived from GPS measurements. The validation results are shown in Section 4.4.

4.2.3.1 Theory of Operation of WVR

The WVR is a dual-frequency total power radiometer, operating at 23.8 GHz and at 31.4 GHz. These two frequencies allow simultaneous determination of integrated liquid water and integrated water vapor along a selected path. The atmospheric brightness temperature is related to the Earth-atmospheric physical temperature and absorption through a radiative transfer equation (RTE), which involves both absorption and scattering phenomena. Brightness temperature is the key parameter describing atmospheric microwave emission depending on frequency, polarization, and viewing angle. Sky brightness temperature T_B can be described by Chandrasekhar's radiative transfer equation (Chandrasekhar, 1950) for non-scattering medium (local thermodynamic equilibrium):

$$T_B(f) = T_C e^{-\tau(0,\infty)} + \int T(z)\alpha(z)e^{-\tau(0,\infty)}dz \qquad (4.9)$$

where $\alpha(z)$ is the atmospheric volume absorption coefficient at the frequency of interest, $T(z)$ is the absolute physical air temperature in Kelvin, and T_C is the blackbody temperature of space. The frequency-dependent atmospheric opacity, $\tau(0,\infty)$ can be represented by the following expression:

$$\tau(0,\infty)=\int_0^\infty \alpha(z)dz \tag{4.10}$$

It is possible to convert the radiometrically measured brightness temperature into the atmospheric opacity, τ, using the mean radiation temperature of the atmosphere. The opacity, τ, includes contributions from oxygen, water vapor, and suspended water droplets (cloud liquid), and is frequency-, temperature- and pressure-dependent.

$$\tau_f(0,\infty)=\ln\left[\frac{T_{MR}(f)-T_C}{T_{MR}(f)-T_B(f)}\right] \tag{4.11}$$

where T_{MR} is the mean radiating temperature of the atmosphere and is defined as follows:

$$T_{MR}(f)=\frac{\int_0^\infty \alpha(z)T(z)e^{-\tau(0,z)}dz}{\int_0^\infty \alpha(z)e^{-\tau(0,z)}dz} \tag{4.12}$$

The integrated water vapor, liquid water, and phase path delay can be obtained from the linear retrieval equations:

$$\text{water vapor} = c_0\left(\text{vap}\right)+c_1\left(\text{vap}\right)\tau_{23.8}+c_2\left(\text{vap}\right)\tau_{31.4}$$

$$\text{liquid water} = c_0\left(\text{liq}\right)+c_1\left(\text{liq}\right)\tau_{23.8}+c_2\left(\text{liq}\right)\tau_{31.4} \tag{4.13}$$

$$\text{radio path delay} = c_0\left(\text{ph}\right)+c_1\left(\text{ph}\right)\tau_{23.4}+c_2\left(\text{ph}\right)\tau_{31.4}$$

where the retrieval coefficients (c_0, c_1 and c_2) are site dependent, and are determined from bilinear regression of water vapor data and inferred liquid water data derived from radiosonde observations (RAOB). The mean radiation temperature T_{MR} must also be determined from RAOB history.

4.3 ERROR DISCUSSION

The precision of validating zenith wet delays and slant wet delays derived from GPS data with the WVR data depends on several different factors: orbital errors, multipath effects, phase noise, WVR errors, and pressure sensor errors. These sources of error are described as follows:

- Orbital errors: NGS (National Geodetic Survey) precise orbits have errors of 0.01 ppm or less. They contribute no more than a 0.5 mm error in the horizontal components of a 50-km baseline. The errors in the vertical component would be 1.5 mm since GPS errors are 2 or 3 times larger in the vertical than in the horizontal. GPS vertical baseline errors are typically 3 times as large as the tropospheric errors causing them (Rocken et al., 1993). Therefore, orbital errors contribute no more than 0.5 mm of the observed difference between GPS and WVR zenith wet delays.

- Multipath errors: Multipath errors are caused by reflection from objects near the GPS antenna and are harder to quantify. In our experiments, the GPS receiver was set up on the roof without any surrounding obstructions and the NovAtel GPS-600 antenna was used to reduce the error due to multipath. The NovAtel GPS-600 antenna takes into account the polarization of the signals to reduce the level of multipath (NovAtel, 2000).

An experiment showed that multipath errors may account for at least 1 cm of the observed difference between GPS and WVR zenith wet delays (Rocken et al., 1993).

- Phase noise errors: The ionosphere-free linear combination is used to estimate the tropospheric parameters. The phase noise of this combination is about 3 mm. Since a large number of observations is used to estimate tropospheric parameters, the contributions of random phase noise are filtered and have negligible impact on the estimation of zenith wet delays.

- WVR errors: Side-by-side comparisons of two water vapor radiometers showed a 2 mm zenith wet delay bias due to instrumental calibration errors (Ware et al., 1993). Additional WVR errors occur due to errors in retrieval coefficients and conversion factors, which are dependent on the site, and are derived from radiosonde (RAOB) observations. In addition, WVR data were not used during rain events because raindrops on the WVR window introduce unrealistically large wet delays. In experiments described in Section 4.4, Radiometrics, Inc. has provided the site specific retrieval coefficients, and these coefficients were used for the estimation of delay parameters. Since these coefficients were not derived from the RAOB history near the site at the University of Calgary, outputs from the WVR must contain some errors. It is noted that the calibration of the noise diode of the WVR was carried out on the roof of the Engineering Building at the University of Calgary. The calibrated noise diode is used for receiver gain calibration of brightness temperature observations. Detail of calibration process of the WVR can be found in the manual for the WVR (Radiometerics, 2002)

- Pressure sensor errors: Pressure errors of 1 mbar cause errors of 2 mm in zenith wet delay estimates. The calibration uncertainty is assumed to be 1 mbar, and the sensitivity of the MET3A is 1 mbar for pressure measurements. Pressure errors can therefore cause as much as a 3 mm error in zenith wet delay.

4.4 EXPERIMENTAL RESULTS

In this section, zenith wet delays and slant wet delays are estimated using GPS data, and are validated through comparisons with delays measured using the WVR. The WVR has been the primary tool in these evaluations due to its high level of precision and because it is considered a more established technology for the retrieval of zenith wet delays and slant wet delays (Bar-Sever, 1996). Furthermore, factors which affect the accuracy for deriving the zenith wet delays and slant wet delays are evaluated.

4.4.1 Validation of Zenith Wet Delays

The GPS data were processed from May 25, 2002 (Day 145) to June 14, 2002 (Day 165) to determine zenith wet delays using methods described in Section 4.1. Zenith wet delays were estimated in batch mode for every hour and gradient parameters were estimated in batch mode every 12 hours using a multiple reference station approach. NANO (basline 737 km) and DRAO (baseline 438 km) were used as reference stations to estimate zenith wet delays and gradient parameters for the GPS site on the roof of the Engineering Building. Figure 4.6 shows the magnitude of zenith wet delays computed using GPS and "truth" values for the WVR. The black line represents the zenith wet delays from GPS measurements and the pink line represents zenith wet delays from WVR measurements. The GPS zenith wet delays were derived at hourly intervals, as explained in Section 4.1. The WVR produces estimates of each zenith wet delay every 50 seconds, such that zenith wet delays from all satellites in view are estimated every 6-7 minutes. The zenith wet delays were averaged for all satellites in view over an hour. Figure 4.6 shows similar trends of zenith wet delays from the GPS and the WVR. However, there are a few spikes on June 2, 2002 (Day 153), June 3, 2002 (Day 154), June 9, 2002 (Day 160), and June 10, 2002 (Day 161). The WVR gave unreliable data for those days. Figure 4.7 shows a plot for the humidity data from May 25, 2002 (Day 145) to June 14, 2002 (Day 165). The humidity values were almost 100% on June 2, 2002 (Day 153), June 3, 2002 (Day 154), June 9, 2002

(Day 160), and June 10, 2002 (Day 161). There was precipitation on those days, and the water vapor radiometer gave high values for delays due to the presence of water droplets on the observation window of the WVR.
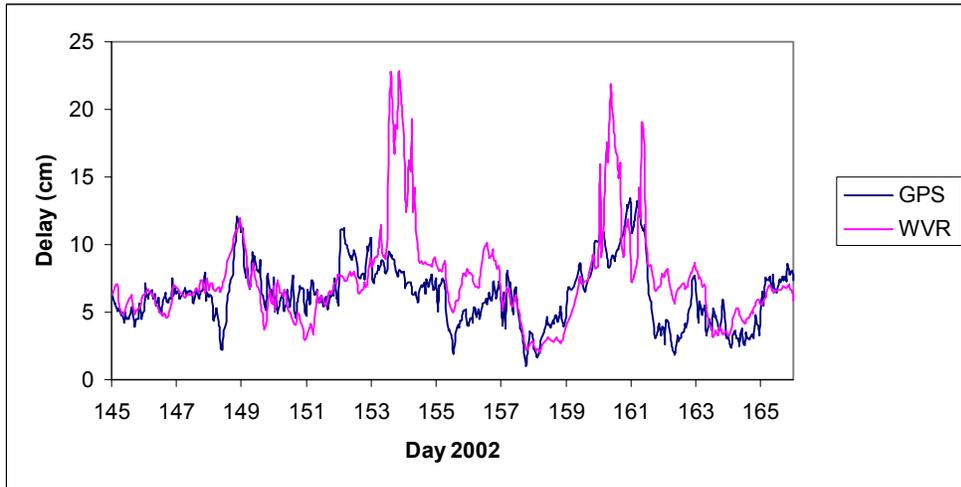
Figure 4.6 Zenith wet delays from the GPS and WVR.
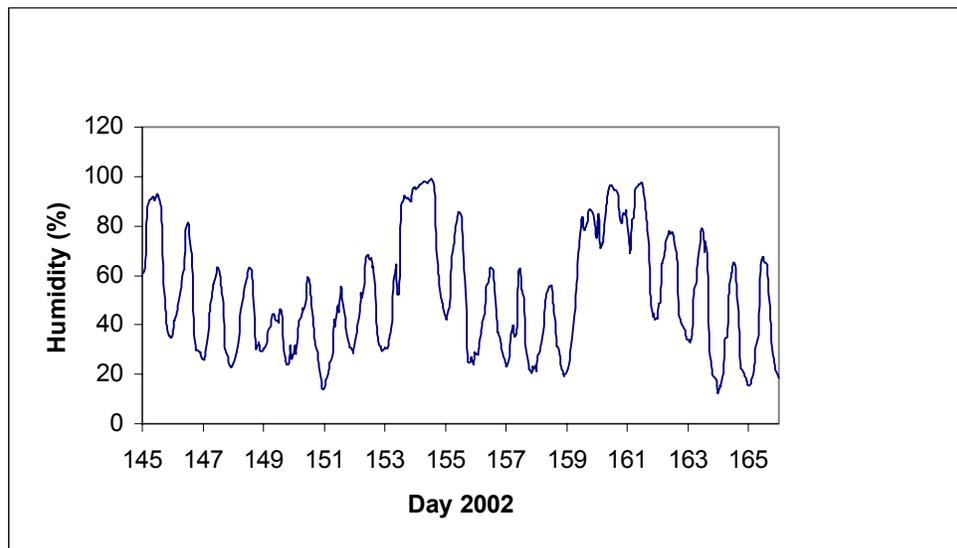
Figure 4.7 Relative humidity change.

Zenith wet delays from the WVR are not reliable when a large amount of liquid water content is retrieved (Shoji et al., 2000). The WVR observations were screened to remove data when the instrument measured more than 0.1 mm of liquid water in the atmosphere. Accuracies of zenith wet delays derived from the GPS data can be compared with zenith wet delays from the WVR data (which are taken to be truth). Figure 4.8 shows the daily RMS zenith wet delays for the GPS data. The overall RMS zenith wet delays for GPS data during May 25-June 14, 2002 are about 2-3 cm.
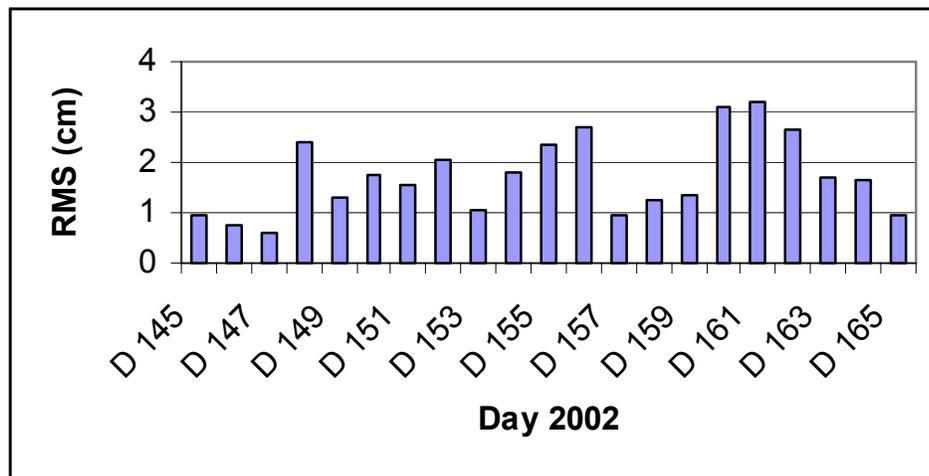
Figure 4.8 RMS zenith wet delays.

Figure 4.9 shows changes in gradient parameters from May 25, 2002 (Day 145) to June 14, 2002 (Day 165). The black line shows north-south gradient parameters and the pink line shows east-west parameters. Gradient parameters were estimated in 12-hour intervals.
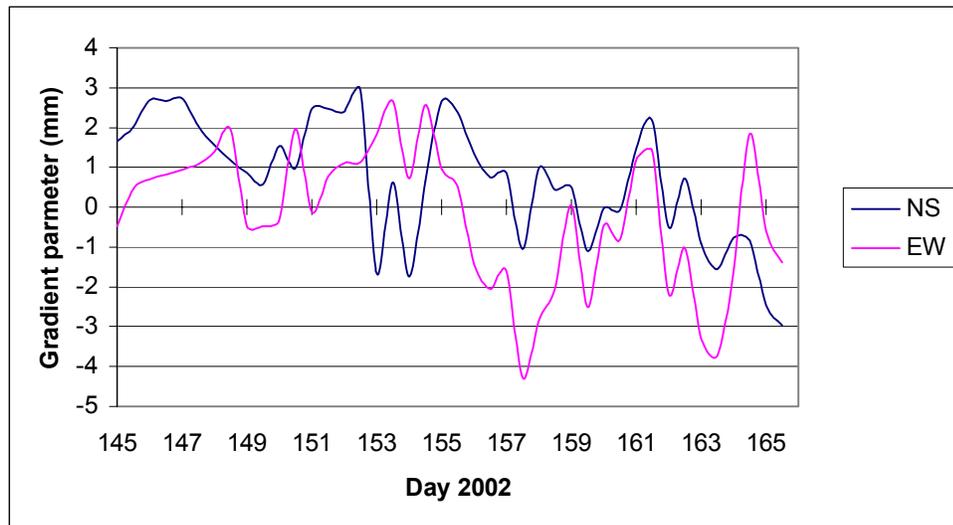
Figure 4.9 Gradient parameters.

4.4.2 Validation of Slant Wet Delays

The slant wet delays from the GPS data were generated using a wet Neill mapping function with zenith wet delays and the gradient parameters, as explained in Section 4.1.2. Zenith wet delays were estimated every hour and gradient parameters were estimated every 12 hours. The elevation cutoff angle was taken to be 15°. Slant wet delays were computed at 30-second intervals for all the satellites in view. The slant wet delays from the GPS data were compared to those derived from the WVR data. Since the WVR estimates the slant wet delays every 6-7 minutes for a particular satellite, they were generated at every 30 seconds for all the satellites in view using a linear interpolation technique. Figure 4.10 shows the RMS slant wet delays for May 3 (Day 123), May 4 (Day 124), May 9 - 12 (Days 129-132), May 25 (Day 145), May 26 (Day 146), and June 1 (Day 152), 2002. These days were selected to generate slant wet delays because RMS zenith wet delays were 1-2 cm on those days.
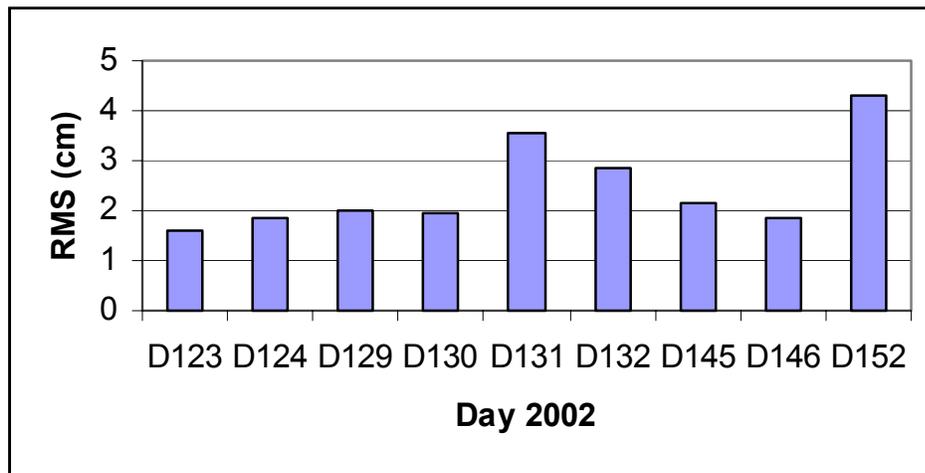
Figure 4.10 RMS slant wet delays.

4.4.3 Factors Affecting Wet Delay Accuracy

Errors affecting the accuracy of zenith wet delays and slant wet delays derived from GPS data were described in Section 4.3. Additional errors arise from the choice of processing parameters. In this section, the impact of various processing parameters is assessed.

4.4.3.1 Elevation Cutoff Angle

Figures 4.11 and 4.12 show the RMS zenith wet delay errors and the RMS slant wet delay errors when GPS data were processed with elevation cutoff angles of $15°$ and $20°$ for May 26, 2002 (Day 146), and results were compared with WVR data. The RMS wet delay errors increase when the elevation cutoff angle for GPS data decreases. Limitations in the mapping function and multipath errors contribute larger RMS wet delay errors for the lower elevation cutoff angle.

Figure 4.11 RMS zenith wet delays for May 26, 2002 (Day 146).
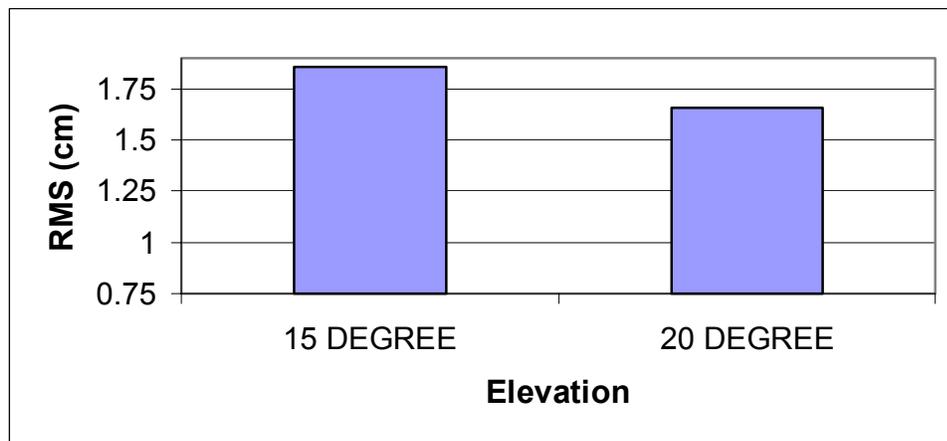
Figure 4.12 RMS slant wet delays for May 26, 2002 (Day 146).

The statistics of the RMS zenith wet delays and the RMS slant wet delays are shown in the Table 4.4:

Table 4.4 Statistics of the RMS Wet Delays for May 26, 2002 (Day 146)

ELEVATION CUTOFF ANGLE	RMS ZENITH WET DELAYS(CM)	RMS SLANT WET DELAYS (CM)	NO. OF OBS. FOR RMS SLANT WET DELAYS
15	0.88	1.86	18890
20	0.81	1.66	16599

Figure 4.13 and 4.14 show RMS slant wet delay errors calculated in different elevation angle bins for elevation cutoff angles of $15°$ and $20°$, respectively, where slant wet delays derived from GPS data are compared with those from the WVR for May 26, 2002 (Day 146). The RMS slant wet delay error increases with lower elevation angles, and the RMS slant delay values are similar for different elevation intervals except for the lower bin of 20-24 degrees. The reason for this is that multipath and mapping function errors contribute increased errors when deriving slant wet delays for lower elevation angle observations.
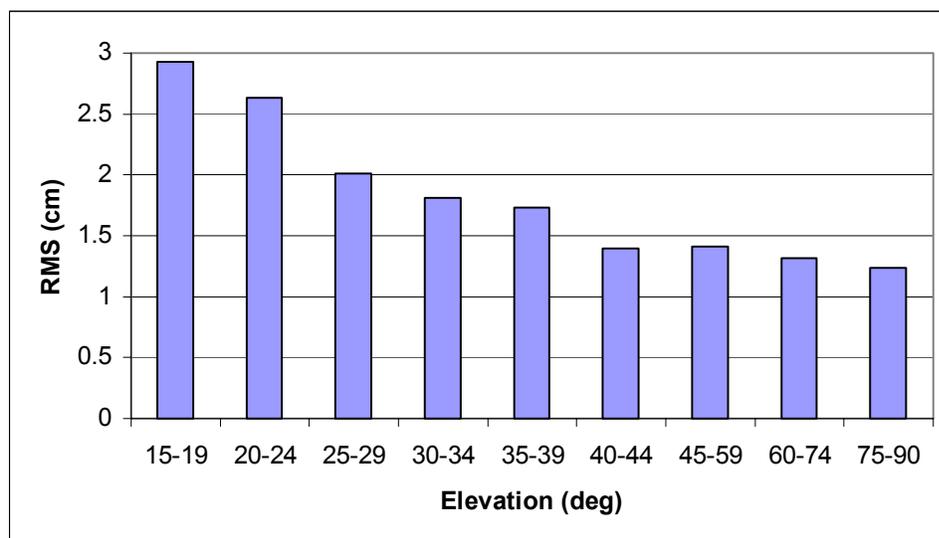
Figure 4.13 RMS slant wet delays for an elevation cutoff angle $15°$ for May 26, 2002 (Day 146).
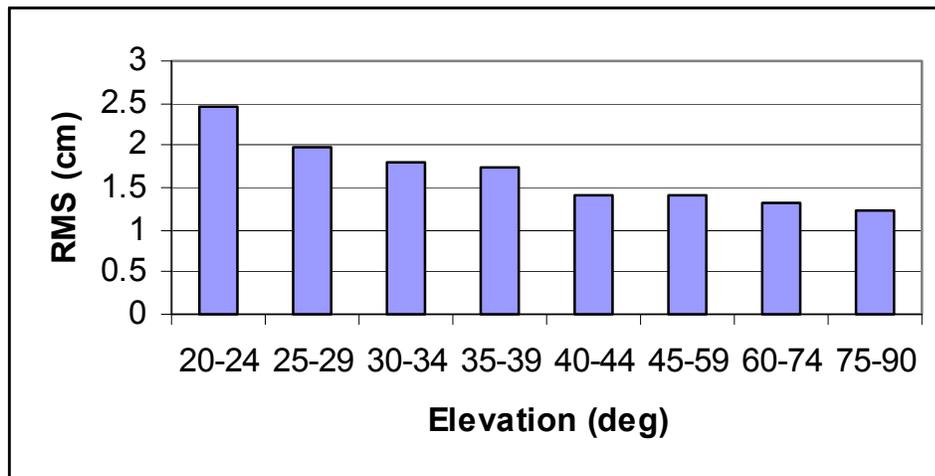
Figure 4.14 RMS slant wet delays for an elevation cutoff angle 20° for May 26, 2002 (Day 146).

4.4.3.2 Batch Processing Interval for Tropospheric Parameter Estimation

Figures 4.15 and 4.16 show the RMS of zenith wet delays and slant wet delays when GPS data were processed to estimate tropospheric parameters in batch processing intervals of one hour and two hours with elevation cutoff angles of 15° and 20° for May 25, 2002 (Day 145). The RMS of wet delays increases for larger batch processing intervals. The reason for this is that water vapor is highly variable with time and space, and the wet delays represent the real atmosphere at a particular time only if tropospheric parameters are estimated at that given time. The RMS of wet delays also increases for the lower elevation cutoff angle. However, there are limitations in estimation of tropospheric parameters for batch intervals less than one hour, such that high RMS values for wet delays are observed. There are a large number of unknown parameters to be determined when the tropospheric parameters are estimated for short batch processing intervals. The errors due to estimation of a large number of unknown parameters would increase the RMS values for wet delay estimation over very short batch intervals.
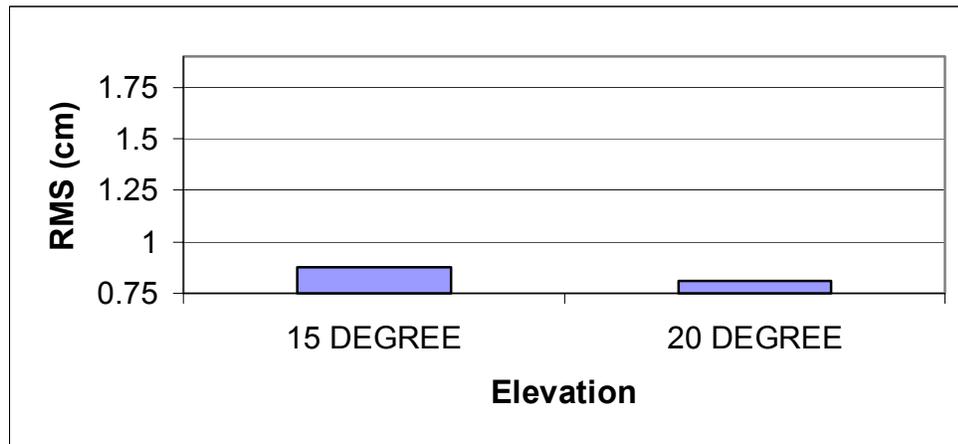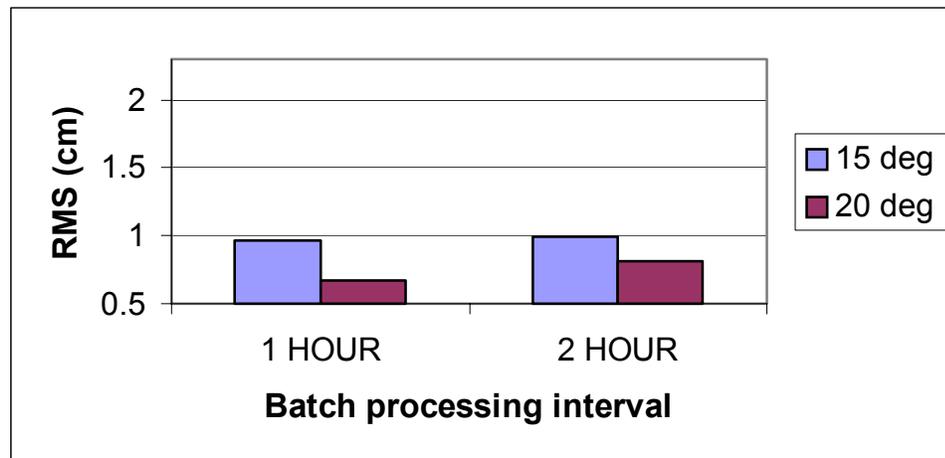
Figure 4.15 RMS zenith wet delays for May 25, 2002 (Day 145).
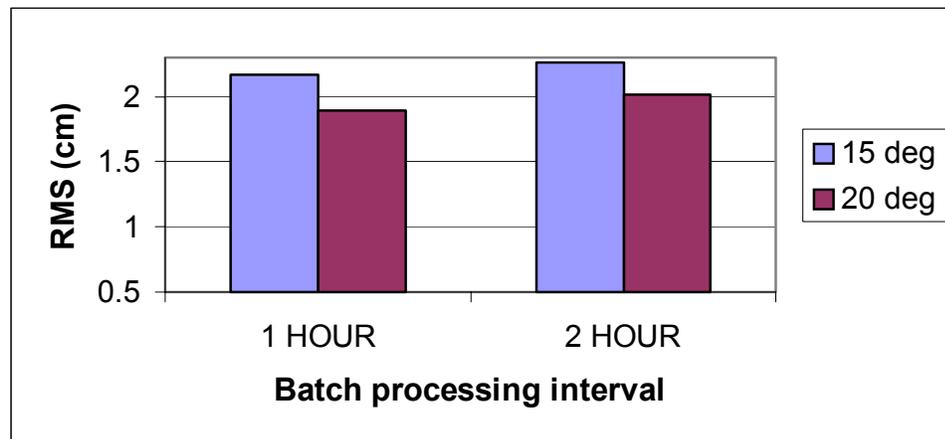
Figure 4.16 RMS slant wet delays May 25, 2002 (Day 145).

The statistics of the RMS wet delays when the tropospheric parameters were estimated for one-hour and two-hour batch processing intervals are listed in Table 4.5:

Table 4.5 Statistics of the RMS Wet Delays for May 25, 2002 (Day 145).

ELEVATION CUTOFF ANGLE	TIME SPAN (HOUR)	RMS ZENITH WET DELAYS (cm)	RMS SLANT WET DELAYS (cm)	NO. OF OBSERVTIONS
15°	1	0.96	2.17	17627
	2	0.99	2.26	17614
20°	1	0.67	1.89	16448
	2	0.81	2.02	16448

4.4.3.3 Selection of Baselines

Figures 4.17 and 4.18 show the RMS of zenith wet delays and slant wet delays when GPS data were processed using reference stations with different baseline lengths with 15° and 20° for June 1, 2002 (Day 152). Tropospheric parameters are estimated for each baseline independently with 1-hour batch intervals. The reference stations are NANO with 737 km baseline length, and PRDS with baseline 25 km with respect to the site on the roof of Engineering Building at the University of Calgary. The objective of this test is to show how the baseline length affects the accuracy of estimation of tropospheric parameters. Figures 4.17 and 4.18 show that when the baseline length decreases the RMS of wet delays increases. The reason for this is that only the relative tropospheric parameters can be estimated for a small local network (short baseline), since observed elevation angles are almost identical for the two reference stations and, therefore, mapping functions would be the same for the two reference stations. In such cases, it becomes difficult to separate and resolve the absolute troposphere parameters at each reference station. If the baseline length increases, the RMS of wet delays decreases and the absolute tropospheric parameters are estimated more reliably. The RMS of wet delays also increases for the lower elevation cutoff angle.
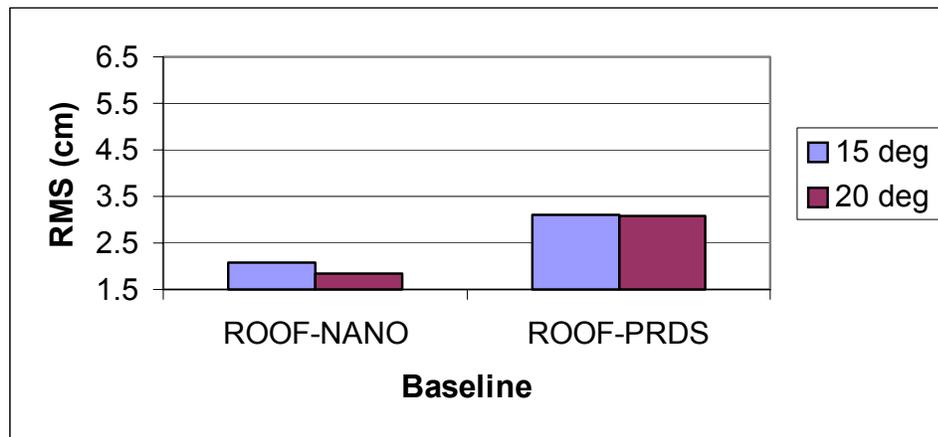
Figure 4.17 RMS zenith wet delays for June 1, 2002 (Day 152).
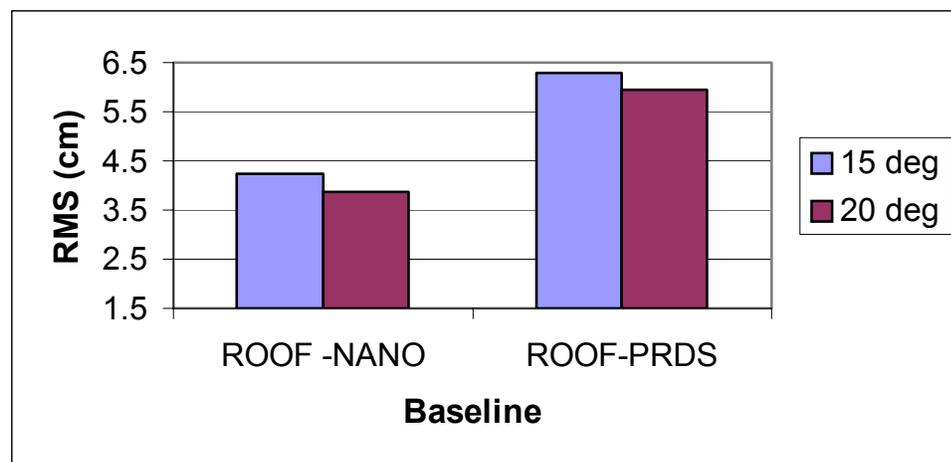
Figure 4.18 RMS slant wet delays for June 1, 2002 (Day 152).

The statistics of the RMS zenith wet delays and RMS slant wet delays for processing with different reference stations (different baseline lengths) are listed in Table 4.6.

Table 4.6 Statistics of the RMS Wet Delays for June 1, 2002 (Day 152)

ELEVATION CUTOFF ANGLE	BASELINE LENGTH (km)	RMS ZENITH WET DELAYS (cm)	RMS SLANT WET DELAYS (cm)	NO. OF OBSERVTIONS
	737	2.07	4.23	17627
15°	25	3.10	6.29	17614
	737	1.83	3.88	16542
20°	25	3.08	5.94	16437

4.4.4 Summary

In summary, the tests conducted here provide information about limitations and optimal processing parameters for the techniques used to estimate the tropospheric parameters and ultimately, derive the slant wet delays, which are required input for tomographic modeling. The elevation cutoff angle needs to be taken as 20° so that the impact of multipath and mapping function error would not be large on the RMS of tropospheric parameter estimation. The batch processing interval of one hour is preferred in order to estimate the tropospheric parameters for the tomographic modeling. The one-hour interval is long enough such that a required minimal number of observations are included in the batch solution, but short enough such that errors due to temporal variations in water vapor are minimized. The processing for the estimation of tropospheric parameters needs to be carried out using multiple reference stations with long baseline lengths. The reason for this is that the absolute tropospheric parameters must be estimated using reference stations with long baseline lengths such that elevation angles (and mapping functions) are not identical at the two stations. It would minimize the RMS error in the estimation of tropospheric parameters.

CHAPTER 5

TOMOGRAPHIC MODELING

Tomographic techniques are used to obtain three-dimensional or four-dimensional images of the tropospheric wet refractivity in a local dense network of GPS receivers. The wet refractivity can then be used to model water vapor in the atmosphere. As explained in Chapter 4, the processing of GPS data can generate slant wet delays. These slant wet delays are the observables in the tomographic processing. Accuracies of slant wet delay estimation were analyzed in Chapter 4.

In this chapter, the technique for the tomographic approach is described in the first section. Simulation results are then shown for various tropospheric conditions to derive the wet refractivity. Finally, tests are conducted using real data from an existing GPS regional network to determine the wet refractivity using the tomographic approach.

5.1 TOMOGRAPHIC TECHNIQUE

Tomography is a particular case of the inverse problem in which measurements are the integration of the model parameters along ray paths (Flores, 2000). In the inverse problem, the observations ($\mathbf{z}$) are considered as the basics to obtain the values of some parameters ($\mathbf{x}$) that are related to observations through a model ($\mathbf{H}$). This can be expressed in the matrix form:

$$\mathbf{z} = \mathbf{H}\mathbf{x} \qquad\qquad (5.1)$$

This approach can be expanded as a Kalman filter, in which parameters at a given epoch are related to those at previous epochs via system models.

Slant wet delays from a dense GPS network are considered as the observables, and parameters describing the wet refractivity may be determined by dividing the troposphere into discrete voxels. The voxel approach has already been applied by previous researchers to determine horizontal and vertical variations in wet refractivity (Flores et al, 2000; Gradinarsky and Jarlemark, 2000). In this thesis, a modification of these previous techniques is proposed (Skone and Shrestha, 2003). The assumptions made for the derivation of the tomographic model in this thesis are that horizontal variations of wet refractivity (N_w) can be described as a low-order expansion in latitude and longitude, and vertical variations of N_w can be described as constant values in discrete layers.

The approach is similar to the voxel algorithms, in that the troposphere is considered to consist of discrete vertical layers. Wet refractivity values for each vertical layer are related in the filtering approach via cross-covariance information. Horizontal variations are estimated using a functional approach, which is essentially equivalent to the smoothing constraints applied in voxel models. Elements of the processing are described as follows.

5.1.1 Measurement Model

The tropospheric delays are related to the neutral refractivity N, which can be represented by the following expression:

$$N = 77.6 \frac{P}{T} + 3.73 \times 10^5 \frac{e}{T^2} = N_h + N_w \qquad (5.2)$$

The variable P represents air pressure in mb, T is the temperature in degrees Kelvin and e is the partial pressure of water vapor in mb. The variables N_h and N_w represent the hydrostatic and wet refractivities, respectively.

The measurement model describes the relationship between the slant wet delays d_w^s and the wet refractivity N_w due to water vapor:

$$d_w^s = 10^{-6} \int\limits_{antenna}^{satellite} N_w ds \tag{5.3}$$

where wet refractivity N_w is a function of latitude (φ), and longitude (λ). In assuming that N_w is constant in a given vertical layer, equation 5.3 can be approximated as a summation:

$$d_w^s = \sum_{j=1}^{n} N_{wj}\left(\varphi_j, \lambda_j\right) ds_j \tag{5.4}$$

where the troposphere consists of n vertical layers and N_{wj} represents the wet refractivity at the mid-point $\left(\varphi_j, \lambda_j\right)$ of the ray with length ds_j in layer j. This concept is illustrated in Figure 5.1.
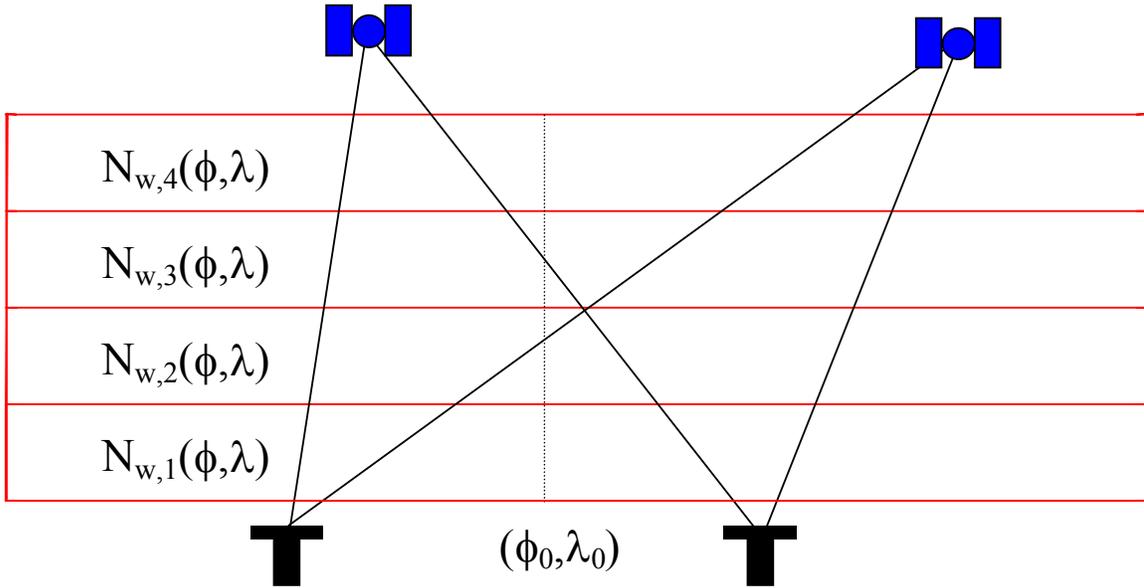
Figure 5.1 Discrete tropospheric layers

Equation 5.4 can be rewritten to include the functional relationship describing the horizontal variations in N_w:

$$d_w^s = \sum_{j=1}^{n} \left(a_{0j} + a_{1j}\Delta\varphi + a_{2j}\Delta\lambda + a_{3j}\Delta\varphi^2 + a_{4j}\Delta\lambda^2 + a_{5j}\Delta\varphi\Delta\lambda \right) ds_j \qquad (5.5)$$

where $a_{0j}, \ldots, a_{5j}$ are coefficients of the expansion for layer j and $\Delta\varphi = \varphi_j - \varphi_0$, $\Delta\lambda = \lambda_j - \lambda_0$. The coordinate (φ_0, λ_0) is the expansion point (generally chosen as the centroid of the GPS network).

5.1.2 System Model

The model unknowns (a_{ij} where i=0,1,…,5 and j=1,…,n) are approximated as stochastic processes in time. A first order Gauss-Markov process is assumed for temporal correlations

in wet refractivity, and the following system model is employed to describe temporal variations in the model coefficients:

$$a_{ij}(t_{k+1})=e^{-\beta(\Delta t)}a_{ij}(t_k)+w \qquad (5.6)$$

where $1/\beta$ is the correlation time and $\Delta t=t_{k+1}-t_k$.

Equation 5.6 provides a statistical description of how model coefficients vary over time. The coefficients at a given time are only partially correlated with those at later epochs, with the normalized autocorrelation function being given as $e^{-\beta(\Delta t)}$. The uncorrelated part of the predicted coefficient $a_{ij}(t_{k+1})$ is described by a white noise sequence w with variance q(t):

$$q(t)=\sigma^2\left[1-e^{-2\beta(\Delta t)}\right] \qquad (5.7)$$

where $q(t)$ is the process noise. For the model implemented here, a correlation time Δt of 1800 seconds is assumed, while the values of σ^2 are set as follows:

$$a_{0j}: \qquad \sigma^2=10\left(\text{mm/km}\right)^2$$

$$a_{1j},a_{2j}: \qquad \sigma^2=2\left(\text{mm/km}\right)^2/\text{deg}^2$$

$$a_{3j},a_{4j},a_{5j}: \qquad \sigma^2=0.5\left(\text{mm/km}\right)^2/\text{deg}^4$$

5.1.3 Prediction and Update Equations

The standard discrete Kalman filter equations are given as follows (after Gelb (1974)), where the superscripts - and + denote prediction and update, respectively.

Prediction (from time t_k to t_{k+1}):

$$\mathbf{x}^-(t_{k+1}) = \mathbf{\Phi}(t_k, t_{k+1})\, \mathbf{x}^+(t_k) + \mathbf{w} \tag{5.8}$$

$$\mathbf{P}^-(t_{k+1}) = \mathbf{\Phi}(t_k, t_{k+1})\, \mathbf{P}^+(t_k)\, \mathbf{\Phi}(t_k, t_{k+1})^{\mathrm{T}} + \mathbf{Q}(t_k) \tag{5.9}$$

Update (at time t_{k+1})

$$\mathbf{x}^+(t_{k+1}) = \mathbf{x}^-(t_{k+1}) + \mathbf{K}[\mathbf{z}(t_{k+1}) - \mathbf{H}(t_{k+1})\, \mathbf{x}^-(t_{k+1})] \tag{5.10}$$

$$\mathbf{P}^+(t_{k+1}) = [\mathbf{I} - \mathbf{K}\mathbf{H}(t_{k+1})]\mathbf{P}^-(t_{k+1}) \tag{5.11}$$

where $\mathbf{K}$ is the gain matrix:

$$\mathbf{K} = \mathbf{P}^-(t_{k+1})\mathbf{H}^{\mathrm{T}}(t_{k+1})[\mathbf{H}(t_{k+1})\mathbf{P}^-(t_{k+1})\mathbf{H}^{\mathrm{T}}(t_{k+1}) + \mathbf{R}(t_{k+1})]^{-1} \tag{5.12}$$

The vector $\mathbf{x}$ represents the unknown coefficients ($a_{0j}, \ldots, a_{5j}$ for all vertical layers j), $\mathbf{\Phi}$ is the transition matrix, and $\mathbf{H}$ is the design matrix. The matrices $\mathbf{R}$ and $\mathbf{P}$ are covariance matrices for the observations $\mathbf{z}$ and estimates of the unknowns $\mathbf{x}$, respectively. Variances for the observations are estimated as follows:

$$\sigma^2 = \left(1.6\ \text{cm}^2\right)/\sin\varepsilon \tag{5.13}$$

where ε is the satellite elevation angle. The observation variances are based on the slant wet delay accuracies, as a function of elevation angle, derived in Section 4.4.

The $\mathbf{P}$ matrix is fully populated, where cross-covariances are used to model the correlations between parameters in different vertical layers. The cross-correlation is derived as a function of distance between the given layers. Covariances also depend on height, where lower correlations are assumed for the lower troposphere layers – where inversion events and irregular variations in the vertical wet refractivity profile may occur.

5.2 SIMULATIONS

Simulation results presented below focus primarily on a few aspects of the complex tomographic problems. Extensive simulations were performed in order to analyze the resolution and sensitivity of the tomographic solution. Also, the impact of elevation cutoff angle and height of GPS stations on the accuracy of wet refractivity estimates were tested.

5.2.1 Software

Simulation processing is carried out using Matlab programs based on the Satellite Navigation Toolbox 2.0™ from GPSoft GPS simulation software. The GPSoft programs simulate GPS satellite constellations, error sources and observations, in addition to computing various positioning solutions. The programs were modified to simulate slant wet delays and associated errors at various stations within a regional GPS network (Skone and Shrestha, 2003). The tomographic estimation technique was also implemented in the software to derive the 4-D wet refractivity solution. Observations are generated every 300 seconds. A "standard" or "inverse" wet refractivity profile may be chosen as truth for the simulation, and the slant wet delays are simulated for each satellite-receiver line-of-sight using equation 5.3. Random errors are added to the simulated observations, with magnitudes dependent on elevation angle. Appropriate magnitudes of these errors are determined from the accuracies of slant wet delays derived in Section 4.4. Accuracies of the tomographic solutions are then derived by comparing the model solution with the truth profile for wet refractivity.

The model estimates vary over time, and are partially correlated with those at earlier epochs. Temporal variations of model estimates are controlled by the system model included in the Kalman filter, which is given in equation 5.6. For the results generated here, a correlation time of 1800 seconds is assumed. The initial convergence time may be decreased by setting a lower correlation time. In such cases, however, the filter may

converge too rapidly to incorrect values. After the initial convergence, model estimates vary only with temporal variations of the non-stationary troposphere – averaging through the error effects such as white noise. The results generated in the simulation have an overall convergence time of approximately 5700 seconds. This initial convergence period is not a limitation in generating results for practical applications. Once initialised, the filter would run continuously for days or even months at a time.

Two types of refractivity profiles are used in the simulations:
1) A vertical wet refractivity profile with an inversion layer near the surface (Nw_inv).
2) A vertical wet refractivity profile that decreases exponentially with height (Nw_ave).

The simulated slant wet delays are derived through integration of theoretical N_w along each satellite-receiver line-of-sight (e.g. equation 5.3). The vertical wet refractivity is simulated using equation 5.2 and the following expressions for partial water vapor pressure (e) and temperature (T) as a function of height (H):

$$T=T_0-6.5H \tag{5.14}$$

$$e=\frac{U}{100}\exp\left(-37.2465+0.213166T-0.0002569T^2\right) \tag{5.15}$$

where H is in km, T is in degrees Kelvin and e is in mb. The variable U and T_0 represents relative humidity (in percent) and temperature at sea level, respectively.

The simulated slant wet delay observations have additional random errors imposed as a function of elevation angle, with magnitude determined from equation 5.13. The inversion event is simulated by using equations 5.14 and 5.15 for heights above 2 km, and imposing a positive wet refractivity gradient (as a function of height) in the altitude range 0-2 km.

In order to simulate a realistic network, and to derive results relevant for processing of real data in Section 5.3.2, the simulated network consists of five GPS stations at location identical to those in the Southern California Integrated GPS Network (SCIGN). The baselines between these stations vary from 19 km to 45 km. These GPS stations are located at different heights that range from sea level up to about 1600 m. The details of this network are given in Section 5.3.1. The geometry, with receivers located at different heights, is particularly well suited for tomography. This network was used for simulation tests to verify if the tomographic approach could be applied, so that the real data from this network could be used to define a local tomographic model. Figure 5.2 shows network geometry for simulations, and Figure 5.3 shows the 3-D lines-of-sight through the atmosphere for all stations.
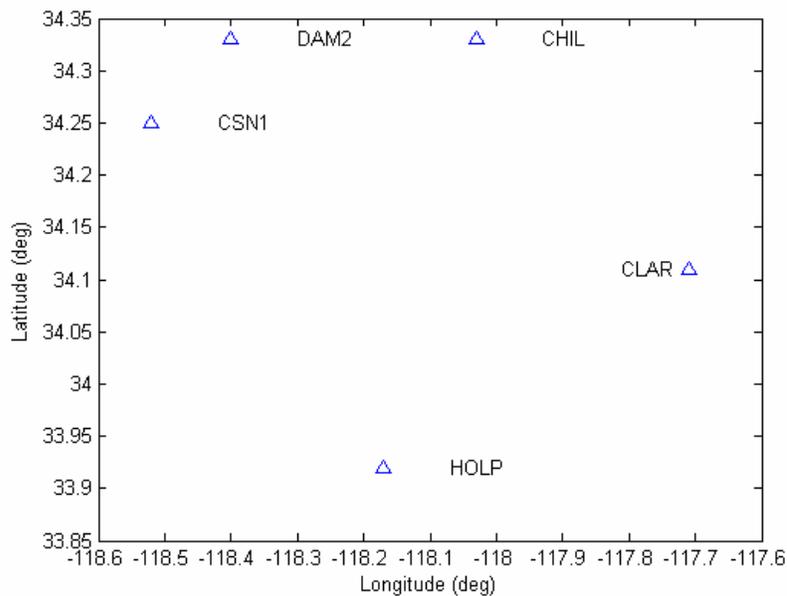
Figure 5.2 Network geometry for simulations.
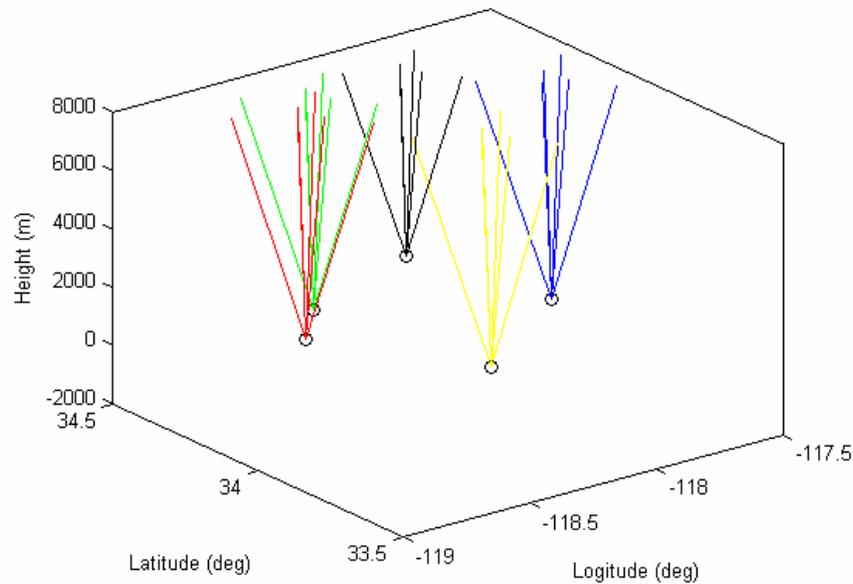
Figure 5.3 Signal paths between satellites and stations.

5.2.2 Testing

Simulation tests were carried out using the two atmospheric profiles: average exponential decay of N_w with height (Nw_ave), and inversion layer in N_w profile near the surface (Nw_inv). The following tests were conducted to define the wet refractivity using the tomographic approach:

- vertical resolution analysis
- reference station vertical geometry analysis
- elevation cutoff angle analysis

These tests were conducted to achieve the following objectives:
- Define the requirement to establish a GPS network for estimation of the wet refractivity using the tomographic approach. The analysis of reference stations differential heights

gives requirements for the vertical network geometry necessary to establish a GPS network (or use an existing GPS network) for estimation of the 4-D wet refractivity for GPS meteorology.

- Define the optimal processing parameters required to achieve better accuracies for the estimation of 4-D wet refractivity using a GPS network. The vertical resolution analysis and the elevation cutoff angle analysis are used to determine requirements for tomographic processing.

5.2.2.1 Vertical Resolution Analysis

This test helps to define the appropriate processing technique to derive better accuracies for estimation of the wet refractivity. As the troposphere is divided into a numbers of vertical layers in the tomographic approach, the following tests were conducted to determine the vertical resolution which may be achieved reliably. Results are generated for both the Nw_ave and Nw_inv profiles. Table 5.1 shows processing parameters used for simulations to test vertical resolution in the tomographic model.

Table 5.1 Processing Parameters

PARAMETERS	MAGNITUDE
Number of steps for trace along line-of-sight path	200
Percent humidity at surface	50
Temperature at surface	293° K
Number of reference stations	5
Top vertical layer height for troposphere	8000 m
Elevation mask angle for slant wet delay observations	15°
Number of vertical troposphere layers for adjustment	8 and 16

5.2.2.1.1 Results for Nw_ave Profile

Simulations were carried out using 8 and 16 vertical layers to test the sensitivity, vertical resolution, and accuracy of wet refractivity estimates. For both 8 and 16 layers, the upper troposphere altitude is taken to be 8 km. The 8-layer model therefore consists of eight 1-km vertical layers, while the 16-layer model consists of sixteen 500-m layers. Figure 5.4 shows the N_w estimates for 8 and 16 layers of the troposphere, as compared with truth values of the vertical Nw_ave profile. The wet refractivity shown in Figure 5.4 is for the center of the network and the filter convergence time was 5700 seconds.

Figure 5.4 Wet refractivity estimates derived from simulations for different vertical resolutions for the Nw_ave profile after 5700 seconds convergence time.

Table 5.2 shows the wet refractivity errors for both 8 and 16 layers of the troposphere, as compared with truth values of the vertical Nw_ave profile.

Table 5.2 Wet Refractivity Errors for Nw_ave (mm/km)

HEIGHT (m)	Nw ERRORS (mm/km)	
	8 LAYERS	16 LAYERS
500	2.62	0.44
1500	-1.30	0.58
2500	-0.46	0.54
3500	-0.02	0.40
4500	0.11	0.14
5500	0.08	-0.13
6500	0.02	-0.03
7500	0.05	0.27

Figure 5.5 shows overall accuracies of wet refractivity estimates as a function of time for both the 8-layer and 16-layer models, for the Nw_ave profile. The Kalman filter was used to estimate the wet refractivity and it required approximately one hour for convergence to a stable solution. Figure 5.5 shows that the accuracy of the estimated wet refractivity improved when a larger number of vertical layers was used in the model. The overall RMS values for wet refractivity estimates were 0.36 mm/km for 16 vertical layers, and 1.05 mm/km for 8 vertical layers after 5700 seconds convergence time.

Figure 5.5 Overall wet refractivity RMS values derived for simulations with different vertical resolutions, as a function of time, for Nw_ave.

5.2.2.1.2 Results for Nw_inv Profile

Simulations were carried out for an inversion layer in the wet refractivity profile near the surface (Nw_inv). As in Section 5.2.2.1.1, the tropospheric height was divided into 8 and 16 vertical layers to test the sensitivity of wet refractivity estimation. Figure 5.6 shows the wet refractivity estimates for different vertical resolutions, as compared with truth values, for the simulated inversion event.
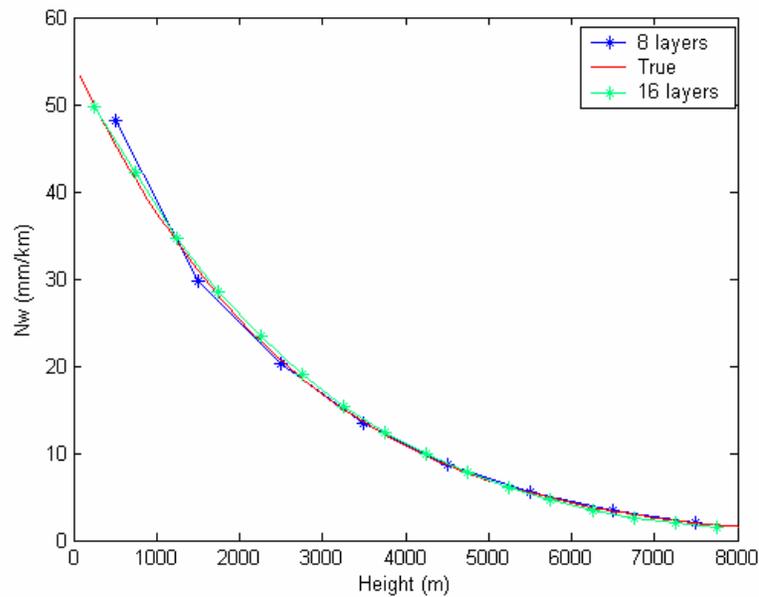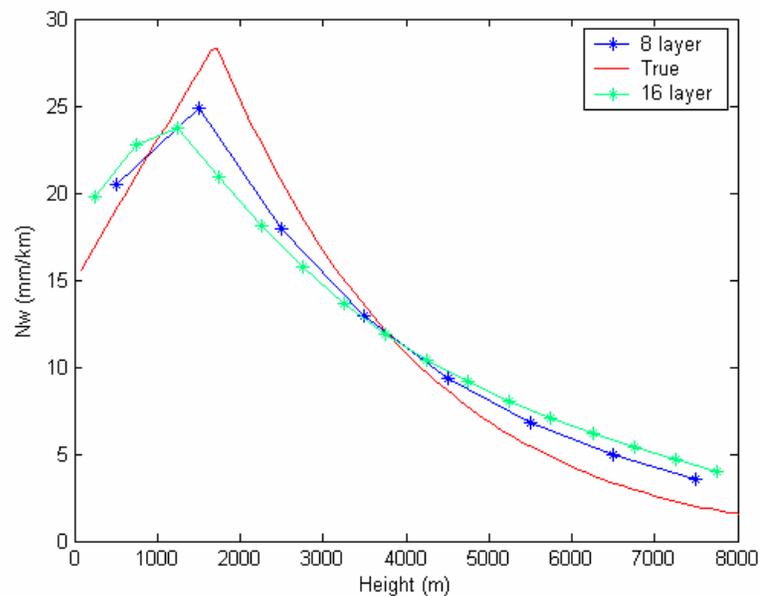

Figure 5.6 Wet refractivity estimates derived from simulations with different vertical resolution, for an inversion event after 5700 seconds convergence time.

Table 5.3 shows wet refractivity errors as compared with the truth values, for simulations with 8 vertical layers and 16 vertical layers for an inversion event.

Table 5.3 Wet Refractivity Errors for Nw_inv (mm/km)

HEIGHT (m)	Nw ERRORS (mm/km)	
	8 LAYERS	16 LAYERS
500	1.51	2.25
1500	-2.14	-4.69
2500	-2.72	-3.73
3500	-0.53	-0.69
4500	0.74	1.15
5500	1.38	2.11
6500	1.60	2.45
7500	1.60	2.40

Figure 5.7 shows the overall accuracies for wet refractivity estimates as a function of time, for the Nw_inv simulations carried out with 8 and 16 vertical layers. This figure shows that the overall accuracies of wet refractivity estimates are degraded when the number of vertical layers is increased. The overall RMS values for wet refractivity estimates were 2.84 mm/km with 16 vertical layers, whereas it was 1.66 mm/km with 8 vertical layers after 5700 seconds convergence time.
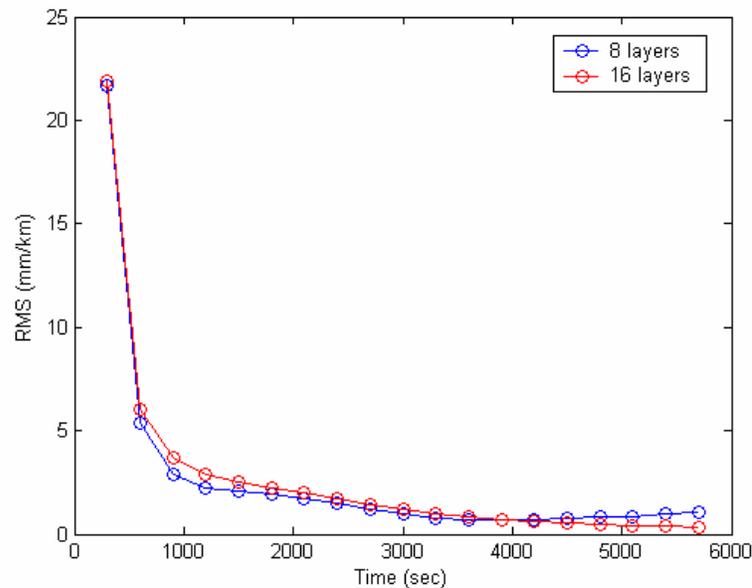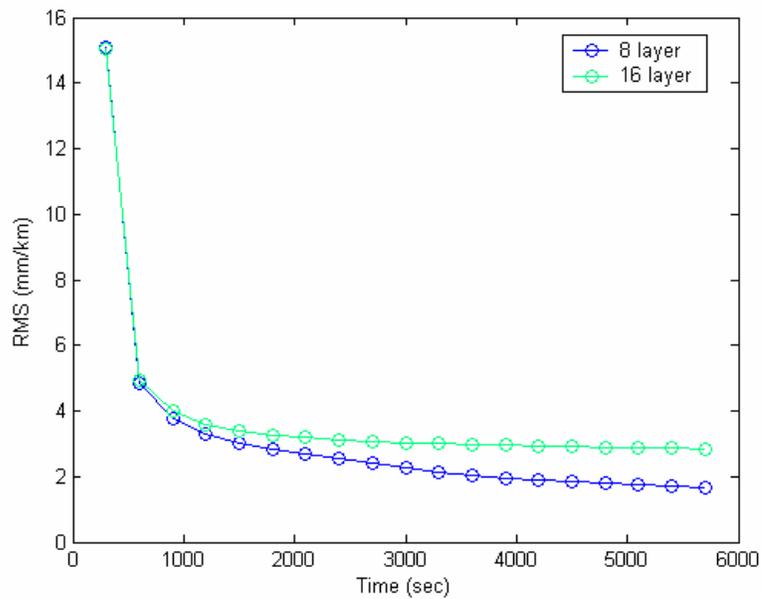
Figure 5.7 Overall wet refractivity RMS values derived for simulations with different vertical resolution, for inversion event.

5.2.2.2 Reference Station Vertical Geometry Analysis

The tomographic approach is sensitive to the vertical station separation within a regional network. The vertical resolution may be degraded for flat networks, with poor observability in the vertical direction. Therefore the following tests were conducted to determine the impact of the vertical station separation on accuracies of wet refractivity estimates. Simulations are conducted for both the Nw_ave and Nw_inv profiles. Table 5.4 shows processing parameters used for simulations to test vertical station separation.

Table 5.4 Processing Parameters

PARAMETERS	MAGNITUDE
Number of steps for trace along line-of-sight path	200
Percent humidity at surface	50
Temperature at surface	293° K
Number of reference stations	5
Top vertical layer height for troposphere	8000 m
Elevation mask angle for slant wet delay observations	15°
Number of vertical troposphere layers for adjustment	8

5.2.2.2.1 Results for Nw_ave Profile

A simulation to assess the impact of vertical station separation was carried out using the five stations of the SCIGN network, with fixed latitudes and longitudes, but with varying relative height differentials. The relative vertical station separations were taken to be 50 m, 200 m, and 400 m. The lowest station is taken to be HOLP, with stations CSN1, CLAR, DAM2 and CHIL set at progressively higher altitudes, respectively. Figure 5.8 shows the network height profiles for simulations.
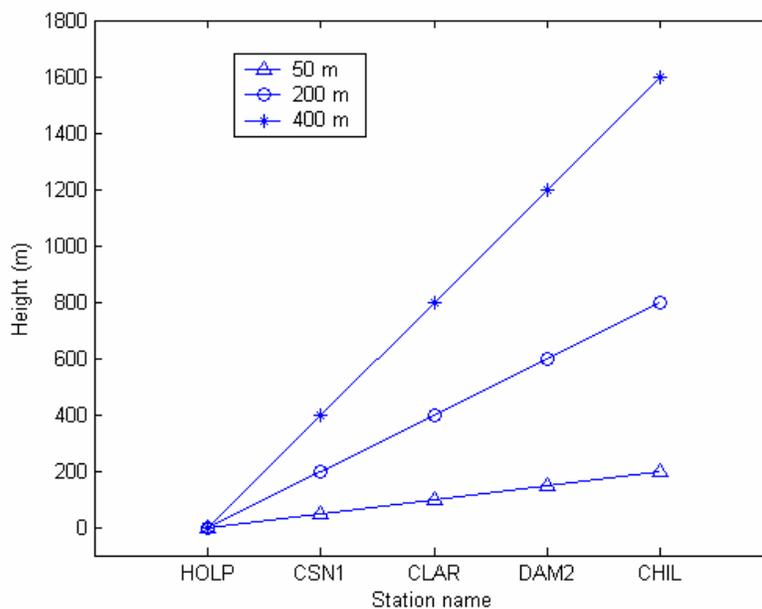
Figure 5.8 Network height profiles for simulations.

Figure 5.9 shows the wet refractivity estimates for different vertical station separations, as compared with the truth profile, for the Nw_ave profile. The wet refractivity estimates are shown at a time 5700 seconds after filter initialization. Table 5.5 shows the wet refractivity errors as compared with truth values for simulations with varying vertical station separations, for the Nw_ave profile.
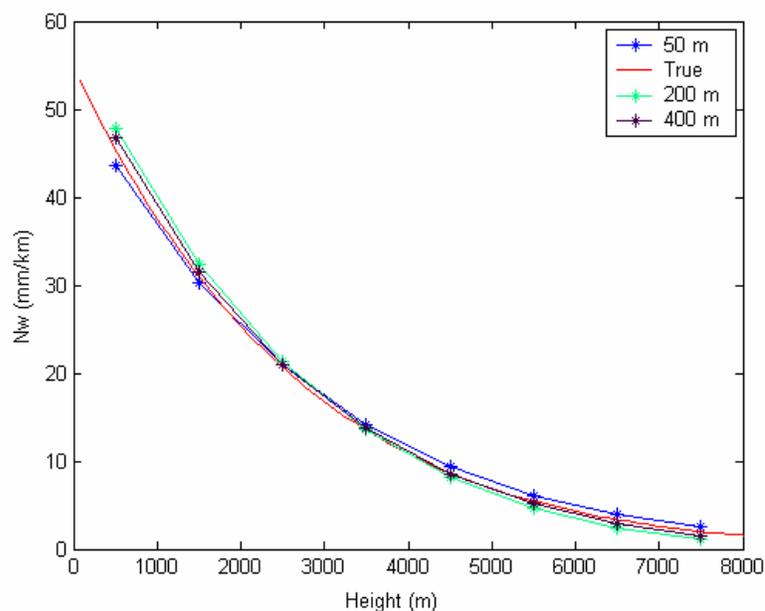
Figure 5.9 Wet refractivity estimates derived from simulations with different vertical station separations, for the Nw_ave profile, 5700 s after filter initialization.

Table 5.5 Wet Refractivity Errors for Nw_ave (mm/km)

HEIGHT (m)	VERTICAL STATION SEPARATIONS		
	50 m	200 m	400 m
500	-1.91	2.21	1.32
1500	-0.63	1.32	0.43
2500	0.23	0.67	0.39
3500	0.67	0.11	0.22
4500	0.78	-0.41	-0.04
5500	0.69	-0.82	-0.31
6500	0.56	-1.03	-0.47
7500	0.49	-0.94	-0.43

Figure 5.10 shows the convergence of wet refractivity RMS values over time for the various vertical station separations. The simulation was carried out for the Nw_ave profile. The overall RMS values were 0.88 mm/km, 1.11 mm/km, and 0.58 mm/km, respectively, for vertical station separations of 50 m, 200 m, and 400 m after 5700 seconds time.
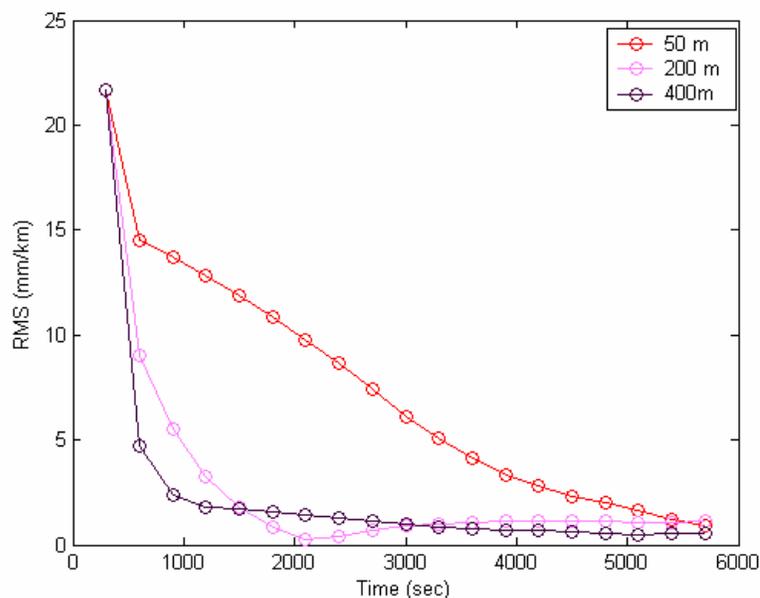
Figure 5.10 Overall wet refractivity RMS values for simulations with different vertical station separations, for Nw_ave.

5.2.2.2.2 Results for Nw_inv Profile

A simulation similar to that carried out in the previous section is conducted here, but for an inversion event (Nw_inv). Figure 5.11 shows results of these simulations for varying vertical station separations.
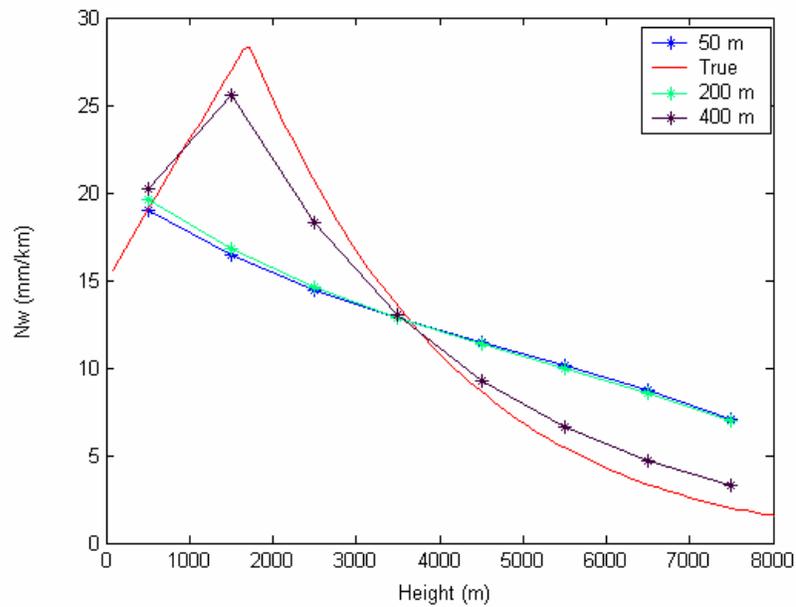
Figure 5.11 Wet refractivity estimates derived from simulations for different vertical station separations, for Nw_inv, after 5700 seconds convergence time.

Table 5.6 shows the wet refractivity errors as compared with the truth values for simulations of the Nw_inv profile and vertical station separations of 50 m, 200 m, 400 m.

Table 5.6 Wet Refractivity Errors for Nw_inv (mm/km)

HEIGHT (m)	VERTICAL STATION SEPARATION		
	50 m	200 m	400 m
500	0.02	0.6	1.23
1500	-10.57	-10.25	-1.45
2500	-6.21	-6.08	-2.41
3500	-0.65	-0.64	-0.47
4500	2.81	2.73	0.65
5500	4.7	4.57	1.19
6500	5.38	5.24	1.37
7500	5.09	4.95	1.33

Figure 5.12 shows the convergence of wet refractivity RMS values over time for the different vertical station separations. These simulations were carried out for the Nw_inv profile. The overall wet refractivity RMS values were 5.42 mm/km, 5.28 mm/km, and 1.37 mm/km, respectively, for vertical height differentials of 50 m, 200 m, and 400 m after 5700 seconds convergence time. These results show that a vertical network geometry with receivers located at significantly different heights is required to resolve irregular features such as an inversion event.
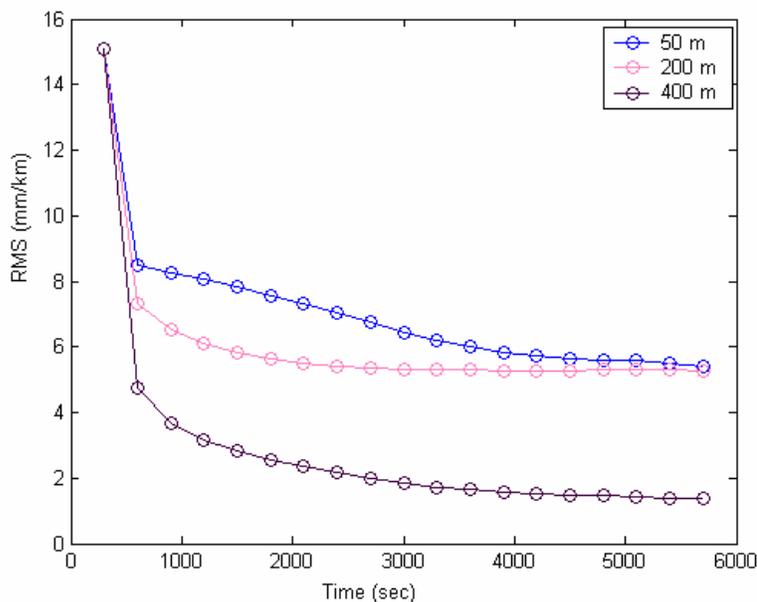
Figure 5.12 Overall wet refractivity RMS values for varying vertical station separations, for the Nw_inv profile.

As shown in Tables 5.5 and 5.6, the height separation between the stations in the network has a large impact on the accuracy of wet refractivity estimation. The wet refractivity errors are improved when the vertical height differential is larger (400 m). Significant vertical height separation is required to resolve the 4-D wet refractivity profiles. A flat network is adequate for smoothly varying vertical profiles, but gives poor resolution for the inversion event.

5.2.2.3 Elevation Cutoff Angle Analysis

Further simulations are conducted using different elevation cutoff angles for both the Nw_ave and Nw_inv profiles. The lower-elevation slant wet delay observations have larger errors, due to multipath and limitations in mapping functions (Section 4.4). The lower-elevation lines-of-sight pass through a primarily horizontal path, however, and can help to improve the geometry of the tomographic solution. Tests are conducted here to determine an optimal elevation cutoff angle for the tomographic processing. Table 5.7 shows processing parameters used for simulations to define the suitable elevation cutoff angle for the tomographic model.

Table 5.7 Processing Parameters

Parameters	Magnitude
Number of steps for trace along line-of-sight path	200
Percent humidity at surface	50
Temperature at surface	$293°$ K
Number of reference stations	5
Top vertical layer height for troposphere	8000 m
Elevation mask angle for slant wet delay observations	$10°, 15°$ and $20°$
Number of vertical troposphere layers for adjustment	8

5.2.2.3.1 Results for Nw_ave Profile

Simulations were carried out for elevation cutoff angles of $10°$, $15°$, and $20°$ for the reference stations within the network. Figure 5.13 shows the results of these simulations for the Nw_ave profile.
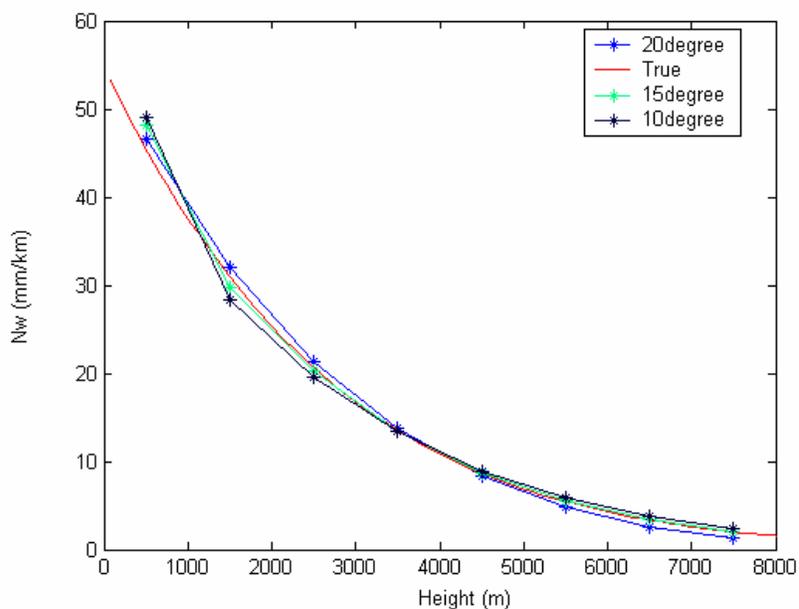
Figure 5.13 Wet refractivity estimates derived from simulations for different elevation cutoff angles, for the Nw_ave profile after 5700 s convergence time.

Table 5.8 shows the wet refractivity errors as compared with truth values for simulations of the Nw_ave profile and elevation cutoff angles of $10°$, $15°$, and $20°$.

Table 5.8 Wet Refractivity Errors (mm/km)

HEIGHT (m)	ELEVATION CUTOFF ANGLES		
	$10°$	$15°$	$20°$
500	3.49	2.62	1.13
1500	-2.62	-1.30	1.09
2500	-1.12	-0.46	0.65
3500	-0.14	-0.02	0.21
4500	0.30	0.11	-0.23
5500	0.44	0.08	-0.61
6500	0.45	0.02	-0.81
7500	0.45	0.05	-0.75

Figure 5.14 shows the overall RMS values of wet refractivity estimates over time for elevation cutoff angles of $10°$, $15°$, and $20°$. The simulation was carried out for the Nw_ave profile. The overall RMS values for wet refractivity estimates were 1.62 mm/km, 1.05 mm/km, and 0.72 mm/km, respectively, for elevation cutoff angles of $10°$, $15°$, and $20°$ after 5700 seconds convergence time.
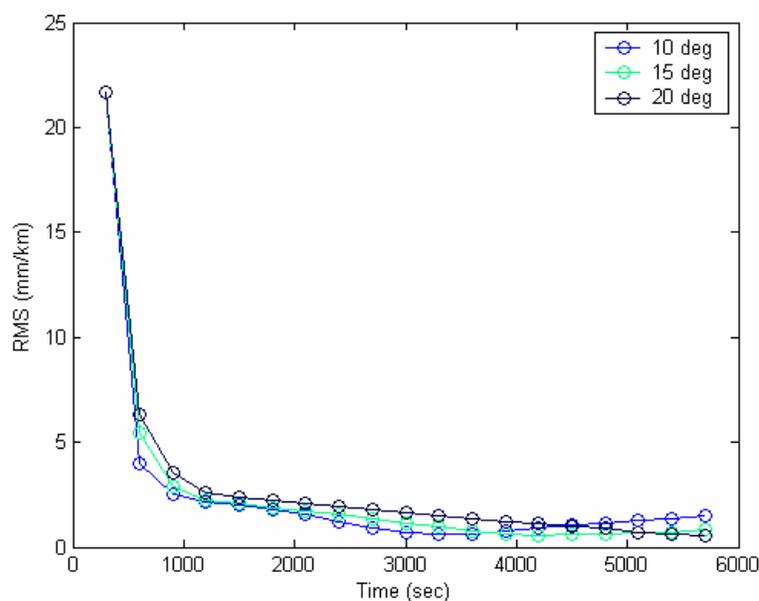
Figure 5.14 Wet refractivity RMS values for simulations with different elevation cutoff angles, for the Nw_ave profile.

5.2.2.3.2 Results for the Nw_inv Profile

Simulations similar to those in Section 5.2.2.3.1 were carried out for elevation cutoff angles of $10°$, $15°$, and $20°$ for all reference stations within the network. Figure 5.15 shows results of these simulations for an inversion layer Nw_inv profile.
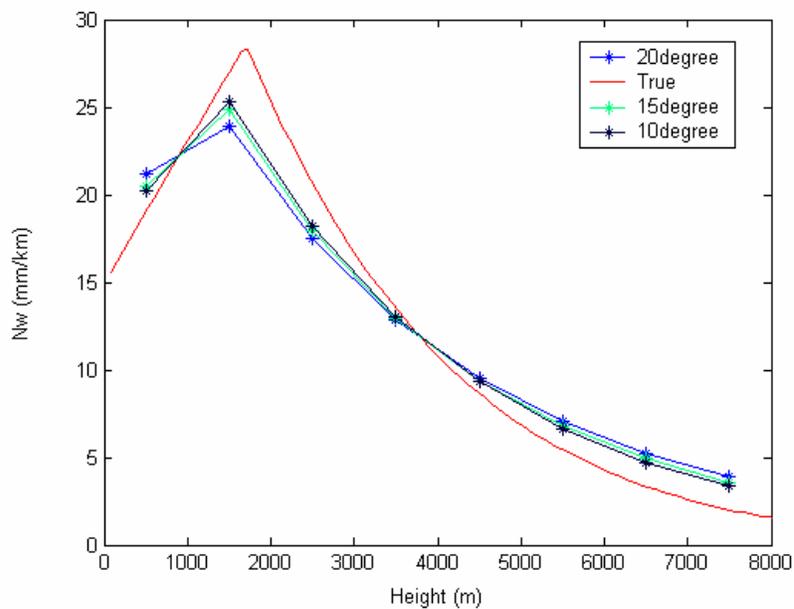
**Figure 5.15 Wet refractivity estimates derived from simulations with different
elevation cutoff angles, for the Nw_inv profile, after 5700 seconds convergence time.**

Table 5.9 shows the wet refractivity errors as compared with truth values for simulations
carried out with the Nw_inv profile and elevation cutoff angles of $10°$, $15°$, and $20°$.

Table 5.9 Wet Refractivity Errors for the Nw_inv Profile (mm/km)

HEIGHT (m)	ELEVATION CUTOFF ANGLE		
	$10°$	$15°$	$20°$
500	1.21	1.51	2.14
1500	-1.67	-2.14	-3.13
2500	-2.47	-2.72	-3.20
3500	-0.46	-0.53	-0.64
4500	0.69	0.74	0.87
5500	1.24	1.38	1.66
6500	1.40	1.60	1.94
7500	1.36	1.55	1.89

Figure 5.16 shows the variation of wet refractivity RMS values over time for elevation cutoff angles of $10°$, $15°$, and $20°$. The simulations were carried out for the Nw_inv profile. The overall RMS values for Nw estimates were 1.43 mm/km, 1.66 mm/km, and 2.12 mm/km, respectively, for elevation angles of $10°$, $15°$, and $20°$ after 5700 seconds convergence time. In this case, accuracies are clearly improved for lower elevation angles.
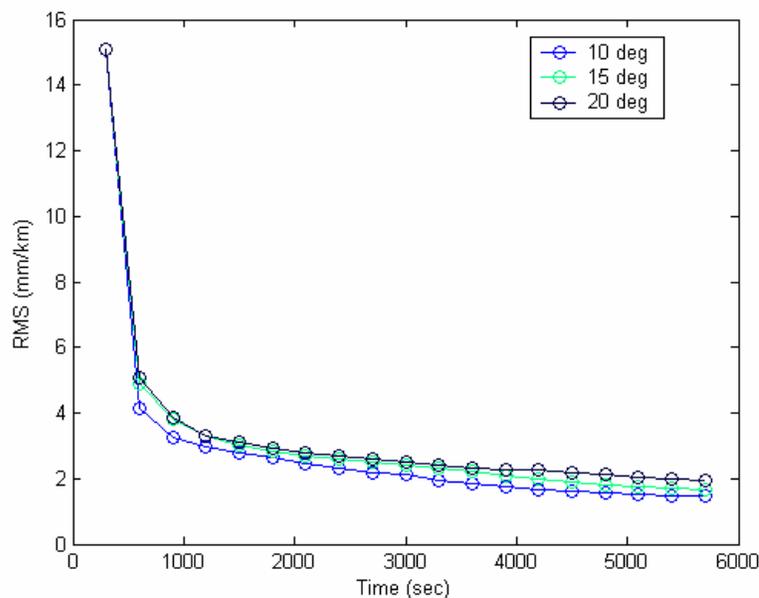
Figure 5.16 Wet refractivity RMS values for simulations with different elevation cutoff angles, for the Nw_inv profile.

5.2.3 Summary of Simulation Results

The simulation tests allow determination of optimal processing parameters and network geometries required for estimation of wet refractivity within a regional network. The wet refractivity values may be used for GPS meteorology and precise positioning applications. The following paragraphs give the summary of simulation results:

- The vertical resolution tests were conducted to define the appropriate number of discrete vertical layers to be used in the tomographic model. The tests were carried

out for 8-layer and 16-layer models. Both the Nw_ave and Nw_inv profiles were evaluated. RMS values for wet refractivity errors were 0.36 mm/km for the 16 vertical layers, and 1.05 mm/km for the 8 vertical layers (after a convergence time of 5700 seconds) for the Nw_ave profile. The overall RMS values for wet refractivity estimates were 2.84 mm/km for 16 vertical layers, whereas it was 1.66 mm/km for 8 vertical layers (after the convergence time of 5700 seconds) for the Nw_inv profile. The RMS values are higher for simulations with 8 layers for Nw_ave profile while RMS errors were higher for simulations conducted with 16 layers for the Nw_inv profile. It is recommended that processing be conducted with 8 layers as the inversion profile of wet refractivity represents natural irregularities in the atmosphere.

- Tests with varying vertical station separations were conducted to define the vertical network geometry requirements for estimation of wet refractivity. The tomographic approach is sensitive to the vertical station separation within a regional network. The vertical resolution may be degraded for flat networks, with poor observability on the vertical direction. A simulation was conducted to define the impact of vertical station separation using five stations of the SCIGN Network, with fixed latitudes and longitudes, but varying relative height differentials, for both the Nw_ave and Nw_inv profiles. The relative vertical station separations were taken to be 50 m, 200 m, and 400 m. The overall RMS values for wet refractivity were 0.88 mm/km, 1.11 mm/km, and 0.58 mm/km, respectively, after a convergence time of 5700 seconds, for vertical station separations of 50 m, 200 m, and 400 m and the Nw_ave profile. The overall RMS values for wet refractivity were 5.42 mm/km, 5.28 mm/km, and 1.37 mm/km, respectively, after a convergence time 5700 seconds, for vertical height differentials of 50 m, 200 m, and 400m and the Nw_inv profile. It is recommended that GPS networks used for tropospheric tomography have vertical station separations of 400 m or more in order to resolve irregular features, such as inversion events, in the lower atmosphere.

- The elevation cutoff angle tests were conducted to determine an optimal elevation cutoff angle for reliable tomographic processing. The tomographic processing was conducted using elevation cutoff angles of $10°$, $15°$, and $20°$ for all reference stations. Both the Nw_ave and Nw_inv profiles were simulated. Overall RMS values were 1.62 mm/km, 1.05 mm/km, and 0.76 mm/km, respectively, for elevation cutoff angles of $10°$, $15°$, and $20°$ after a convergence time of 5700 seconds for the Nw_ave profile. Overall RMS values were 1.43 mm/km, 1.66 mm/km, and 2.12 mm/km, respectively, for elevation angles of $10°$, $15°$, and $20°$ after a convergence of 5700 seconds for the Nw_inv profile. The recommendation is made to keep a $10°$ elevation cutoff angle for tomographic processing.

5.3 WET REFRACTIVITY ESTIMATION USING A GPS NETWORK

Results of Section 5.2 were generated for controlled simulations, where processing parameters, wet refractivity profiles, and network geometries were easily varied. These results provide information regarding optimal processing parameters and network geometry requirements to derive accurate profiles of wet refractivity in the lower atmosphere using GPS. It is important to conduct further tests of this technique using real GPS data from an existing network.

The tomographic technique was tested with observations from GPS reference stations in the SCIGN network, in order to determine the wet refractivity in a local network. For this purpose, six stations in the SCIGN network have been used. These stations were chosen because the height differences between stations and baseline lengths between stations are suitable to recover wet refractivity using the tomographic technique. The following sections describe the data set, processing and results of the tomographic modeling.

5.3.1 Data Set

The GPS data and meteorological data were downloaded from the Scripps Orbit and Permanent Array Center (SOPAC) web site. Six stations from the California network were used to test the tomographic technique for determination of the 4-D wet refractivity. Stations CHIL, DAM2, CSN1, CLAR, and HOLP were used to define the wet refractivity within the network. Station JPLM was used as an independent test site to check the validity of wet refractivity estimates calculated using the tomographic technique. Accuracies were evaluated by deriving slant wet delays for all satellite-receiver lines-of-sight at JPLM from the wet refractivity estimates derived using the five stations in the network, and then comparing these predicted values with the slant wet delays derived for JPLM using Bernese software version 4.2. Figure 5.17 shows the geographical location of the stations in the SCIGN network. Table 5.10 lists the coordinates and heights of the reference stations in the SCIGN network.
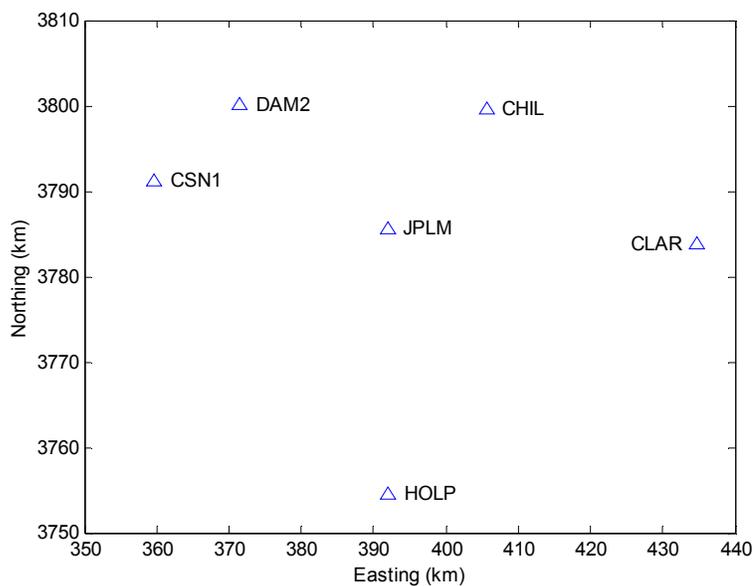
Figure 5.17 Geographical location of stations in SCIGN network.

Table 5.10 Coordinates and Heights of the Reference Stations in the SCIGN Network

STATION NAME	LATITUDE (deg min sec)	LONGITUDE (deg min sec)	HEIGHT (m)
CHIL	34 20 00.31	-118 01 33.58	1567.51
DAM2	34 20 05.40	-118 23 48.70	583.80
CSN1	34 15 12.77	-118 31 25.71	261.52
CLAR	34 06 35.73	-117 42 31.70	373.64
HOLP	33 55 28.33	-118 10 05.40	-6.68
JPLM	34 12 17.35	-117 23 48.70	423.98

As shown in Figure 5.17 and Table 5.10, the stations are well-distributed over a regional area and are located at different heights that range from slightly below sea level up to approximately 1600 m. The geometry, with receivers located at different heights and small baseline lengths, is particularly well suited for tomography.

The stations CHIL, DAM2, CSN1, CLAR, are HOLP are equipped with ASHTECH Z-XII3 receivers and the station JPLM is equipped with a ROGUE SNR-8100 receiver. These are all survey-grade dual frequency receivers. The surface pressure, temperature and humidity data were provided from each site with 10 minute sampling interval, where the stations are equipped with MET3 sensors.

5.3.2 Accuracy Analysis of Tomographic Modeling with Real Data

The data were available in RINEX format with 30 seconds data interval and were pre-processed to derive the total tropospheric delays and gradient parameters in the stations using Bernese software version 4.2. A full 24 hours of data for May 25-June 4, 2002 (Day 145-155) and June 14, 2002 (Day 165) have been chosen for processing data from the stations CHIL, DAM2, CSN1, CLAR and HOLP to estimate the regional wet refractivity. Zenith wet delays were recovered by applying a hydrostatic model based on surface pressure measurements. The processing was conducted in batch mode of one-hour interval. Hourly estimates of zenith delay and 12-hourly estimates of azimuthal gradients were

derived. National Geodetic Survey (NGS) precise orbits were used and an elevation cutoff angle of 15° was applied. In order to derive absolute zenith delays, it is necessary to use long baselines in the double difference processing. Three additional GPS reference stations (SLCU, DHLG, and SIO3) were used in a multiple reference station approach. These stations are located 892 km (SLCU), 232 km (DHLG) and 178 km (SIO3) from the reference station CHIL. The slant wet delay observations were recovered at 30-second intervals by removing the hydrostatic components from the total zenith delays, adding the gradient contributions, and mapping the resulting wet delays to slant line-of-sight delays. Details of the processing technique were provided in Section 4.4.

The following test statistic was derived:

- The RMS slant wet delays was calculated at independent test site JPLM by deriving the slant wet delays from predicted wet refractivity values and comparing these values with slant wet delays derived for JPLM using the Bernese software version 4.2. Since observations from JPLM are not included in the adjustment to determine wet refractivity fields, this is considered to be an independent test statistic.

Accuracies of slant wet delays derived in Section 4.4 were on the order of 2 cm. It is therefore inferred that slant wet delay observations derived for reference station JPLM in these tests (using the Bernese software) may have only centimetre-level accuracies. This "truth" data, which is used to validate tomographic model predictions, is therefore limited in accuracy. The following parameters are used to estimate the wet refractivity at the center of network:

- Number of steps for trace along line-of-sight path $= 200$
- Elevation mask angle for slant wet delay observations $= 15°$
- Number of vertical troposphere layers for adjustment $= 8$
- Number of reference stations $= 5$

- Top vertical layer height for troposphere = 8000 m

The elevation cutoff angle has been chosen as 15° because it is the best elevation cutoff angle to minimize the effect due to multipath and to minimize the error on the Nw estimates. As shown in simulation results, 8 vertical layers are taken for the estimation of the wet refractivity to minimize the errors on Nw estimation.

Figure 5.18 shows the RMS slant wet delays for the test station JPLM for May 25-June 4, 2002 (Day 145-155) and June 14, 2002 (Day 165). The tomographic model predicts slant wet delay corrections with accuracies at the 2-3 cm level. These results indicate that tomographic models may be employed within regional networks to derive slant wet delay corrections with accuracies at the 2-3 cm level. In Chapter 4, it was shown that the accuracy of slant wet delays derived from GPS data was about 2 cm when compared with the WVR data as truth values.
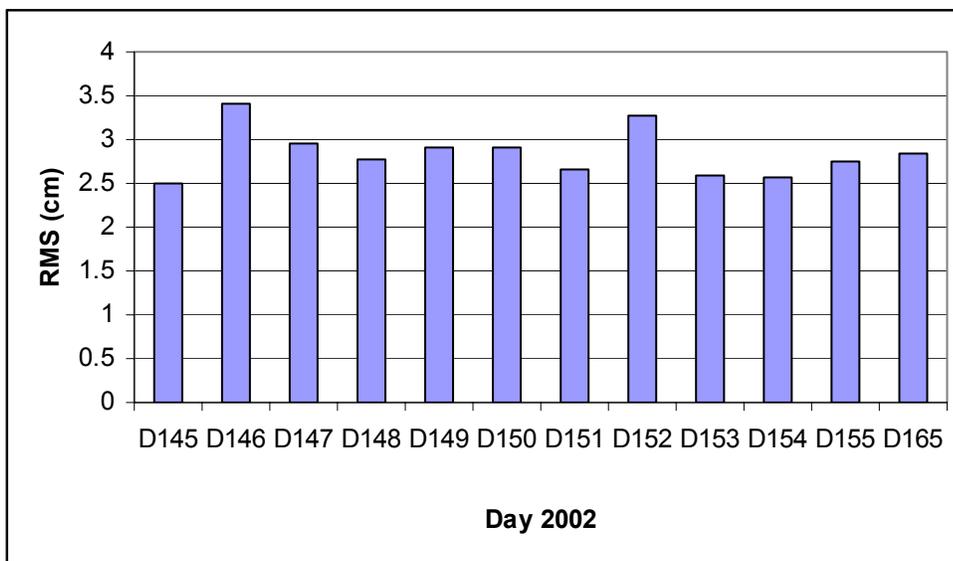
Figure 5.18 Overall accuracies of slant wet delays derived from the tomographic model, as assessed at the test station JPLM.

Figure 5.19 shows the variations in RMS values for slant wet delays at test station JPLM on May 25, 2002 (Day 145). The results show that the RMS values are in the range 1.3 cm to 4.2 cm. The overall RMS value for JPLM is 2.51 cm for the whole day.
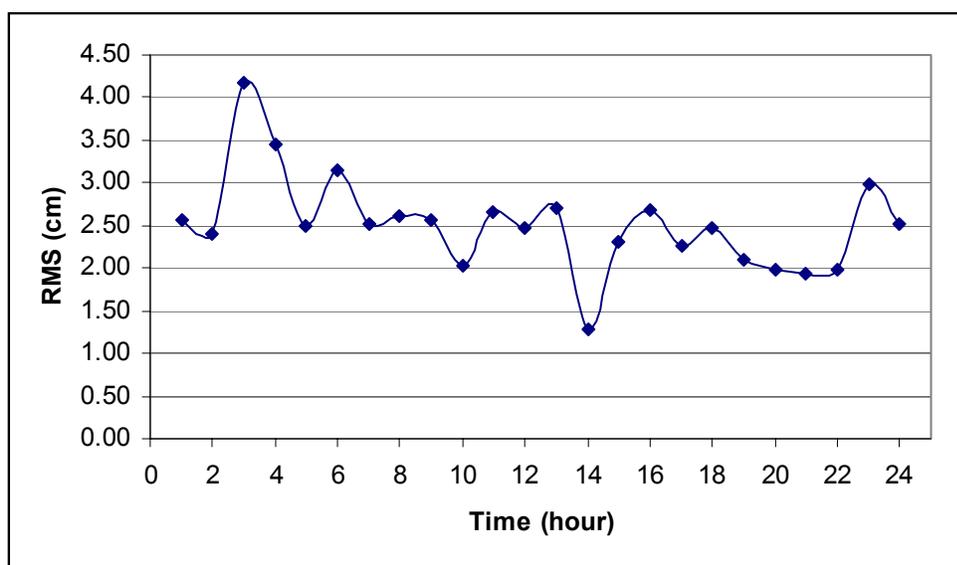
Figure 5.19 Hourly accuracies of slant wet delays derived from tomographic model predictions, as derived for test station JPLM on May 25, 2002 (Day 145).

Figure 5.20 shows the RMS values for slant wet delays at JPLM as a function of elevation angle for May 27, 2002 (Day 147). The errors clearly increase with lower elevation angles. The reasons for this are that the "truth" slant wet delays from Bernese processing have larger errors at lower elevations because the mapping function gives larger errors at lower elevations. Also, larger errors in the wet refractivity estimates and slant wet delays are derived by integrating through the 3-D profiles at the edges of the network, which would affect the lower elevation observations to a larger extent.
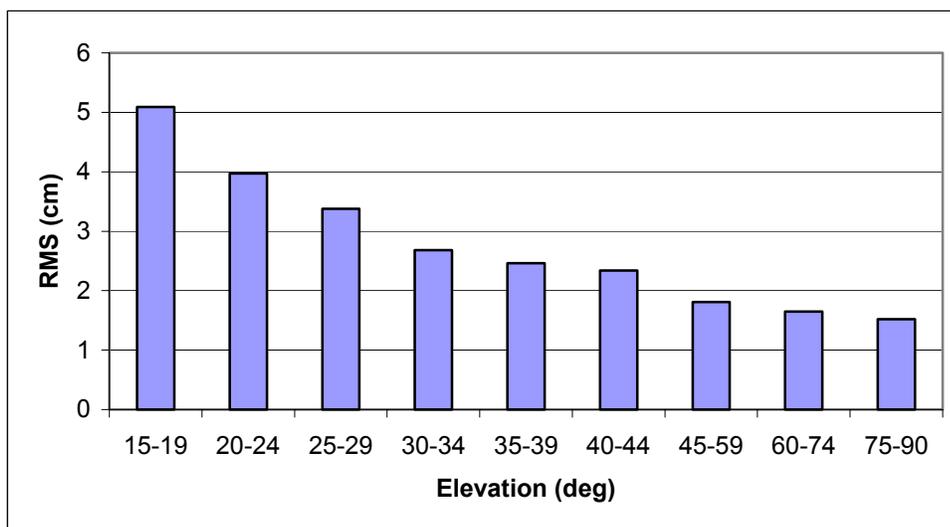
Figure 5.20 RMS values for slant wet delays as a function of elevation angle for test station JPLM for May 27, 2002 (Day 147).

Slant wet delays were used as input observables to define the wet refractivity in a regional network using a tomographic technique. Figure 5.21 shows the wet refractivity profiles in the troposphere at the network expansion point $(34.19°\,N, 118.17W)$ for 18:00 UT, May 29, 2002 (Day 149). The refractivity profile indicates an inversion event at lower altitudes, with a general decrease in refractivity at higher altitudes. Figure 5.22 shows the wet refractivity profiles in the troposphere at the network expansion point $(34.19°\,N, 118.17W)$ for 19:00 UT, May 29, 2002 (Day 149). The refractivity profile indicates a general decrease in refractivity with altitude. There was no truth data for the refractivity profiles such as radiosonde observations, but the nature of the profiles can be considered in order to assess capabilities of the modeling approach.
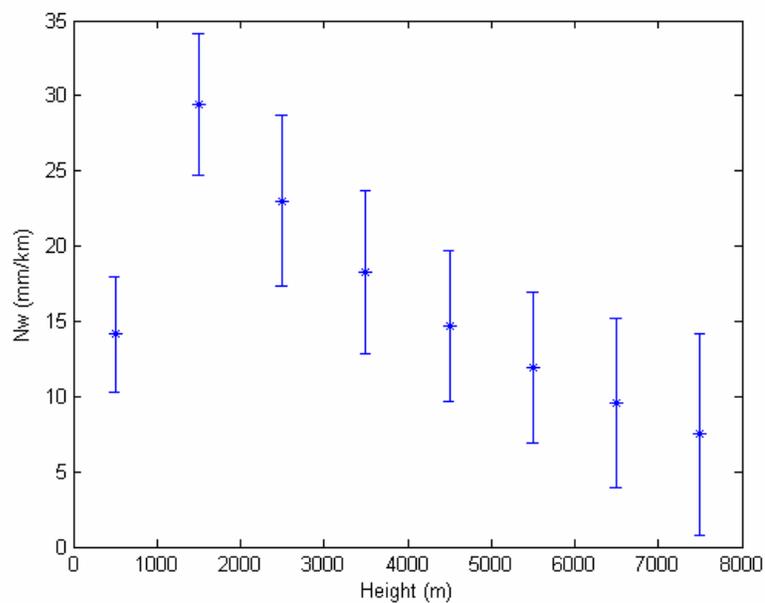
Figure 5.21 Wet refractivity profile at network expansion point (34.19°N, 118.17°W**)**

at 18:00 UT, May 29, 2002 (Day 149).
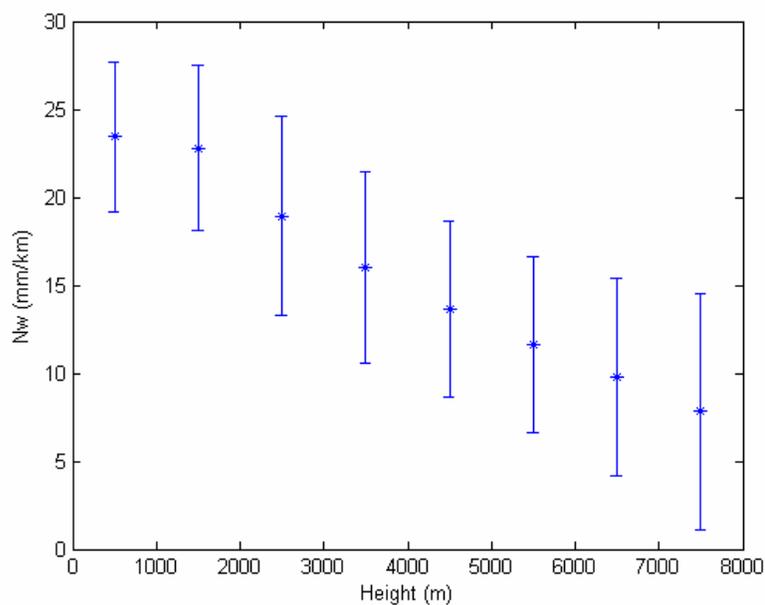
Figure 5.22 Wet refractivity profile at network expansion point (34.19°N, 118.17°W**)**

at 19:00 UT, May 29, 2002 (Day 149).

5.3.3 Summary of Real Data Results

The tomographic technique was tested with observations from five GPS reference stations (CHIL, DAM2, CSN1, CLAR, and HOLP) in the SCIGN network, in order to determine the wet refractivity profile within the local network. Station JPLM, located near the center of the network, was used as an independent test site to check the validity of wet refractivity estimates calculated by the tomographic technique. Accuracies were evaluated by deriving slant wet delays computed for all satellite-receiver lines-of-sight at JPLM using the wet refractivity estimates from five stations in the network and these values were then compared with the slant wet delays at JPLM computed using Bernese software version 4.2. The tomographic processing was conducted with 8 vertical layers and a 15° elevation cutoff angle. The tomographic model gives accuracies of slant wet delay corrections at the 2-3 cm level for the station JPLM. These results indicate that tomographic models may be employed within regional networks to derive slant wet delay corrections with accuracies at the 2-3 cm level. The results also showed that the RMS slant wet delay error increases with lower elevation angles. The "truth" slant wet delays from Bernese processing have larger errors at lower elevations because the mapping function gives larger error at lower elevations. Also, larger errors in Nw at the edges of the network would affect the lower elevation observations to a larger extent.

CHAPTER 6

CONCLUSIONS AND RECOMMENDATIONS

The Global Positioning System reached operational status in early 1994 and is now operating continuously with the 24-satellite constellation. Traditionally it was used for high precision geodesy, and the GPS system has recently emerged as a powerful tool in atmospheric studies, in particular, climatology and meteorology (Bar-Sever and Kroger, 1998). Tropospheric delay is a major source of error in GPS positioning. However, the delay is considered as a signal for GPS meteorology. As explained in Chapter 4, the delays experienced by the GPS signal while traversing the troposphere can be estimated accurately if the position of the receiver and the satellite is known. The total tropospheric zenith delay can be separated into two components, a delay due to dry gases in the troposphere and the non-dipole component of water vapor refractivity, called the zenith hydrostatic delay, and a delay due to the dipole component of water vapor refractivity, called zenith wet delay.

Total zenith delays and gradient parameters can be estimated with the present GPS data processing. The zenith hydrostatic delay can be accurately inferred from precise measurements of atmospheric pressure. Once the total zenith delays are estimated from the GPS data processing and the zenith hydrostatic delays are removed, the observables remaining are the zenith wet delays. The magnitude of the wet delays depend on the vertically integrated quantity of water vapor (PWV) in the atmosphere, which is the main meteorological product that the ground-based GPS estimates. The accuracy of the zenith wet delays was tested using zenith wet delays from the WVR as a truth. The RMS errors of the zenith wet delays were about 2-3 cm in the clear weather, as the WVR does not give reliable results with water droplets in its observation window.

The slant wet delays were generated using a mapping function with the zenith wet delays. These delays were computed at 30 second intervals for all the satellites in view corresponding to the station-satellite direction. The slant wet delays from the GPS data

were compared with those of the water vapor radiometer data. The RMS slant wet delays were found 1.62-4.29 cm for a data set collected in May-June, 2002.

There are several factors that affect wet delays during the processing of GPS data. The RMS wet delay errors decrease as the elevation cutoff angles increase. The RMS zenith wet delay errors were 0.88 cm and 0.81 cm when elevation cutoff angles were $15°$ and $20°$ respectively. The RMS slant wet delay errors were 1.86 cm and 1.66 cm when elevation cutoff angles were $15°$ and $20°$ respectively.

Likewise, wet delay errors also depend on the batch processing interval for the estimation of tropospheric parameters. Definition of tropospheric parameters using a short batch processing interval gives better evaluation of seasonal variation of water vapor in the atmosphere with less wet delay errors. The RMS zenith wet delay errors were 0.96 cm and 0.99 cm when the tropospheric parameters were estimated with the elevation cutoff angle $15°$ every 1 hour and 2 hours, respectively. The RMS zenith wet delay errors were 0.67 cm and 0.81 cm when the tropospheric parameters were estimated with the elevation cutoff angle $20°$ every 1 hour and 2 hours, respectively. The RMS slant wet delay errors were 2.17 cm and 2.26 cm when the tropospheric parameters were estimated with the elevation angle $15°$ every 1 hour and 2 hours, respectively. The RMS slant wet delay errors were 1.89 cm and 2.02 cm when the tropospheric parameters were estimated with the elevation angle $20°$ every 1 hour and 2 hours, respectively.

Similarly, wet delay error also depends on the baseline length of reference stations, as the GPS processing with short baseline reference stations does not recover absolute tropospheric delay and, ultimately, it increases wet delay errors. The RMS zenith wet delay errors were 2.07 cm and 3.10 cm with the elevation angle $15°$ when the baseline length of reference stations were 737 km and 25 km, respectively. The RMS zenith wet delay errors were 1.83 cm and 3.08 cm with the elevation angle $20°$ when the baseline length of reference stations were 737 km and 25 km, respectively. The RMS slant wet delay errors

were 4.23 cm and 6.29 cm with the elevation angle $15°$ when the baseline lengths of reference stations were 737 km and 25 km, respectively. The RMS slant wet delay errors were 3.88 cm and 5.94 cm with the elevation angle $20°$ when the baseline lengths of reference stations were 737 km and 25 km, respectively.

A tropospheric tomography technique is used to determine 4D refractivity in the troposphere over a small network. Dividing the troposphere up to a height of 8 km above GPS receivers into layers, the refractivity in each layer is estimated in successive windows by discrete inversion methods. The basic observables for tomography are GPS slant wet delays for respective pairs of stations and satellites. Extensive simulations were performed to analyze the sensitivity of the tomographic solution for the definition of the wet refractivity as a function of vertical layers, elevation cutoff angles, and the height of stations. These simulation results help to specify the network capabilities for the determination of wet refractivity in a local network.

The simulation was carried out using two atmospheric profiles: average exponential decay of N_w with height (Nw_ave), and an inversion layer in N_w profile near the surface (Nw_inv). The RMS error of Nw estimation was 0.36 mm/km with 16 vertical layers, whereas it was 1.06 mm/km with 8 vertical layers for Nw_ave profile. The RMS error of N_w estimation was 2.84 mm/km with 16 vertical layers, whereas it was 1.66 mm/km with 8 vertical layers for Nw_inv profile. The RMS errors of N_w estimation were 0.88 mm/km, 1.11 mm/km, and 0.58 mm/km corresponding to 50 m, 200 m, and 400 m height differences between each station in the network for the Nw_ave profile. The RMS errors of N_w estimation were 5.42 mm/km, 5.28 mm/km, and 1.37 mm/km corresponding to 50 m, 200 m, and 400 m height difference between each station in the network for the Nw_inv profile. The RMS errors were 1.62 mm/km, 1.05 mm/km, and 0.76 mm/km, respectively when the elevation cutoff angle was changed into $10°$, $15°$, and $20°$ for the Nw_ave profile. The RMS errors of N_w estimation were 1.43 mm/km, 1.66 mm/km, and 2.12 mm/km when

the elevation angle was $10°$, $15°$, and $20°$ for the Nw_inv profile. Recommendation is made to take a lower elevation cutoff angle for tomographic processing as the lower elevation slant wet delays strengthen the tomographic solution.

The tomographic technique was tested with real data to define the wet refractivity over a local network. For this purpose, six stations of the Southern California Integrated GPS Network (SCIGN) have been taken as a local network. Accuracies were evaluated by deriving slant wet delays from N_w estimates by integrating N_w along the appropriate line-of-sight and comparing these values with slant wet delay observations at the station JPLM. GPS data from five reference stations were used to estimate the wet refractivity in the network. The GPS data from the station JPLM, which is almost located in the center of the network was used to calculate "truth" slant wet delays. The results showed that the RMS slant wet delays at the JPLM station was 2-3 cm. This result indicates that the accuracy of slant wet delay corrections is encouraging to define the wet refractivity of the network using the tomographic technique. The results from the estimation of wet refractivity showed the inversion layer in the N_w profile near the surface of the Earth and average decrease of N_w profile with altitude, which were the real representation of the troposphere. The results also showed that the RMS slant wet delays derived from the tomographic model increase for lower elevations when they are compared with slant wet delays derived from GPS observations using Bernese software version 4.2.

The following recommendations are presented for further work:

- The hydrostatic gradient parameter should be extracted from the total gradient to recover the wet gradient parameter. If hydrostatic gradient is not removed from the total gradient to calculate slant delays, the estimated wet refractivity field is called pseudo-wet refractivity fields, which may significantly differ from wet refractivity under conditions of strong surface pressure gradients.

- GPS sensing of slant wet delays should be determined down to $0°$ elevation to detect water vapor associated with fronts, storms, and other weather and climate phenomena at distances of several hundred kilometres.

- Tropospheric parameters and wet refractivity are expected to determine near real time, as they can be used to meteorological purposes.

REFERENCES

Alber, C., R. Ware, C. Rocken and J. Braun (2000), Obtaining single path phase delays from GPS double differences, Geophysical Research Letters, Vol. 27, pp. 2661-2664.

Alber, C., R. Ware, C. Rocken and F. Solheim (1997), GPS surveying with 1 mm precision using corrections for atmospheric slant path delay, Geophysical Research Letters, Vol. 24, pp. 1859-1862.

Baby, H.B., P. Gole and J. Lavergnat (1988), A model for the tropospheric excess path length of radio waves from surface meteorological measurements, Radio Science, November-December, Vol. 23, No. 6, pp. 1023-1038.

Bar-Sever, Y.E. (1996), Strategies for near real time estimation of precipitable water vapor, IGS 1996 Analysis Center Workshop Proceedings, pp. 165-175.

Bar-Sever, Y.E. and P.M. Kroger (1998), Estimating horizontal gradients of tropospheric path delay with a single GPS receiver, Journal of Geophysical Research, Vol. 103, No. B3, pp. 5019-5035.

Bauersima, I. (1983), NAVSTAR/Global Positioning System (GPS), II, No. 7, Astronomical Institute, University of Berne, Switzerland.

Bean, B.R. and E.J. Dutton (1966), Radio meterology, National Bureau of Standards Monograph 92, U.S. Government Printing Office, Washington, D.C., pp. 435.

Berman, A.L. (1976), The prediction of zenith range refraction from surface measurements of meteorological parameters, Jet Propulsion Laboratory, California Institute of

Technology, Pasadena, Calif., National Aeronautics and Space Administration Technical Report 32-1602, pp. 40.

Bevis, M., S. Businger, T.A. Herring, C. Rocken, R.A. Anthes and R.H. Ware (1992), GPS meteorology: sensing of atmospheric water vapor using the Global Positioning System, Journal of Geophysical Research, Vol. 97, No. D14, pp. 15787-15801.

Bevis, M., S. Businger, S. Chiswell, T.A. Herring, R.A. Anthes, C. Rocken and R. Ware (1994), GPS meteorology: mapping zenith wet delays onto precipitable water, Journal of Applied Meteorology, Vol. 33, pp. 379-386.

Beutler, G. and M. Rothacher (2002), Advance aspects of GPS positioning, Summer Lecture Notes, ENGO 699.80, University of Calgary, Calgary, Canada.

Beutler, G. (1996), GPS satellite orbits, GPS for Geodesy, Eds. Kleusberg A, Teunissen PJG, Springer, Berlin Heidelberg New York Tokyo, pp. 37-101.

Beutler, G., I. Bauersima, W. Gurtner, M. Rothacher, T. Schildknecht and A. Geiger (1988), Atmospheric refraction and other important biases in GPS carrier phase observations, Atmospheric Effects on Geodetic Space Measurements, Monograph 12, pp. 15-43, School of Surveying, University of New South Wales, Kensington, Australia,

Black, H.D. (1978), An easily implemented algorithm for the tropospheric range correction, Journal of Geophysical Research, Vol. 83, No. B4, pp. 1825-1828.

Boudouris, G. (1963), On the index of the refraction of the air, the absorption and dispersion of centimeter waves by gases, Journal of Research of the National Bureau of Standards, Vol. 67D, pp. 631-684.

Bouma, H.R. and B. Stoew (2001), GPS observations of daily variations in the atmospheric water vapor content, Physics and Chemistry of Earth (A), Vol. 26, No. 6-8, pp. 389-392.

Brunner, F.K. (1984), Geodetic refraction: effects on electromagnetic wave propagation through the atmosphere, Springer-Verlag, New York, N.Y., USA.

Brunner, F.K. and W.M. Welch (1993), Effect of the troposphere on GPS measurements, GPS World, Vol. 4, No. 1, pp. 42-51.

Bruton, A. (2000), Improving the accuracy and resolution of SINS/DGPS airborne gravimetry, UCGE Reports No. 20145, University of Calgary, Calgary, Canada.

Businger, S., S.R. Chiswell, M. Bevis, J. Duan, R.A. Anthes, C. Rocken, R.H. Ware, M. Exner, T. VanHove and F.S. Solheim (1996), The promise of GPS in atmospheric monitoring, Bulletin of American Meteorological Society, Vol. 77 (1), pp. 5-18.

Chandrasekhar, S. (1950), Radiative transfer, Oxford University Press, New Jersey, USA.

Cannon, M.E. (2001), ENGO 561: Satellite positioning, Winter Lecture Notes, University of Calgary, Calgary, Canada.

Cannon, M. E., G. Lachapelle, M. Olynik, M.G. Petevello, B. Gelatka and J. Davis (2001), P3 aircraft buffeting using precise carrier phase techniques, Proceedings of ION GPS-2001, Salt Lake City, Utah, pp. 1009-1016.

Chao, C.C. (1972), A model for tropospheric calibration from daily surface and radiosonde balloon measurement, Jet Propulsion Laboratory, Pasadena, Calif., Technical Memorandum 391-350, pp. 16.

Chen, G. and T.A. Herring (1997), Effects of atmospheric azimuthal asymmetry on the analysis of space geodetic data, Journal of Geophysical Research, Vol. 102, No. B9, pp. 20489-20502.

Cucurull, L., A. Rius, F. Vandengerghe and M. de Pondeca (2001), 4D-VAR assimilation of GPS-derived ZTD: A case study, Proceedings, ION GPS 2001, Salt Lake City, UT, USA.

Davis, J.L., T.A. Herring, I.I. Shapiro, A.E.E. Rogers and G. Elgered (1985), Geodesy by radio interferometry: effects of atmospheric modeling on estimates of baseline length, Radio Science, Vol., 20, No. 6, pp. 1593-1607.

Davis, J.L., G. Elgered, A.E. Neill and C.E. Kuehn (1993), Ground-based measurement of gradients in the wet radio refractivity of air, Radio Science, Vol. 28, No. 6, pp. 1003-1018.

Davis, J.L. (2001), Atmospheric water vapor signals in GPS data: Synergies, correlations, signals, and errors, Physics and Chemistry of Earth (A), Vol. 26, No. 6-8, pp. 513-522.

Dixon, T.H. and S.K. Wolf (1990), Some tests of wet tropospheric calibration for the CASA UNO Global Positioning System experiment, Geophysical Research Letters, Vol. 17, No. 3, pp. 203-206.

Dodson, A.H. and H.C. Baker (1998), The accuracy of GPS water vapour estimation, Proceedings ION-NTM 98, January, Institute of Navigation, Alexandria, pp. 649-657.

Dodson, A.H., P.J. Shardlow, L.C.M. Hubbard, G. Elgered and P.O.J. Jarlemark (1996), Wet tropospheric effects on precise relative GPS height determination, Journal of Geodesy, No. 70, No. 4, pp. 188-202.

Duan, J.P., M. Bevis, P. Fang, Y. Bock, S. Chiswll, S. Businger, C. Rocken, F. Solheim, T. VanHove, R. Ware, S. McClusky, T.A. Herring and R.W. King (1996), GPS meteorology: direct estimation of absolute value of precipitable water, Journal of Applied Meteorology, Vol. 35, No. 6, pp. 830-838.

Elgered, G., J.L. Davis, T.A. Herring and I.I. Shapiro (1991), Geodesy by radio interferometry: water vapor radiometry for estimation of the wet delay, Journal of Geophysical Research, Vol. 96, No. B4, pp. 6541-6555.

England, M.N., R.A. Ferrare, S.H. Melfi, D.N. Whiteman and T.A. Clark (1992), Atmospheric water vapor measurements: comparison of microwave radiometry and lidar, Journal of Geophysical Research, Vol. 97, No. D1, pp. 899-916.

Essen, L. and K.D. Froome (1951), The refractive indices and dielectric constants of air and its principal constituents at 24, 000 Mc/s. Proceedings of the Royal Society B, Vol. 64, pp. 862-875.

Flores, A., L.P. Gradinarsky, P. Elosegui, G. Elgered, J.L. Davis and A. Rius (2000a), Sensing atmospheric structure: tropospheric tomographic results of the small-scale GPS campaign at the Onsala Space Observatory, Earth Planets Space, No. 52, pp. 941-945.

Flores, A., G. Ruffini and A. Rius (2000b), 4D tropospheric tomography using GPS slant wet delays, Annales Geophysicae, No. 18, pp. 223-234.

Flores, A., A. Rius, J. Vila-Guerau de Arellano and A. Escudero (2001), Spatio-temporal tomography of the lower troposphere using GPS signals, Physics and Chemistry of Earth, Vol. 26, No. 6-8, pp. 405-411.

Gelb, A. (1974), Applied Optimal Estimation, MIT Press, Cambridge, Mass., USA.

Gendt G., G. Dick, A. Rius and P. Sedo (2001), Comparison of software and techniques for water vapor estimation using German near real-time GPS data, Physics and Chemistry of Earth (A), Vol. 26, No. 6-8, pp. 417-420.

Gendt G., C. Reigber and G. Dick (2001), Near real-time water vapor estimation in a German GPS network-first results from ground program of the HGF GASP Project, Physics and Chemistry of Earth (A), Vol. 26, No 6-8, pp.413-416.

Goad C.C. and L. Goodman (1974), A modified Hopfield tropospheric refraction correction model. Paper presented at the American Geophysical Union Annual Fall Meeting at CA, 12-17 December, pp. 28.

Gradinarsky, L. and G. Elgered (2000), Horizontal gradients in the wet path delay derived from four years of microwave radiometer data, Geophysical Research Letters, Vol. 27, No. 16, pp. 2521-2524.

Gradinarsky, L., R. Hass, G. Elgered and J.M. Johansson (2002), Wet path delay and delay gradients inferred from microwave radiometer, GPS and VLBI observations, Earth Planets Space, No. 52, pp. 695-698.

Gradinarsky, L. and P. Jarlemark (2002), GPS tomography using the permanent network in Goteborg: simulations, Proceeding of IEEE Position, Location and Navigation Symposium, Palm Springs, Calif., pp. 128-133.

Gurtner, W., G. Beutler and M. Rothacher (1989), A common exchange format for GPS data, GPS Bulletin, 2(3), pp. 1-11.

Hill, R.J. (1988), Dispersion by atmospheric water vapor at frequencies less than 1 Thz, IEEE Transactions on Antennas and propagation, Vol. 36, No. 3, pp. 423-430.

Hill, R.J., R.S. Lawrence and J.T. Prestley (1982), Theoretical and calculational aspects of the radio refractive index of water vapor, Radio Science, Vol. 17, No. 5, pp. 1251-1257.

Herring, T.A. (1992), Modeling atmospheric delays in the analysis of space geodetic data, Proceedings of Symposium on Refraction of Transatmospheric Signal in Geodesy, The Netherlands, No. 36, New series, pp. 157-164.

Herring, T.A., J.L. Davis and I.I. Shapiro (1990), Geodesy by radio interferometry: the application of Kalman filtering to analysis of very long baseline interferometry data, Journal of Geophysical Research, Vol., 95, No. B8, pp. 12561-12581.

Hirahara, K. (2000), Local GPS tropospheric tomography, Earth Planets Space, No. 52, pp. 935-939.

Hiromu, S., S. Shimada, H. Nakamura and T. Kato (2000), Three-dimensional distribution of water vapor estimated from tropospheric delay of GPS data in a mesoscale precipitation system of the Baiu front, Earth Planets Space, No. 52, pp. 927-933.

Hoffmann-Wellenhof, B., H. Lichtenegger and J. Collions (1994), GPS theory and practice, 3rd Edition, Springer-Verlag, New York, NY, USA.

Hopfield, H.S. (1971), Tropospheric effect on electromagnetically measured range: Prediction from surface weather data, Radio Science, Vol. 6, No. 3, pp. 357-367.

Hopfield, H.S. (1969), Two quartic tropospheric refractivity profile for correcting satellite data, Journal of Geophysical Research, Vol. 74, No. 18, pp. 4487-4499.

Hugentobler, U., S. Schaer and P. Fridez (2001), Bernese GPS software, Version 4.2, Astronomical Institute, University of Bern, Switzerland.

Ifadis, I.M. (2000), A new approach to mapping the atmospheric effect for GPS observations, Earth Planets Space, No. 52, pp. 703-708.

Ifadis, I.M. (1986), The atmospheric delay of radio waves: modeling the elevation dependence on a global scale, School of Electrical and Computer Engineering, Chalmers University of Technology, Goteborg, Sweden, Technical Report No. 38L, pp. 115.

International GPS Service (IGS) (2001), International GPS service annual report, 2001, IGS Central Bureau, Jet Propulsion Laboratory, Pasadena, Calif., pp. 14-16.

Janes, H.W., R.B. Langley and S.B. Newby (1991), Analysis of tropospheric delay prediction models: comparisons with ray tracing and implications for GPS relative positioing, Bulletin Geodesique, Vol. 65, No. 3, pp. 151-161.

Jarlemark, P.O.J. and T.R. Emardson (1998), Strategies for spatial and temporal extrapolation and interpolation of wet delay, Journal of Geodesy, No. 72, pp. 350-355.

Kaniuth, K. (1986), A local model for estimating the tropospheric path delay at microwave frequencies, Proceedings of the Fourth International Geodetic Symposium on Satellite Positioning, Austin, Texas, April 28-May 2, Vol. 1, pp. 589-601.

Kaplan, E. (1996), Understanding GPS principles and applications, Artech House, Norwood, Mass., USA.

Kleijer, F. (2001), Mapping function induced bias in tropospheric delay estimation using GPS, Physics and Chemistry of Earth (A), Vol. 26, No. 6-8, pp. 467-470.

Klobuchar, J.A.(1996), Ionospheric effects in Global Positioning System: theory and applications, Vol. I, ed. B.W. Parkinson and J.J. Spilker, American Institute of Aeronautics and Astronautics, Washington, D.C., USA.

Lachapelle, G. (1994), High accuracy GPS positioning, Navtech Seminars Courses 330, Lecture Notes.

Lachapelle, G., H. Sun, M.E. Cannon and G. Liu (1994), Precise aircraft-to-aircraft positioning using a multiple receiver configuration, Proceedings of the National Technical Meeting, The Institute of Navigation, San Diego, California, pp. 793-799.

Lachapelle, G., Advanced GPS theory and applications, ENGO 625 Course Lecture Notes, 2001, University of Calgary, Calgary, Canada.

Lachapelle, G., Hydrography, ENGO 545 Course Lecture Notes, 2000, University of Calgary, Calgary, Canada.

Langi, G. (1984), Tropospheric delay effects in radio interferometry, Jet Propulsion Laboratory, California Institute of Technology, Pasadena, Calif., April-June, TDA Progress Report No. 42-78, pp. 152-159.

Lichten, S.M., (1990), Estimation and filtering for tropospheric path delays with GPS techniques, Manuscripta Geodetica, Vol. 15, pp. 159-176.

Liou, Y. and C.Y. Huang (2000), GPS obseravations of PW during the passage of a typhoon, Earth Planets Space, No. 52, pp. 709-712.

Marini, J.W. (1972), Correction of satellite tracking data for an arbitrary tropospheric profile, Radio Science, Vol. 7, No. 2, pp. 223-231.

Mendes, V.B. (1999), Modeling the neutral-atmosphere propagation delay in radiometric space techniques, PH.D. dissertation, University of New Brunswick, Frederiction, Canada.

Mendes, V.B. and R.B. Langley (1995), Zenith wet tropospheric dealy determination using prediction models: Accuracy analysis, Cartografia E Cadastro, No. 2.

Neill, A.E. (1996), Global mapping functions for the atmospheric delay at radio wavelengths, Journal of Geophysical Research, Vol. 111, No. B2, pp. 3227-3246.

Neill, A.E. (2000), Improved atmospheric mapping functions for VLBI and GPS, Earth Planets Space, No. 52, pp. 699-702.

NovAtel (2000), Look into NovAtel's GPS-600 antenna, Production Specification Sheet.

Olynik, M.C., (2002), Temporal characteristics of GPS error sources and their impact on relative positioning, UCGE Reports No. 20162, University of Calgary, Calgary, Canada.

Onsala Space Observatory (1998a), Microwave radiometer, Chalmers University of Technology, Sweden.

Onsala Space Observatory (1998b), Global Positioning System, Chalmers University of Technology, Sweden.

Oltmans, S.J. and D.J. Hofmann (1995), Increase in lower-stratospheric water vapour at a mid-latitude northern hemisphere site from 1981 to 1994, Nature, Vol. 374, pp. 146-149.

Pacione, R., E. Fionda, C. Sciarretta, F. Vespe and R. Rerrara (2001), GPS and ground-bsed microwave radiometer IPWV: A case study at Cagliari Astromomical Station, Italy, Proceedings, ION GPS 2001, Salt Lake City, UT, USA.

Pattinson, M., A. Dodson and T. Moore (2002), Tropospheric delay estimation from a moving GPS receiver, Proceedings ION GPS 2002, Portland, WA, USA.

Radiometrics (2000), User's manual WVR-1100 (Total integrated water vapor and liquid water radiomter), October 16, 2000.

Raquet, J.F. (1998), Development of a method for kinematic GPS carrier phase ambiguity resolution using multiple reference receivers, UCGE Reports No. 20116, University of Calgary, Calgary, Canada.

Ray, J. (2000), Mitigation of GPS code and carrier phase multipath effects using a multi-antenna system, Ph.D. Thesis, Department of Geomatics Engineering, University of Calgary, Calgary, Canada.

Ray, J., M.E. Cannon and P. Fenton (1998), Mitigation of static carrier phase multipath effects using multiple closely-spaced antennas, Proceedings of ION GPS-98, Nashville, Tennessee, Institute of Navigation, pp. 1025-1034.

Remondi, B.W. (1984), Using the Global Positioning System (GPS) phase observable for relative geodesy: modeling, processing, and results, University of Texas at Austin, Center for Space Research.

Reigber, C., G. Gendt, G. Dick and M. Tomassini (2001), Near real-time water vapor monitoring in a German GPS network and assimilation into weather forecast model, Proceedings, ION GPS 2001, Salt Lake City, UT, USA.

Reigber, C., G. Gendt, G. Dick and M. Tomassini (2002), Water vapor monitoring for weather forecasts, GPS World, 1 Jan. 2002.

Richmond, A. D. (1983), Solar-Terrestrial Physics, Eds. Carovillano and Forbes, Reidel.

Rocken, C., R. Ware, T.V. Hove, F. Solheim, C. Alber and J. Johnson (1993), Sensing atmospheric water vapor with the global positioning system, Geophysical Research Letters, Vol. 20, No. 23, pp. 2631-2634.

Rocken, C., T.V. Hove and R. Ware (1997), Near real-time GPS sensing of atmospheric water vapor, Geophysical Research Letters, Vol. 24, No. 24, pp. 3221-3224.

Rocken, C., J. Braun, T.V. Hove and R. Ware (2000), GPS networks for atmospheric sensing, GPS Science and Technology (GST) Program.

Ruffini, G., L.P. Kruse, A. Rius, B. Burki, L. Cucurull and A. Flores (1999), Estimation of tropospheric zenith delay and gradients over the Madrid area using GPS and WVR data, Geophysical Research Letters, Vol. 26, No. 4, pp. 447-450.

Saastamoinen, J. (1973), Contribution of the theory of atmospheric refraction, Bulletin of Geodesique, No. 105, pp. 279-298, No. 106, pp. 383-397, No. 107, pp. 13-34.

Saastamoinen, J. (1972), Atmospheric correction for troposphere and stratosphere in radio ranging of satellites, Geophysical monograph, 15, American Geophysical Union, Washington, D.C., pp. 247-252.

Sapucci, L.F. (2001), Precipitable water measurements using GPS: A case study in Brazil, Proceedings ION GPS 2001, Salt Lake City, UT, USA.

Schueler, T., A. Posfay, G.W. Hein and R. Biberger (2001), A global analysis of the mean atmospheric temperature for GPS water vapor estimation, Proceedings ION GPS 2001, Salt Lake City, UT, USA.

Shoji, Y., H. Nakamura, K. Aonashi, A. Ichiki and H. Seko (2002), Semi-diurnal and diurnal variation of errors in GPS precipitable water vapor at Tsukuba, Japan caused by site displacement due to ocean tidal loading, Earth Planets Space, No. 52, pp. 685-690.

Skone, S. (1998), Wide area ionospheric grid modeling in the auroral region, UCGE Reports, No. 20213, University of Calgary, Calgary, Canada.

Skone, S., Atmospheric effects on satellite navigation system, ENGO 633 Course Lecture Notes, 2001, University of Calgary, Calgary, Canada

Skone, S. and S.M. Shrestha (2003), Strategies for 4-D regional modeling of water vapor using GPS, Proceedings of the ION National Technical Meeting 2003, Anaheim, Calif., USA.

Smith, T.L., S.G. Benjamin, B.E. Schwartz and S.I. Gutman (2002), Using GPS-IPW in a 4-D data assimilation system, Earth Planets Space, No. 52, pp. 921-926.

Smith, E.K. and S. Weintraub (1953), The constants in the equation for atmospheric refractive index at radio frequencies. Proceedings of I.R.E., August, Vol. 4, pp. 1035-1037.

Stoew, B., P. Jarlemark, J. Johanssson and G. Elgered (2001), Atmospheric delay estimates from a ground-based real-time GPS network, Proceedings ION GPS 2001, Salt Lake City, UT, USA.

Thayer, G.D. (1974), An improved equation for the radio refractive index of air, Radio Science, Vol. 9, No. 10, pp. 803-807.

Tralli, D.M. and S.M. Lichten (1990), Stochastic estimation of tropospheric path delays in Global Positioning System geodetic measurement, Bulletin Geodesique, Vol. 64, No. 2, pp. 127-159.

Van Dierendonck, A. J., P. Fonton and T. Ford (1992), Theory and performance of narrow correlator spacing in a GPS receiver, Navigation, Vol. 30, No. 3 Fall, pp. 265-283.

Vey, S., E. Calais, M. Llubes, N. Florsch, G. Woppelmann, J. Hiderer, M. Amalvict, M.F. Lalancette, B. Simon, F. Duquenne and J.S. Haase (2002), GPS measurements of ocean loading and its impact on zenith tropospheric delay estimates: A case study in Brittany, France, Journal of Geodesy, No. 76, pp. 419-427.

Ware, R., C. Alber, C. Rocken and F. Solheim (1997), Sensing integrated water vapor along GPS ray paths, Geophysical Research Letters, No. 24, pp. 417-420.

Ware, R., C. Rocken, F. Solheim, T.V. Hove, C. Alber and J. Johnson (1993), Pointed water vapor radiometer corrections for accurate global positioning system surveying, Geophysical Research Letters, Vol. 20, No. 23, pp. 2635-2638.

Ware, R., D.W. Fulker, S.A. Stein, D.N. Anderson, S.K. Richard, D. Clark, K.K. Droegemeier, J.P. Kuettner, J.B. Minster and S. Sorooshian (2002), Suominet: a real-time national GPS network for atmospheric research and education, Bulletin of the American Meteorological Society, Vol. 81, No. 4, pp. 677-694.

Wells, D.E., N. Beck, D. Delikaraoglou, A. Kleusberg, E.J. Krakiswsky, G. Lachapelle, R.B. Langley, N. Nakiboglou, K.P. Schwarz, J. Tranquilla and P. Vanicek (1987), Guide to GPS Positioning, 2nd printing with corrections, Canadian GPS Associates, Fredericton, N.B., Canada.

Zhang, J. (1999), Investigations into the estimation of residual tropospheric delays in a GPS network, UCGE Reports No. 20132, University of Calgary, Calgary, Canada.

Zhang, J. and G. Lachapelle (2001), Precise estimation of residual troposheric delays using a reginal GPS network for real-time kinematic applications, Journal of Geodesy, No. 75, pp. 255-266.

Zumberge, J.F. and W.I. Bertiger (1996), Ephemeris and clock navigation message accuracy, in GPS: theory and applications, Vol. I, Eds: B.W. Parkinson and J.J. Spilker, American Institute of aeronautics and Astronautics, Washington, D.C., USA.

APPENDIX A

OUTPUT OF THE WATER VAPOR RADIOMETER (WVR)

In YYJJJhhmm.gps file, the records include the time tag, azimuth and elevation of the GPS
satellite (and of the radiometer observation), the GPS space vehicle identification (ID), the
brightnesses at the two radiometer frequencies, the radio path delay due to vapor (Vdlycm),

```
MO DY YR HR MN SC ID   AZact ELactTb23   Tb31 VDlycm zVDlycm  Liqcm zLDlycm
02/19/02 15:39:53 26 315.0  25.2  22.43  19.00   5.51   2.34  .0116  .0072
02/19/02 15:40:42 23 309.4  12.6  43.51  35.00  12.46   2.72  .0246  .0078
02/19/02 15:41:48  2 254.2  54.0  12.57  10.99   2.67   2.16  .0047  .0055
02/19/02 15:44:10 13 173.5  10.8  48.42  39.32  13.96   2.62  .0289  .0078
02/19/02 15:45:13  8 130.1  87.8   9.96   9.57   1.70   1.70  .0042  .0061
02/19/02 15:46:03 27 124.4  53.5  12.40  11.47   2.42   1.94  .0057  .0067
02/19/02 15:46:51 19 123.4  13.1  41.11  32.62  11.84   2.67  .0219  .0072
02/19/02 15:47:43 11 114.6  11.7  44.89  35.98  12.96   2.63  .0253  .0074
02/19/02 15:48:51 31  52.9  31.9  18.51  15.89   4.34   2.30  .0090  .0069
02/19/02 15:50:05 26 132.0 151.7  20.67  17.59   4.99   2.37  .0104  .0071
02/19/02 15:50:55 23 125.4 168.8  49.71  39.50  14.73   2.87  .0280  .0079
02/19/02 15:51:58  2  77.0 122.0  11.75  11.05   2.20   1.86  .0055  .0067
02/19/02 15:53:09  7  19.4 169.2  50.26  40.70  14.63   2.74  .0300  .0081
02/19/02 15:54:33  8 130.2  82.8  10.99   9.49   2.30   2.28  .0032  .0046
02/19/02 15:55:23 27 127.0  48.6  13.45  12.10   2.79   2.09  .0060  .0066
02/19/02 15:56:18 11 111.6  14.9  37.50  29.76  10.65   2.73  .0195  .0072
02/19/02 15:57:26 31  50.3  28.4  20.89  17.48   5.15   2.45  .0100  .0069
02/19/02 15:58:41 26 129.0 148.9  19.41  16.69   4.58   2.36  .0097  .0073
02/19/02 15:59:32 23 122.0 169.7  53.45  42.64  15.97   2.87  .0310  .0081
02/19/02 16:00:33  2  79.7 118.3  11.15  10.80   1.94   1.71  .0055  .0070
02/19/02 16:01:41  7  19.7 165.6  39.74  32.15  11.16   2.78  .0222  .0080
02/19/02 16:03:08  8 131.6  78.8  10.52   9.84   1.92   1.88  .0042  .0060
02/19/02 16:03:56 27 128.9  45.0  14.68  12.82   3.23   2.28  .0064  .0065
02/19/02 16:04:50 11 108.7  17.6  33.08  26.13   9.28   2.80  .0162  .0071
02/19/02 16:05:59 31  48.6  25.2  23.64  19.42   6.06   2.58  .0114  .0070
02/19/02 16:07:13 26 125.6 146.7  18.16  15.50   4.28   2.35  .0085  .0068
02/19/02 16:08:17  2  82.6 114.8  11.05  10.62   1.95   1.77  .0052  .0069
02/19/02 16:09:29  7  20.2 162.0  32.47  26.55   8.76   2.71  .0176  .0079
02/19/02 16:10:55  8 133.3  74.3  10.68   9.66   2.07   2.00  .0038  .0053
```

APPENDIX B

OUTPUT OF THE METEOROLOGICAL PACKAGE MET3A

The output of the meteorological package Met3A consists of the date and time tag, pressure in bar, the external temperature in deg C, and the relative humidity in %.

```
Paroscientific, Inc. Digiquartz Assistant Data Log File.
Sampled Data Type:    ,  Pressure ,Ext.Temp. ,Humidity ,
Engineering Units:    ,  bar      ,deg C     ,RH%      ,

      DATE/TIME    ,  CHANNEL1, CHANNEL2, CHANNEL3,
02/19/2002 16:00:04.150,  .871851,  8.5,     27.7,
02/19/2002 18:00:04.440,  .872090,  5.5,     33.5,
02/19/2002 20:00:04.020,  .872242,  3.0,     45.8,
02/19/2002 22:00:05.140,  .872497,  2.9,     44.6,
02/20/2002 00:00:02.690,  .873342,       ,  53.7,
02/20/2002 02:00:06.160,  .874035,       ,  55.2,
02/20/2002 04:00:05.470,  .875147,  2.1,     46.7,
02/20/2002 06:00:05.650,  .876614,  3.2,     40.6,
02/20/2002 08:00:02.590,  .879457,  1.3,     43.1,
02/20/2002 10:00:05.190,  .881985,  3.5,     39.0,
02/20/2002 12:00:05.050,  .883871,  5.9,     33.0,
02/20/2002 14:00:04.850,  .884605,  6.9,     23.8,
02/20/2002 16:00:02.170,  .886110,  6.7,     26.2,
02/20/2002 18:00:05.270,  .887512,  3.5,     29.2,
02/20/2002 20:00:05.010,  .890027,       ,  45.6,
02/20/2002 22:00:03.160,  .890854,  -2.5,     59.4,
02/21/2002 00:00:06.260,  .891461,  -3.1,     64.4,
02/21/2002 02:00:02.810,  .891976,  -3.3,     66.3,
```